The University of Nottingham
UNITED KINGDOM · CHINA · MALAYSIA

Thermal monitoring of electric machines using fibre-optic sensors with machine learning algorithms

Kun Shang (20198670)

Supervision Team:

Prof. Vladimir Brusic, Dr. Yaping Zhang, Prof. Michael Galea, Dr. Weiduo Zhao, Dr. Shun Bai

PhD Thesis

Submitted in partial fulfilment of the requirement for the degree of Doctor of Philosophy

Department of Electrical and Electronic Engineering

Faculty of Science and Engineering

University of Nottingham Ningbo China

Abstract

Electric machines (EM) are widely considered as the main energy conversion devices among industry 4.0 era: they are employed in major industry sectors including but not limited to manufacturing, transportation electrification, power generation and industrial machinery. EMs consume ~75% of electricity across all areas of industry. EMs fail mainly because of undetected overheating. Conventional electronic thermal sensors do not operate reliably inside EMs because of strong electromagnetic fields inside that cause interferences with electronic sensors.

In this work, we investigated fibre-optic sensors (FOS) for thermal monitoring of EMs. Fibre Bragg grating (FBG) was evaluated and chosen for the EM thermal monitoring application from various principles of FOS techniques. A novel sensor system combining FBG sensor with machine learning (ML) algorithms was designed and validated progressively to achieve comprehensive thermal monitoring of EMs. The self-constructed lab-version FBG temperature sensor system presented 20-200℃ measurement range with maximum 1kHz sensing frequency, 5cm spatial resolution, and 3.5 ± 1.5℃ error compared with thermocouple measurement. SVR and MLPR machine learning algorithms were proven to be qualified for our EM thermal monitoring task. The FBG-ML combined sensor system presented good regression performance for inner EM temperature prediction with the values of regression evaluation indices as: Mean absolute error (MAE)< 5℃, Root mean squared error (RMSE) <15℃, Coefficient of determination (R^2)>0.9 and Explained variance score (EVS)>0.9. Compared to the conventional thermal sensors and simulation methods for EMs, our FBG-ML sensor prototype can measure the EM thermal

distribution in a more accurate, more robust, more convenient manner, and more sensitive to the actual EM working conditions.

The socio-ethically informed standard was developed and published after the construction of sensor prototypes, it made up for the blank of the standard establishment of industrial intelligent monitoring systems (IMS). Additionally, three Chinese invention patents were applied based on our FBG-ML sensor prototype. The utilization of FBG sensor with ML algorithms can improve safety and reliability of electric machines and other power electronic equipment, pre-diagnose equipment failure, reduce maintenance cost, prolong lifetime, and optimize control. The research in this thesis demonstrated both scientific research significance as well as the practical engineering value within Industry 4.0.

Acknowledgements

An immense thank you to my PhD supervisors: Prof. Vladimir Brusic, Dr. Yaping Zhang, Prof. Michael Galea, Dr. Weiduo Zhao, Dr. Serhiy Korposh and Dr. Shun Bai. The support and guidance from my supervisors throughout the project were unconditional, inspiring, and always timely. Vladimir and Yaping have been fantastic leading supervisors – they offered continuous guidance on many aspects of this PhD project. I owe special thanks to Michael for guiding me to build the strong foundations of this project and his support on the experimental design. Thanks to Serhiy for the guidance on theory and practical aspects of fibre optic sensors. Thanks to Weiduo for the support in parts of the project that involved electric machines and Shun for his help with electronic hardware. Prof. Giampaolo Buticchi inspired me and helped me extend the innovation part of my project to power electronics solutions.

Working with two research departments, namely the electrical and electronic engineering and the computer science, has been an amazing experience – the interdisciplinary of this project enriched my experiences and enabled me to observe different points of view and then harmonize them into, in my opinion, powerful solutions to a problem that is difficult to solve.

I want to express my gratitude to the wonderful colleagues from the PEMC and SSNI Research Groups. It was a great fun to work with you! Special thanks to Dr. Bowen Shi and Mr. Han Zhao, for assistance with the constructions of the test-rig.

Thank you Ziqian Liu. We stood together and helped each other during our academic journey, sharing both good and difficult times. Most importantly, thanks to my parents for their loving support and believing in me all the way from my first breath to the completion of PhD.

Deliverables of this PhD Project

Publications

1. **K. Shang**, M. Galea, V. Brusic, S. Korposh, Y. Zhang. "Polyimide-coated fibre Bragg grating (FBG) sensors for thermal mapping of electric machine windings"**,** 22nd International Conference on Transparent Optical Networks (ICTON 2020), (Scopus, EI index)
2. **K. Shang**, Y. Zhang, M. Galea, V. Brusic, S. Korposh. "Fibre optic sensors for the monitoring of rotating electric machines: a review", Optical and Quantum Electronics 53 (2), 1-28. (SCI, JCR Q2 (OPTICS / Engineering ELECTRICAL & ELECTRONICS), IF:2.794)
3. **K. Shang**, M. Galea, V. Brusic, W. Zhao, Y. Zhang. "Fibre Bragg grating (FBG) thermal monitoring system for copper windings of electric machines under different duty modes", International Conference on Sensors and Instruments (ICSI 2021), (Scopus, EI index)
4. **K. Shang**, S. McDonald, G. Buticchi, V. Brusic. "The development of ethically informed standards for intelligent monitoring systems of electric machines", IEEE 46th Annual Computers, Software, and Applications Conference (COMPSAC 2022), (Scopus, EI index)
5. **K. Shang**, Y. Zhang, M. Galea, V. Brusic. "Optimized Multi-sensor system for comprehensive thermal mapping of electric machine windings using Fibre-optics and supervised machine learning", (for the at the time of the thesis submission the draft has been completed, but the publication has been suspended until the IP protection is secured)

Patents

1. **K. Shang**, V. Brusic, M. Galea, Y. Zhang. Chinese invention patent: A system and method for measuring internal temperature of electrical machine windings using fibre-optic sensors and machine learning (基于光纤传感和机器学习的电气设备绕组内部温度测量方法及系统), (CN. Patent No.202210507701.9)
2. G. Buticchi, **K. Shang**, V. Brusic, Y. Zhang. Chinese invention patent: A fibre-optic temperature and reliability measurement system for power electronics components (基于光纤光栅传感的电力电子设备可靠性监测方法与系统), (CN. Patent No.202210966810.7)
3. G. Buticchi, **K. Shang**, V. Brusic, Y. Zhang. Chinese invention patent: An intelligent optic- fibre based monitoring and control system for optimized operations of wind power systems (基于光纤传感的风电机组监测控制方法及系统), (CN. Patent No.202210961294.9)

List of Figures

List of Tables

List of Abbreviations

Abbreviation	Definition
EM	Electric machine
FOS	Fibre optic sensor
FBG	Fibre Bragg grating
ML	Machine learning
PHM	Prognostics and health management
IMS	Intelligent monitoring system
IoT	Internet of Things
AI	Artificial intelligence
FEA	Finite element analysis
RTD	Resistance thermal detectors
TC	Thermocouple
LPTN	Lumped parameter thermal network
EMI	Electromagnetic interference
WDM / TDM / FDM	Wavelength / Time / Frequency division multiplexing
DPF	Displacement power factor
UV	Ultraviolet
CW	Central wavelength
DFOS	Distributed fibre optic sensor
OTDR	Optical time-domain reflectometry
FOG	Fibre optic gyroscope
RF	Radio frequency
IR	Infrared
BPMOR	Brushless permanent magnet outer rotor
PMSM	Permanent magnet synchronous motor
DTG	Draw tower gratings
2D / 3D	Two / Three Dimensional

FPI	Fabry-Perot interferometer
PD	Partial discharge
OUT	Object under test
EXP	Experiment / Experimental
DC	Direct-Current
IL	Insertion loss
SVR / SVC	Support vector regression / classification
MLPR	Multi-layer Perceptron Regression
BP	Back-propagation
ANN	Artificial neuron network
RFR	Random forest regression
SVM	Support vector machine
S1-S10	IEC duty-cycle modes of electric motors
MAE	Mean absolute error
MAPE	Mean absolute percentage error
RMSE	Root mean squared error
R-squared	Correlation / Determination coefficient
ES	Exponential smoothing

Table of Contents

1 Introduction

In this chapter, we present a brief state-of-the-art review of the industrial role of electric machines (EMs), and discuss the main bottleneck of EM operations – the thermal limits. Given the scientific and technical limitations of thermal monitoring methods for EMs, the research gaps were identified and the specific research questions for this PhD project were defined. The main topic of this work focuses on the design, implementation, and validation of a robust and accurate fibre-optic sensor system for comprehensive thermal monitoring of EM.

1.1 Review of state-of-the-art in the field

Electric machines (EMs) are widely used in major industry sectors including manufacturing, transportation, power generation and industrial machinery [1-3]. Market research reports agree that the global market size for EMs is rapidly growing and has exceeded 100 billion USD [4]. The electricity usage by EMs makes approximately half of the global electricity consumption and two-thirds of the total electrical energy consumption by the industry [5, 6]. Each 1% of power efficiency improvement of EMs will result in 0.5% of global electricity savings. These potential improvements promote the research in EM design, as well as performance and maintenance optimization. Basic design requirements for EMs include economical operation, generation of sufficient power, and longevity. The principal factors that diminish the life of an EM (Figure 1.1) include mechanical (bearing) and electrical (stator windings) failures [7, 8]. Bearings are vulnerable to the wear and tear, rotor eccentricity, misalignments, inadequate lubrication, or electrical failures, mostly due to the bearing currents and shaft voltages [9]. Stator windings may

fail due to thermal stress [10], electrical stress, or damage from external environmental factors [8]. Integrated sensor systems enable optimization of operational parameters, prevention of overloading, safety alerts while out of operational safe zone, and optimization of maintenance. Accurate and reliable sensors for critical EM parameters are needed to provide for EM operation and condition monitoring. Additionally, EM optimal design evolution and control algorithm optimization can be achieved with reliable EM sensor system.

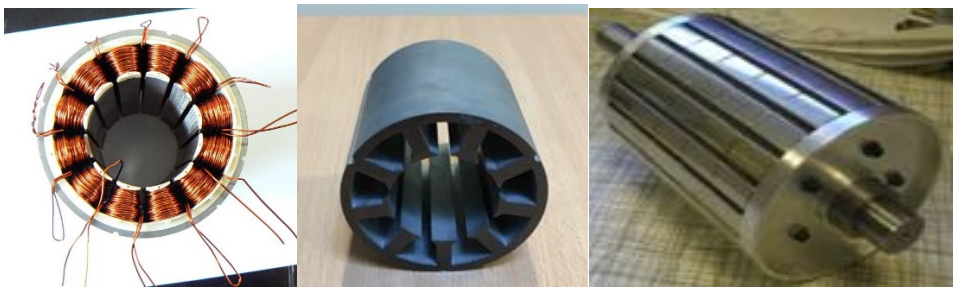

a) b) c)

Figure 1.1. Photos of a stator of EM a) with and b) without copper windings, c) a rotor of EM with permanent magnet attached to the rotor surface.

The size of global electric motor market was estimated to have surpassed 120 billion USD in 2021 (Figure 1.2). The same study has estimated the annual market growth at 6.70%, with the forecast of 210 billion USD by 2030. The development and innovation of electrification and related machinery systems are very fast, particularly within the transformation called Industry 4.0 [11]. Conventional industrial modules will be integrated by new technologies, for instance, Internet of Things (IoT), cloud computing and AI systems. It is a fourth industrial revolution that drives efficiency across operations including electric industry [12].

The ability to monitor operational parameters of EMs and accurately assess their values, including temperature, vibration, electrical current, and other relevant indicators offers promises for

optimization of performance and longevity of EMs. This will, in turn, enable significant savings on the cost of running, replacing, and maintaining EMs.

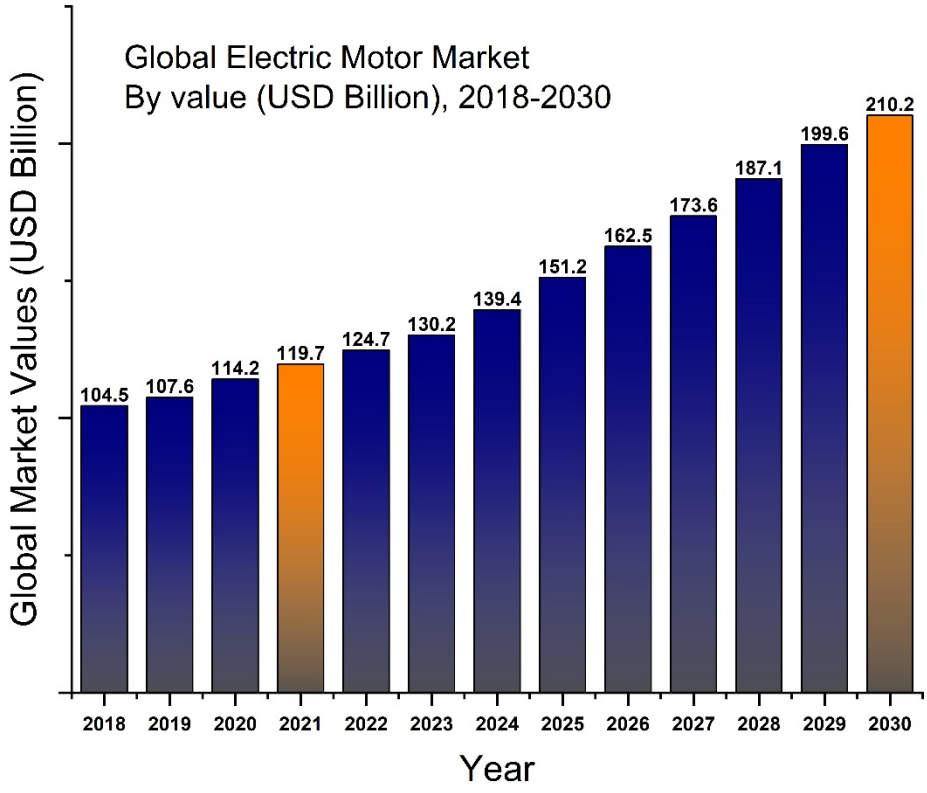

Figure 1.2. Estimated overall global market of electric motors is expected to double over the following 10 years. Based on the study reported by BlueWeave Consulting [13].

Accurate and efficient monitoring of electrical machine (EM) operating parameters can indicate the specific "health" status of EMs, such operating parameters include temperature, mechanical vibration, torque, rotating speed etc. With large-scale automation of industrial processes, operational parameter monitoring is growing in importance in the world of electrical drives. The

traditional methodology of one sensor per parameter can be theoretically replaced by a single fiber optical carrier with multiple sensor sites technology and a single measurement instrument (source, interrogator, and optical fibre). Several key advantages for monitoring operational parameters of EM can be achieved through the use of fibre-optic sensor systems (FOS), but there is a number of challenges that need to be resolved before the technology is ready for deployment [14].

Among the physical parameters of EMs, both the motors and generators, the most important factor for maintaining "healthy" operational status is the thermal limit. The thermal limit categories are defined by the insulation classes within EMs (Figure 1.3). Copper windings of EMs are most vulnerable to the excessive thermal stress [12, 13]. The ability to reliably monitor the temperature of the EM copper windings is essential for improving both the cost of using and the lifespan of the EMs.

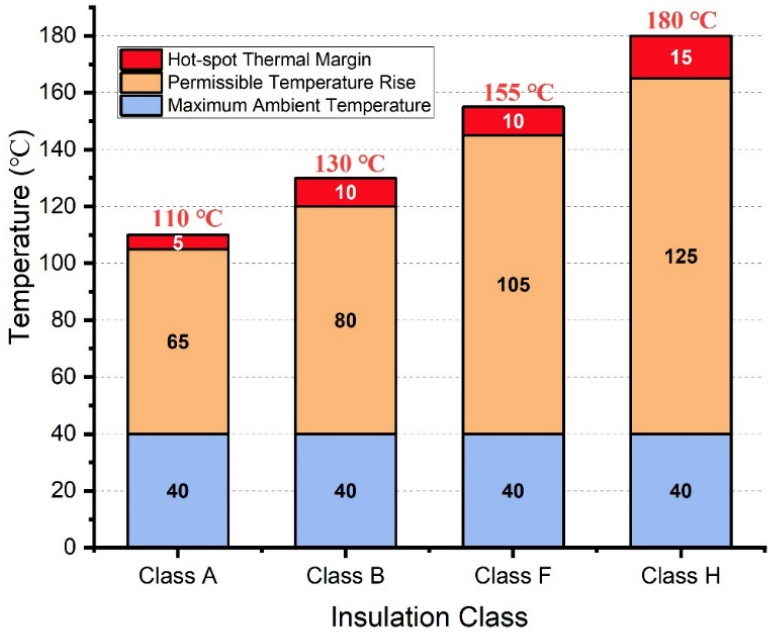

Figure 1.3. International temperature standard & limitations for four insulation classes, originally defined by the US National Electrical Manufacturers Association (NEMA) [17].

Several methods for assessing the winding temperature in electrical equipment have been used. They include direct measurement method, guide calculation method, thermal circuit analytical method, Finite Element Analysis (FEA) and artificial intelligence (AI) algorithm modelling method [18]. The direct measurement method detects the temperature at one or more positions within the windings using embedded temperature sensors. Comprehensive thermal data collection of EM copper windings is required during the thermal test stage of the EM design. Therefore, a large number of discrete sensors, such as thermocouples (TCs) or resistance thermal detectors (RTDs), are embedded within the EM windings for thermal monitoring and temperature data acquisition [19]. This process increases both the physical and assembling complexities of EM

manufacturing and maintenance. The guide calculation method currently uses the temperature calculation formula recommended by IEEE C57.91-1995 and the China national standard GB/T1094.7-2008. This method uses empirical formulas, and the results obtained are far from the experimental measured data [20]. The thermal circuit analytical method, also called lumped parameter thermal network (LPTN) is based on the heat transfer and thermoelectric analogy theories. According to the heat transfer parameters and operating parameters of EMs, the corresponding thermal circuit model is established to study its thermal characteristics [21]. However, this method requires multiple points of winding temperatures, and the number and positions of the measurement points must be set in advance. Due to the theoretical assumptions of the boundary conditions during model construction, the differences between the thermal circuit temperatures and actual temperatures are common and errors can be high [22]. The FEA method is based on the finite element theory for assessing temperatures in a three-dimensional temperature field model of electrical equipment [23]. The internal temperatures of target object can be assessed with certain resolution. This method requires accurate and comprehensive knowledge of the structure and used materials, and the electromagnetic parameters for the specific EM. The process of model building is of high complexity and is time consuming. The AI algorithm modelling uses historical data or experimental data collected from monitoring the EM operation to construct a model of relationship between various input features and inner winding temperatures [24]. Such models produce the predictions of temperature within the winding in multiple positions. Commonly used AI methods include types of machine learning algorithms, for instance, logistic regression, support vector regression, artificial neural network, random forest regression [16, 17], and recursion algorithms like Kalman filtering [27]. The AI learning method has strong fault

tolerance and self-adaptive ability, and it is increasingly applied across various engineering industries [28].

Compared to the conventional direct measurement method using thermocouples, Fibre Bragg Grating (FBG) sensors provide several advantages for the thermal monitoring of electric windings [19, 20]. Because FBG sensors are fiber-optics based, they have intrinsic properties that make them an attractive option for thermal monitoring of EMs. These advantages include immunity to electromagnetic interference (EMI), small dimensions (around 125μm diameter of optical fibre) and the ability to fit between copper windings without disrupting their alignment [30]. Multiplexing techniques developed for FBG sensor systems, such as wavelength division multiplexing (WDM) [31], enable concurrent sensing of a large number of discrete points. The FBG sensing points can be spaced at millimeter-level among the windings. In practice, the best measurement points depend on the size and the nature of the windings and need to be determined for each type of the application scenario. The thermal monitoring of EM windings using FBG sensor has been proven to be effective and accurate [23-25].

Instead of using many discrete sensor systems for monitoring individual EM parameters separately, an integrated sensing system capable of multi-parameter measurements is a preferred alternative. Modern fibre-optic based sensing technology offers multiple advantages for EM's multi-parameter online monitoring [30]:

- All dielectric
- Immunity to EMI
- Compact (small weight and size)

- Low-cost
- Accurate and sensitive measurements
- High environmental robustness

1.2 Research gaps & the formulation of research questions

The industrial thermal monitoring methods currently used for EM have limitations in terms of the accuracy, cost and reliability as we discussed. A novel sensor system is required to fill this gap of EM thermal blind issue. The new sensor solution should present the capability of comprehensive thermal monitoring for EM with high reliability. Fibre optic sensor techniques will be investigated as the potential solution in our project due to its robust advantages for EM monitoring application. It will be an emerging efficient alternative for EM thermal monitoring in both cost-saving and safety improvement within electrification industry. The aim of research and specific research questions are presented:

Aim of research:

Construct and verify a fibre optic sensor system for comprehensive thermal monitoring of rotating electric machines (EM), especially for the most vulnerable component, the EM- copper windings.

Specific research questions:

- Is it feasible to use fibre optic sensor for thermal monitoring of real operating EM? If so, how to validate this hypothesis?
- How to achieve comprehensive EM winding thermal monitoring with optimal number of thermal sensors?

- How to monitor internal winding temperatures without in-situ sensors placed?

To find the answers to the stated research questions, the first step was to perform a literature review of modern fibre-optic sensor techniques for physical parameters monitoring of EM sensors. The literature review is presented in Chapter 2.

2 Theoretical concepts and literature review

In this chapter, a detailed literature review of FOS techniques used for multiple physical parameters of EM monitoring is presented with the discussion of their advantages and disadvantages. The combination of FOS systems and ML algorithms employed for EM monitoring is reviewed in this section. The appropriate combination of suitable FOS technique and ML algorithms represent be the novel contribution that addresses the research gaps of thermal monitoring of EM. The successful combination of FBG-ML is a solution for comprehensive thermal monitoring of EM. We briefly discuss the benefits of such combination and present the overall study design framework. The validation of proposed solution is presented in the main body of this thesis.

2.1 Fibre optic sensors (FOS) for EM multi-physical parameters monitoring

Modern FOS sensing principles (Figure 2.1) have been employed for EM parameter monitoring. These involve Fibre Bragg Grating (FBG), distributed FOS, interferometric FOS and reflective FOS [35]. In this section, several FOSs, which use different optical sensing principles for multiple physical parameter measurements of EMs, are reviewed. This section provides an insight into the major contemporary developments, and discusses various engineering challenges of FOS used for EM monitoring.

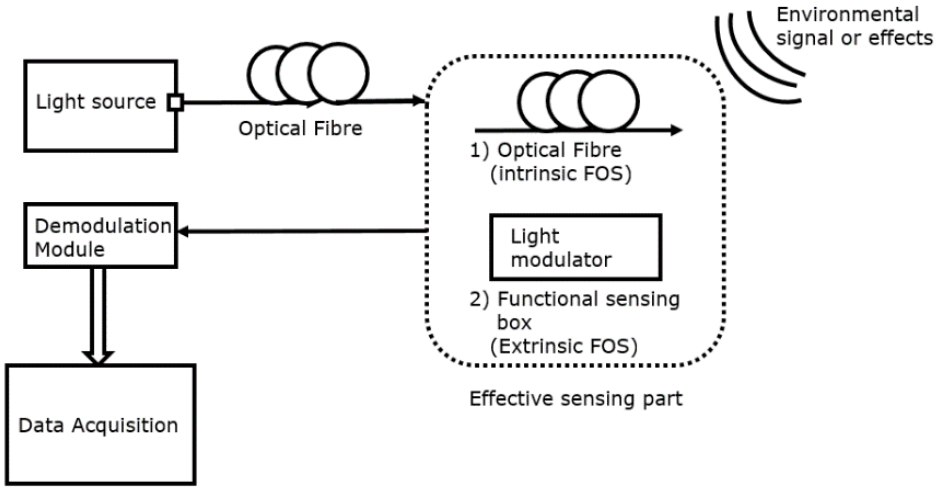

Figure 2.1. General schematics for two types of FOS system (intrinsic and extrinsic FOS), depending on whether effective sensing is taking place within the optical fibre.

The main objective of this literature review is a critical evaluation of the state of the art of concurrent and continuous monitoring of critical physical parameters during the EM operation using Fibre Optic Sensors (FOS). The key monitored parameters include **temperature, mechanical vibration, rotation speed, torque, and power efficiency.** Conventional monitoring solutions require a set of sensor systems for each individual parameter: thermocouples or resistance thermal detectors (RTDs) combined with temperature loggers are used for temperature measurement of stationary parts (stator and bearing). An electric encoder or resolver is used for the EM's rotating speed measurement. Piezoelectric accelerators are used for EM vibration measurement. A combination of multiple conventional sensor systems is characterized by high costs, installation complexity, and synchronization issues for real-time multi-parameter simultaneous monitoring.

In this section, an overview of FOS techniques for monitoring of multiple EM physical parameters, as well as a comparison to the conventional electric sensors are presented [36]. A discussion of the application potentials and challenges of a centralized FOS sensor system for EM multi-parameter real-time monitoring is included as the outlook of this PhD project.

2.2 Fibre optic sensors: Principles of measurements for EM applications

Temperature is a critical indicator that affects an EM's life span and reliability. Thermal stresses caused by overheating can degrade the insulation quality of the EM, and thereby reduce its longevity. Temperature monitoring of stator, rotor and bearings are critical measurement targets for understanding the EM's operational health and the prevention of overheating [37]. The **torque and vibration** parameters are good indicators of the EM's mechanical operation status useful for detection of problems and prevention of mechanical failures. Mechanical vibration is considered as an early indicator of EM malfunction, arising from issues such as an unbalanced or misaligned rotor, damaged bearings, or electrical problems on the rotor such as shorted turns in the windings or broken bars in the squirrel-cage induction motors [38]. The **rotating speed** of the EM is monitored to ensure that actual operating characteristics match up with the expected speed. Many applications of EMs require accurate speed information for the control of load and for system feedback. Relative position of the rotor can be calculated once the speed parameter is known. Because the cost of energy (i.e. the electricity supplied) dominates (~95%) the EM life cycle cost [39], **power** monitoring of the EM should be measured to ensure that the displacement power factor (DPF) is observed [40].

2.2.1 Temperature measurement

FBG-based sensors

FBG can be described as a quasi-distributed (i.e. measuring many discrete points within a certain distance) sensor system with each effective sensing grating area in *cm* scale, which can be written inside the optic fibre using UV lasers by either a holographic or phase mask method [41], or written by femtosecond (fs) lasers [42]. The variation of measurand induces the FBG reflected centre wavelength $\boldsymbol{\lambda_B}$ shift where this wavelength shift is intensity-independent, providing the theoretical feasibility for FBG use as a physical variable sensor. FBGs have been widely used for the monitoring of temperature and strain parameters, which have high sensitivity and show a linear response to wavelength shift as shown in Equation 2.1 and 2.2. The quantitative expressions of Bragg wavelength $\boldsymbol{\lambda_B}$ and the shift of Bragg wavelength $\boldsymbol{\Delta\lambda_B}$ in relation to temperature variation $\boldsymbol{\Delta T}$ and strain $\boldsymbol{\varepsilon_{FBG}}$ can be expressed as:

$$\lambda_B = 2n_{eff}\Lambda \tag{2.1}$$

$$\Delta\lambda_B = 2n_{eff}\Lambda\left[\left(1-\frac{n_{eff}^2}{2}(p_{12}+\mu(p_{11}+p_{12}))\right)\varepsilon_{FBG}+(\alpha_\delta+\xi_\delta)\Delta T\right] \tag{2.2}$$

where $\boldsymbol{n_{eff}}$ is the effective refractive index of the optical fibre, $\boldsymbol{\Lambda}$ is the FBG Bragg period, $\boldsymbol{p_{11}}$ and $\boldsymbol{p_{12}}$ are elastic-optic coefficients of FBG, $\boldsymbol{\varepsilon_{FBG}}$ is the experienced strain of FBG along the fibre axis, $\boldsymbol{\mu}$ is the Poisson ratio of fibre material, $\boldsymbol{\alpha_\delta}$ and $\boldsymbol{\xi_\delta}$ are thermal expansion and thermo-optic coefficients of optical fibres, respectively. The thermal response of FBG is in 10 milliseconds level (i.e. ~100 Hz) while the mechanical response of strain is several orders of magnitude faster. Variations of temperature and strain induce Bragg wavelength's shifts, as shown in Figure 2.2.

Typically, detection sensitivities of the temperature and strain variations for a common silica single mode FBG with Bragg wavelength at 1550 nm are around 10pm/°C and 1.2pm/με, respectively [34, 35]. The wavelength shift led by single environmental stimulation (i.e. only temperature change or strain variation) are quantified and presented in Equation 2.3 and 2.4. The response expressions of wavelength shift $\boldsymbol{\Delta\lambda_B}$ to temperature variation $\boldsymbol{\Delta T}$ and strain variation $\boldsymbol{\Delta\varepsilon}$ are expressed as [45]:

$$\frac{\Delta\lambda_B}{\Delta T} = 2n_{eff}\Lambda\left(\alpha_\delta + \frac{1}{n_{eff}}\frac{\Delta n_{eff}}{\Delta T}\right) \tag{2.3}$$

$$\frac{\Delta\lambda_B}{\Delta\varepsilon} = 2n_{eff}\Lambda\left(1 - \frac{n_{eff}^2}{2}(p_{12} + \mu(p_{11} + p_{12}))\right) \tag{2.4}$$

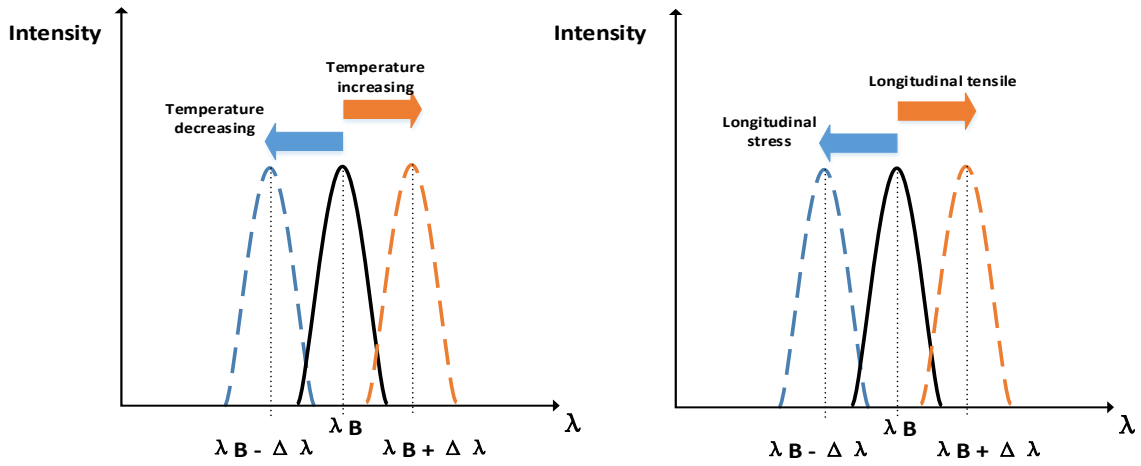

Figure 2.2. FBG-based sensors reflected- spectral for temperature and strain monitoring principle.

For practical FBG sensor installation, advanced packaging techniques of FBG sensors are required to provide temperature compensation [46] to correct FBG sensors shifts used for monitoring parameters other than temperature. Effective packaging of FBG sensor are material-specific and it can increase the detection sensitivities of temperature and strain dramatically [47]. The thermal-strain cross effects can be partially avoided by packaging [39, 40]. FBG sensors may be used to a high-resolution temperature and stress map for EM copper windings for the identifications of malfunction localizations related to hotspots and high stress. The light source for FBG sensing system can be broadband continuous-wave lasers or tunable lasers.

Distributed fibre optic temperature sensors (DFOS)

Distributed FOSs (DFOS) are based on the back-scattering optical signal intensity analysis, which apply nonlinear optic scattering principles, including Rayleigh and Raman scattering methods [50]. These scattering methods help determine quantitative variations of target measurands and their corresponding spatial locations. Scattered lights are generated from the interaction between the SiO_2 molecule electrons and the photons of light particles, which are excited by variations of surrounding physical measurands (e.g. temperature, force, electric fields). The core signal processing technique for DFOS is optical time-domain reflectometry (OTDR) [35], in which weak measurand-induced spectral reflections can be localized using a pulsed optical input.

Assuming the optical fibre is isotropic and placed in a non-disturbance environment, the backscattered intensity shall decay exponentially with time due to the fibre intrinsic loss. However, the decay rate will increase (*i.e.* more loss appears) with the introduced of new physical perturbation. For instance, Raman backscatter temperature sensing method employs OTDR to

monitor the temperature at a specific location. The Raman backscattered light can be divided into three spectral components: Rayleigh scattering at origin pulsed laser wavelength, Stokes (lower photon energy) with left-shift wavelength and Anti-Stokes (higher photon energy) with right-shift wavelength [51]. The optical intensities of both Stokes and Anti-Stokes are temperature-dependent, whereby the intensity ratio of these two kinds can provide the amplitude of measurand temperature. In addition, corresponding spatial locations of these temperature readings can be derived from the laser pulse circulating duration [52]. Theoretically, the location of EM hotspots can be detected through DFOS systems.

The inherently distributed nature of DFOS provides for employing this sensing techniques in EM parameter monitoring. Physical faults or imperfections of EM performance can be measured quantitatively and spatially with the help of DFOS installed along the targeted EM components. For industrial applications of DFOS system, two decisive factors are considered to determine the spatial resolution of DFOS: input laser pulse duration and sampling rate of data acquisition equipment. The narrower the pulse used, the faster sampling rate employed, and the higher the spatial resolution obtained [53]. For example, spatial resolution of ~0.1m can be obtained with 1ns pulses laser input. Theoretically, DFOS is able to measure the temperature of any position along the target component. For high spatial accuracy, an ultra-short pulsed laser (i.e. femtosecond pulsed laser) may be employed as input light source, however this increases both the overall cost and hardware system and the complexity of the DFOS installation. Similarly, it is expensive to use data acquisition devices with high sampling rate, in DFOS system. Considering the cost-effectiveness tradeoff, the DFOS is more suitable for parameter monitoring of very-large scale electric machines, which do not require ultra-short pulsed laser for high spatial precision.

2.2.2 Torque measurement

The best-developed FOS method for torque monitoring in industrial engineering is probably the FBG sensor [44, 45]. For EM generated torque monitoring, the rotor of an EM can be considered as a solid cylinder with composite materials (i.e. a combination of permanent magnet, silicon steel and stainless steel) with a specific tensile elastic modulus. Combining the strain data $\boldsymbol{\varepsilon_{FBG}}$ obtained by the FBG sensor and the tensile elastic modulus of the rotor, the stress on the rotor surface can be calculated. While the overall electromagnetic shear force on rotor surface can be expressed as the product of stress and total area of rotor surface. Finally, the torque can be derived from total shear force and radius of the rotor [56].

2.2.3 Mechanical vibrations measurement

The vibration FOS systems can be categorized into contact sensor system or non-contact depending on their sensing principles and installation methods. Compared to some types of conventional vibration sensors, most FOS accelerometers require no moving parts, providing relatively high robustness and a small housing. There are three main types of FOS system for contact mechanical vibration measurement: FBG-based FOS and interferometric (Fabry-Perot [57] [58], Michelson [59], or Mach-Zehnder [60]) FOS. While interferometric FOS for vibration require complex system setup and strict setup alignment. The FBG-based sensors are preferred to interferometers for EM vibration monitoring since they require fewer supporting facilities, provide higher spatial resolution and use easier demodulation methods and setup. The FBG accelerometer converts strain variation experienced by FBG in specific time range to acceleration [61], for EM vibration monitoring, multi-axis acceleration measurements [62] with temperature compensation

are required [63]. The temperature compensation is accounted for by employing another reference FBG with the same temperature sensitivity at same direction to cancel out the wavelength shift led by temperature variation. Like the FBG torque sensor mentioned above, strain $\boldsymbol{\varepsilon_{FBG}}$ measured by FBG can be converted to acceleration (in unit of $m \cdot s^{-2}$). A photodiode detector can be used to convert the optical signal to an electric signal for temporal information analysis [64].

The non-contact vibration FOS systems for EM, use reflective FOS based on intensity-modulation [55, 56], where the optical fibre plays the role of 'transmission pipe' for the light beam. The reflective FOS need to cooperate with external reflectors, so that the motion of reflector surface modulates optical intensity. The detected and demodulated optical intensity determines the vibration measurement. However, reflective FOS is naturally sensitive to the measurement uncertainty resulting from dynamic unstable reflected power from vibrating surface. Increasing the number of receiving fibres may improve the accuracy of vibration measuring while it complicates sensor setup and requires a precise sensor calibration process [67].

2.2.4 Rotating speed & position measurement

Interferometric FOS based on the Sagnac effect [68] are capable of measuring the rotation rate by detecting angular frequency. Currently, one of the mature FOS products called fibre optic gyroscope (FOG) is built on the Sagnac effect, having longer lifetime and lower cost as compared to conventional gyroscopes. There are two optical propagation modes within the Sagnac interferometric FOS: clockwise and anticlockwise . The light transmitted through these two modes experiences different optical paths due to the rotation of the target object, so the spectral phase difference can be detected from the output side by checking either interference pattern or spectral

intensities. This phase difference $\boldsymbol{\Delta\Phi}$ between clockwise and anticlockwise modes is directly proportional to the angular frequency of sensing fibre coil $\boldsymbol{\Omega}$, which can be expressed as [59, 60]:

$$\Delta\Phi = \frac{8\pi M_f A\Omega}{c\lambda_0} \tag{2.5}$$

Where $\boldsymbol{M_f}$ is the number of turns of the sensing fibre coil, $\boldsymbol{A}$ is the area of Sagnac fibre loop, $\boldsymbol{\Omega}$ is the angular frequency rotation, and $\boldsymbol{\lambda_0}$ is the laser light's free-space wavelength. One of the great advantages of FOG is that this sensor gives no signal for reciprocal stimuli [71]. The environmental disturbances such as temperature variation may affect both beams equally and result in no contribution to overall measurement result. The superluminescent diode is employed as a light source for FOG. Because such diode has a wide spectral bandwidth (tens of nm), high temperature stability and high output power is achieved.

For the FOG used in EM rotating speed & position measurement, one significant challenge is the accuracy of the FOG for angular frequency monitoring. The most advanced FOG currently can only achieve up to 100° per hour angular velocity accuracy, which is too small for general high-speed EMs whose rotation speed is about ~10k rpm. The development of FOG, has potential to surpass the upper limit speed by several orders of magnitude [72].

Another FOS method for rotation speed & position monitoring of the EM is the reflective FOS, similar in principle with the reflective vibration sensor. The coded reflector and photodiode are combined to generate a periodic electronic signal. By demodulating the frequency response of received electronic signal, rotating speed can be determined. Due to the broad bandwidth provided from laser source, reflective FOS can cover sensing frequency range of EM high-speed rotating.

Some researchers have made progress on using FBG strain sensor to measure the EM rotating speed [73], with derived equation which indicates that the FBG experienced strain is proportional to the square of rotating speed [74]. However, the performances of the FOS rotating speed sensors are still limited for high-speed EMs measurements.

FBG-based strain sensing principles are widely used for many targeted mechanical EM parameters discussed above: torque, vibrations and rotating speed. However, these sensors need temperature compensation setup to remove the wavelength shift caused by thermal effects.

2.2.5 Power efficiency calculation

To calculate the power efficiency $\boldsymbol{\eta}$ of EMs, the actual mechanical output power $\boldsymbol{P_{out}}$ of EM is required. $\boldsymbol{P_{out}}$ of EM is related to the EM rotating speed $\boldsymbol{r}$ and torque $\boldsymbol{T}$, Torque of EM in SI units can be calculated in a simplified expression as:

$$P_{out} = T \times \frac{2\pi \times r}{60} = \frac{T \times r}{9.549} \tag{2.6}$$

where $\boldsymbol{T}$ is the torque in Nm, $\boldsymbol{r}$ the rotating rate in rounds per minute (rpm) and $\boldsymbol{P_{out}}$ in watts. Using the torque sensor and rotating speed sensor based on the fibre-optic methods, the output power as well as the power efficiency $\boldsymbol{\eta}$ can be calculated:

$$\eta = \frac{P_{out}}{P_{in}} * 100\% \tag{2.7}$$

where $\boldsymbol{P_{in}}$ the input electrical power can be measured by applying Hall-effect voltage and current sensor chips on the electronic control and drive systems of EM [75], or calculated by some other

sensorless control methods [76]. Alternatively, polarimetric FOS can monitor the current flow within the EM winding coils by surveying the nearby magnetic field [67, 68]. The operation principle is that the polarization of the light signal is proportional to the surrounding magnetic field, which is defined as the Faraday Effect. Theoretically, both mechanical and electrical powers of EM can be measured by FOS systems, therefore, the power efficiency of EMs can be evaluated without conventional electronic sensors.

2.2.6 Techniques for multi-parameter sensor network

In addition to multiple EM parameters sensor networks based on FOS measurement principles, the FOS multiplexing technique is another critical technique for the implementation of a practical sensor network, different from other mechanisms applied for quasi-distributed FOS and distributed FOS network construction [53].

For the quasi-distributed FOS (*i.e*. FBG array), the multiplexing method is the most significant and attractive feature to achieve large-scale sensor network implementation, considering the low-cost by sharing multiple channels over only one set of expensive supportive sensing components (e.g. laser light source, demodulator). There are three most commonly used types of multiplexing methods with variety of novel approaches reported for the FOS systems: time division multiplexing (TDM), frequency division multiplexing (FDM) and wavelength division multiplexing (WDM) [79]. They are commonly utilized for quasi-distributed (*i.e*. 'point') FOS especially FBGs or interferometric FOS systems. The first two methods (TDM and FDM) for FOS are similar to the conventional electronic methods, while WDM is specific for the FOS based on optical signal transmission. FDM can provide best sensing performance by applying more optical

components in terms of optical fibres, lasers and parallel demodulators, but this is not preferred in terms of a cost-efficiency tradeoff. TDM is realized using serial interrogation, thus only one demodulator is required. WDM can be used in combination with TDM to expand the sensing channel resolution, achieve long-range sensing and improve cost-effectiveness [80]. The choice of multiplexing scheme is circumstance specific, and it depends on the trade-offs between the sensing performance and the cost. For embedded EM parameter monitoring applications, the dominant cost is that of electro-optic components rather than the cost of optical fibres, considering limited optical fibre length required within a proper-sized EM for parameter monitoring. Therefore, the highest sensing resolution per laser light source is the criterion for selection of multiplexing scheme. Such a multiple channel setup proves the possibility for EM multiple parameter sensing by employing different demodulation mechanisms for monitoring of various EM parameters.

In addition to multiplexing methods, there are several optical ranging techniques required applied for conducting the locating function of the FOS system. Apart from the OTDR technique for distributed temperature sensor applications, other optical ranging techniques for distributed FOS include Optical Frequency-Domain Reflectometry (OFDR) [71, 72], Coherent OTDR [83] and Polarization-optical time-domain reflectometry [84]. The selection of optical ranging techniques depends on the targeted EM parameters and their sensing specifications (e.g. sensitivity, dynamic range, spatial resolution). The demodulation unit of distributed FOS is more complex and more expensive than that of the quasi-distributed FOS, while the spatial resolution of distributed FOS is lower. Therefore, the FBG array is the most popular FOS principle for EM multi-parameter monitoring with the benefits of high spatial resolution, cost-effectiveness tradeoff, and multiparameter sensing capability of FBG.

By employing a combination of various FOS working principles with corresponding networking techniques, it is possible to set up an integrated all-fibre optic sensing system for the EM multiple physical parameters monitoring. Such integrated multi-parameter FOS system may overcome the limitations of conventional sensors used for EM parameter monitoring, which are discussed in next section.

2.3 Conventional sensors for EM parameter monitoring

For physical EM parameters (such as temperature, speed and position, vibration and output power) there are two main methods for EM parameter monitoring: sensor-involved and sensorless. Most sensorless technologies employ the EM internal analogue or digital signal analysis combined with the EM control algorithms. For instance, motor current harmonics can be used to evaluate the EM internal temperature [85] and vibrations [86]. However, the sensing accuracy and applicable situations for sensorless methods are relatively limited compared to the sensor-involved ones, characterized by simplified model construction, multiple boundary condition assumptions and parameter uncertainty of sensorless methods would lead to errors or inaccuracy of target EM parameters. In this thesis the focus is on sensor-involved technologies rather than on sensorless calculations and estimation techniques.

Table 2.1. Targeted EM parameters and corresponding conventional monitoring methods and sensors.

EM parameter	**Temporal sensor system**	**Principles of Operation**	**Limitations**
Copper winding temperature	Thermocouples [87] RTDs[88] (i.e. thermistor) Infrared thermography[89]	Thermocouple: thermoelectric transducer effects (i.e. Seebeck effect and pyroelectric effect) RTDs: positive or negative temperature coefficient of electric resistance Infrared thermography: Infrared radiation combined with thermal detection or photonic detection	For TCs and RTDs: 1. Risk of overlooking local hot-spots 2. Sensor number limited by satisfied copper space factor and electric-magnetic field balance 3. Prone to EMI For IR thermography: IR thermography cannot be installed inside windings for precise hot-spot localization and temperature measurement
Rotor temperature	Static temperature measurement method Infrared thermography [89] Slip-ring signal transmission for contact temperature sensors	thermoelectric transducer effects (i.e. Seebeck effect and pyroelectric effect)	1. Lack of methods to achieve online & direct temperature monitoring of EM rotor 2. Complex installation and less robust 3. Prone to EMI
Vibration	Electric Accelerators[90]	Capacitive sensing **or** Piezoelectric effect	1. Complex installation (require high-standard pre-alignment)

	Eddy current sensor [91] Electromechanical based strain gauges [92]		2. Sensitive to ambient temperature 3. Susceptible to EMI[93]
Torque	Strain gages [94] combined with 1.Slip ring array (contact) **or** 2. Rotary transformer or RF telemetry (non-contact)	Bonded strain gage technology	1. Short lifetime 2. Costly 3. low signal-noise ratio 4. Complex installation
Rotational speed and position	Electric Encoder [95] **or** Resolver [96]	Electro-mechanical device converts angular motion to analogue/digital signal	1. Frequently regular hardware maintenance or replacement 2. Costly
Power efficiency	Ammeter+ voltmeter **or** Wattmeter [97]	Electric-magnetic field interaction effect Hall effect for current sensing	1. Complex (two types of transducers for just one parameter) 2. Affected by EMI 3. Compensation is mandatory for low power factor operation 4. Space occupation within EM control drive board

Table 2.1 lists commonly employed sensing systems for some of the primary EM parameters. In addition to the identified limitations, one significant challenge for the temporal separated EM monitoring sensor systems is that it is hard to construct one multi-parameter integrating sensing

system for EM physical parameter online monitoring due to the differences of sensing methods and supplementary components of sensors for each individual parameter. The presence of numerous sensors leads to the problems of installation complexity and high cost of the testing system.

To address these limitations, fibre-optic sensing technologies can be applied to exploit their obvious advantages. Only one type of sensor carrier (optical fibres) with small physical size (D<1 mm) regardless of the option of specific fibre-optic sensing principle, providing for the flexibility of sensor installation within EMs with insignificant modification on the original EM component spatial scheme. Secondly, good response to many physical variables can be achieved including thermal, mechanical and electrical quantities, providing the theoretical basis for fibre-optic based multi-parameter sensing system for EMs. Thirdly, high sensitivity and resolution are available for determining targeted sensing parameters by utilizing multiplexing techniques by in-situ fibre-optic sensor networks [79]. Lastly, sensing information is transmitted via optical signal that is immune to the complex EMI inside EMs. The research and development related to individual target parameters monitoring using FOS system, is discussed in the next section.

2.4 Modern FOS cases for EM parameters monitoring

2.4.1 Temperature monitoring

Thermal analysis and management of EMs are critical for machine performance and reliability guarantee. During the EM operation, undesired heat is generated from different types of heat sources (copper loss, iron loss, magnetic loss, etc.), and dealt with by designed heat paths and heat removal sinks [18]. However, overheating problem within the EM may still occur due to EM

operation failure or an inefficient cooling system. These thermal issues may lead to faster insulation degradation (EM life expectancy half reduction for 10℃ excessive of insulation class [98]), EM components failures such irreversible damage to EM and eventually whole EM breakdown. Therefore, overall online and continuous temperature measurement of the EM with high spatial resolution is necessary for EM health monitoring, the thermal data collected by sensors can also be used for EM thermal mapping construction and further EM thermal management design optimization [99].

Literature research on failed subassemblies of rotating electrical machines indicated that bearings, windings and rotors are the most vulnerable EM components to thermal problems [37]. The temperature distribution of bearings can be easily monitored through conventional electric sensors such as thermocouples since bearing is a motionless and external EM component, which is convenient for thermocouple installation.

The tricky parts for EM hardware temperature online monitoring are windings and rotors. Copper windings with multiple turns would carry electric current with current density about 5 A/mm^2, coiled within stator or rotor [100]. Such deep-buried windings usually suffer from the 'hot-spots' issues, which are hard to detect, and localized since thermocouple installation is limited as we have discussed. The unattended hot-spots may result in higher resistance and hence higher copper loss of windings, such vicious thermal cycles would increase the winding failure rate dramatically. Additionally, winding failure may lead to current/voltage unbalance and further undesired vibrations. In terms of rotor, it is an internal fast rotating component, which represents lack of accessibility for sensor implementation for online monitoring. Excepting the rotor winding hot-spot problem, rotors of different types of EMs would face various thermal problems: for

permanent-magnet synchronous motor (PMSM), its rotor is covered by permanent magnets (e.g. NdFeB, SmCo) without windings, such rare-earth magnets are highly sensitive to the temperature [101]. Local overheating concentration on the magnet will lead to irreversible demagnetization and hence torque generation reduction [102]. Additionally, rotor of high-speed EM will suffer the air fraction loss [103], which is a significant mechanical heat source for rotor temperature rise. The thermal problems of EM may also lead to material deformation and unbalanced placement of EM components, thus further lead to mechanical vibrations, acoustic noises and other mechanical problems.

FOS systems provide feasibility for online temperature monitoring of various EM components and subassemblies, considering characteristics of optical fibres including compact, dielectric and immunity to EMI. EM windings with FBG array embedded for temperature monitoring was developed [104]: by installing in-situ FBG array within different positions of windings, the hot-spots were successfully detected and located. Type-K thermocouples were embedded at FBGs corresponding positions for temperature measurement validation. The non-uniform thermal distribution (30 ℃ temperature difference for different positions) of copper windings was proved by FBG temperature sensors. FBG temperature sensor prototype with high spatial resolution and wound localization function of faulted windings [105], thermal ageing model of EM insulation life-time monitoring and prediction [106] were built based on the FBG array temperature sensors. Furthermore, a design concept and a prototype of a polyimide-coated Fibre Bragg Grating (FBG) array thermal sensor system was presented to perform a comprehensive 2-D real-time radial and axial thermal profiling and mapping of short duty cycle electric machine windings. Such systems, based on tunable laser technology, successfully demonstrated the advantages for FBG thermal

mapping of copper windings: broad temperature detection range (20 – 200 °C), adequate spatial resolution (6 cm) and fast wavelength sweeping frequency (up to 1 kHz) [107]. Simultaneous thermal maps can be used for real-time monitoring of the distribution and spatial localization of thermal hot spots within the EM copper windings.

Except pure optical FBG sensing technology, electric-optic hybrid sensing methods were employed for EM temperature monitoring: draw tower gratings (DTGs) combining with piezoelectric ceramic transducer was built for EM component temperature monitoring [108]. The thermal constant of the EM can be inferred by continuous winding temperature monitoring and the thermal data can be used for artificial intelligence algorithm training for EM control. In terms of EM rotor, compact FBG temperature sensors were attached on rotor, and with help of a multichannel optical rotating joint for signal transmission [109]. FBG strain simulation was designed since the FBG on the operating rotor was exposed to both thermal and mechanical effects [110]. The simulation results will cancel the thermal-strain cross effect of FBG and guarantee the accuracy of FBG temperature readings.

In addition to the EM subassemblies temperature monitoring, the FBG temperature sensors with fast response and adequate sensitivity were also employed for EM thermal analysis and to predict model construction. FBG array was applied for determining the relationship between mechanical / thermal losses and stator temperature increase of EM [111]. Copper/iron loss caused by an unbalanced voltage supply was proven to be the dominant factor for stator temperature increase rather than mechanical loss. With the base of temperature data collected by FBG array, a thermal and electrical simulation model of induction motor using the losses as input parameter was established [112].

Table 2.2. FOS cases used for EM thermal monitoring, including specific EM thermal parameters, FOS sensing principles and achieved metrological properties.

AUTHOR	EM PARAMETER	APPLIED FOS PRINCIPLE	METROLOGICAL PROPERTIES
Mohammed and Djurović, 2018[104]	Stator winding temperature	FBG	From 20 to110 ℃ Sensitivity: 10pm/℃ Temperature resolution: ±5℃
De Morais Sousa *et al.*, 2012[111]	Stator temperature	FBG	Up to 200 ℃ Temperature resolution: ±1℃ Sensitivity: 12pm/℃ Temporal resolution: 300 ms
Haramoni *et al.*, 2008[108]	Stator temperature	DTG+FBG + Tunable laser source	Sensitivity: 9.7 pm/℃ Temperature resolution: ±1℃
Duncan, Childers and Rajendran, 2004[113]	Stator + stator winding temperature	DFOS (weakly-reflecting FBG + OFDR)	Able to measure temperatures up to 200℃ Temperature resolution: ±1 ℃ Spatial resolution: 1 cm Sensitivity: 12pm/℃
Rajendran *et al.*, 2004[114]	Windings + end-windings temperature	DFOS (FBG+OFDR)	Able to measure temperatures up to 200℃ Temperature resolution: ±1 ℃ Spatial resolution: 1 cm Sensitivity: 12pm/℃
Hudon *et al.*, 2016[115]	Rotor field winding temperature	FBG	up to 129℃ Sensitivity: 10pm/℃
Boiarski *et al.*, 1995[116]	Switchgear, stator winding and rotor shaft temperature	DFOS (OTDR + Rayleigh)	Up to 150 ℃ Temperature resolution: ±5℃

			Spatial resolution: 10 cm Sensitivity: 12pm/℃
Mohammed *et al*., 2016[117]	Random wound components temperature	FBG	Up to 200 ℃ Temperature resolution: ±5℃ Spatial resolution: 10 cm Sensitivity: 11pm/℃
Zheng Ping, Pan Shiyong and Li Yong, 2005[118]	Rotor surface temperature	GaAs absorption spectral analysis	Non-contact Up to 200 ℃
Dreyer *et al*., 2018[119]	Stator core, slot and windings temperature	Multiplexed FBG	Able to measure temperature above 60 ℃ Temperature resolution: ±1.5 ℃ Spatial resolution: 10 cm Sensitivity: 10pm/℃
Wang *et al.*, 2011[120]	Stator bars temperature	FBG	From 20 to 110 ℃ Sensitivity: 10pm/℃
K. Sousa *et al.*, 2014[121]	Exciter bridge drive circuit temperature	FBG	Sensitivity: 10pm/℃

Other studies about using several types of FOS principles for EM thermal monitoring applications are listed in Table 2.2.

2.4.2 Vibration monitoring

Mechanical vibration analysis and diagnostics is another vital theme for EM performance monitoring. Like the heating of EM, vibration always exits during EM operation and the limits of normal vibration limit proportional to rotating speed [122] are defined in both IEC and NEMA

standards [114, 115]. Excessive vibration may be caused by faults from imbalance in several aspects: electro-magnetic (voltage/current unbalance, harmonics), mechanical (misalignment, component distortion and loose, overload) and other complicated hybrid reasons [125]. Additionally, the interplay between thermal problems and destructive vibrations always results in catastrophic strike on the reliability of EMs: the overheating of EM components may lead to insulation degradation and current imbalance, then eventually excessive vibration of the EM appears, vice-versa.

Vibrations above limit would lead to malfunctions of EMs, including the wear and failure of EM components, insulation degradation and undesired acoustic noise. The energy efficiency is also decayed by vibrations. The vulnerable EM components to vibrations are similar with those of thermal issues: bearing, winding, stator and rotor. Vibration diagnostic frequency spectral characteristics with the possible corresponding EM faults was summarized [126]. Generally, vibration sensors are required to collect the vibration signal spectral characteristics for fault diagnostics. Conventional electric accelerators or strain gauges have some obstacles restricting their reliability for EM vibration monitoring: prone to EMI, sensitive to ambient temperature, only aiming at bulky vibrating objects (low spatial resolution), and limited access for narrow space sensing [127]. These drawbacks of conventional vibration sensors set the challenge for precise vibration source localization and further vibration isolation.

FOS is a cost-effective method, which can measure the vibration signals thoroughly with high accuracy, since the FOS has advantages of compact and EMI immunity. Therefore, many different FOS principles were employed for EM vibration monitoring as discussed in previous section. Considering the contact vibration FOS, an in-line fibre etalon with FPI scheme (ILFE) [119, 120]

was proposed for voltage unbalance and harmonics detection of induction motor, FBG sensor system [119] as well as active FPI fibre optic sensor system were developed [130] to carry out simultaneous temperature & vibration monitoring of EM. There are other principles for EM vibration monitoring as well: reflective displacement FOS [131], extrinsic vibration FOS [123, 124], distributed vibration sensor [83], since mechanical vibrations can be presented by different types of physical quantities (e.g. acceleration, displacement and velocity).

Many novel FOS vibration sensors are designed and utilized for different components of EMs: stator vibration monitoring [125, 126], rotating shaft [136], magnetic core [137], winding overhang [138] and end windings [139]. Even a mature fibre optic accelerometer product is presented for market, for instance, by VibroSystm Inc [140]. The online monitoring of vibrations benefits the EM reliability: voltage imbalance and harmonics can be detected in a timely manner to prevent fatal faults in high-power machines [128]. The vibration data collected by FOS can also help to promote the EM feedback control system optimization [86].

2.4.3 Other EM parameters monitoring

Torque generated by a rotating shaft is the key parameter to evaluate performance as well as efficiency of EMs. Usually, the torque performance evaluation of an EM is completed during its prototype testing stages, the conventional torque transducers provide no simultaneous torque monitoring of an EM during its operation. FBG contact sensor is the critical and widely-employed FOS principle used for EM rotor torque monitoring [141], considering its uncomplicated and compact sensor setup: a pair of FBGs are attached on the surface of rotor shaft, each at a 45 degree angle relative to the shaft axis, to form the twist sensitive region for torque measurement. The

optical signal can be transmitted from internal rotor shaft to the outside optic demodulation module by single-mode fibre [141], rotary optical coupler [142] or coupling C-lenses [55] to minimize the optical signal attenuation led by rotation. Other FOS mechanisms except FBG are applied for mechanical torque monitoring, including sensors based on modulation of birefringence, electric-field or light polarization states, and stress refractive index [54]. However, these FOS systems with other supportive optical hardware required are not suitable for EM torque monitoring due to the space limit within EM.

Rotating speed is one of the EM parameters that are preferred to be monitored and controlled continuously during EM operation. Since the rotating speed of an EM is the most direct parameter to describe the performance of EM applications: such as the ground speed of aircraft or vehicle, the working conditions of wind turbine generators [143]. Like the reasons for other mechanical EM parameters, the FBG-based FOS is the most popular technique for EM rotating speed measurement: the core mechanism is converts the strain variation to rotation speed. Such rotating speed FOS systems require some support structures except optical fibre itself for speed monitoring, for instance, rotational disc with a metal rod [73], optical fibre collimators for better optical coupling [74]. Additionally, other principles including ring interferometric FOS with Rayleigh backscattering [144], reflective FOS with codewheel (i.e. fibre optic encoder) [145] and Sagnac interferometric FOS [146] are developed. All these fibre optic rotation sensing techniques suffer the problem of the ceiling of detectable rotating speed: The FBG and reflective FOS can detect the rotating speed no more than 5000 rpm [63, 64] while the advanced Sagnac FOS can only recognize maximum rotating speed about 100 °/ hour. None of them achieves the detection standard for high-speed (above 10000 rpm) EM speed monitoring so far. The future of FOS

rotating speed monitoring may be still depending on the development of FOS encoders or other developing sensing principles.

Other EM practical issues and parameters are monitored by employing FOS systems as well, including the EM's electric [138, 139] or magnetic fields [140, 141] (*i.e.* current, flux, and power), partial discharge detection [142, 143] and dynamic eccentricity monitoring [153]. For the electric field and magnetic field monitoring, FOS systems stand out due to their intrinsic advantage of EMI immunity, additionally, the real-time monitoring of EM power efficiency can be realized with help of electric field FOS, by using the method shown in Equation (2.6) and (2.7). The magnetic field of the EM also is one of the indicators of its health condition: FBG strain sensor with magnetic-sensitive material coated was employed within EM for demagnetization monitoring of rotor permanent-magnet [154]. In terms of partial discharge (PD) detection, it can be used to monitor and predict the insulation degradation in the EM. For dynamic eccentricity monitoring, it can be used to check the assembly and alignment conditions among EM components and prevent undesired mechanical vibrations.

To sum up, optical fiber-based sensor technology offers the possibility of developing a variety of physical sensors for a wide range of physical parameters. In addition, the real-time monitoring feature of FOS allows an entire EM system to complete troubleshooting. The development and construction of modern FOS integrated systems are of great significance for further structural health management for EMs and their applications [155]. A FOS system with low-physical profile and high EMI can rapidly detect and collect sufficient internal structural data of various EM parameters, which is not possible to be achieved by conventional sensors. These data would help for EM predictable aging model construction as well as the EM control algorithms optimization,

which are both useful tools for 'foreseen maintenance' to predict and reduce the electric machinery faults degree [156].

2.5 Challenges of using FOS for EM monitoring

There are still several implementation challenges for optimization of integrated FOS systems for EM monitoring. The first and significant one is that of **time-scales**: target parameters are measured in different time scales with various amplitudes. Therefore, the required demodulation rate of integrated FOS system is hard to be defined and achieved. Table 2.3 below indicates general specification range of the target EM physical parameters.

Table 2.3. General EM reliability physical parameters & their specification range [113, 114][157].

Parameter / **Specs**	**Insulation class temperature range**	**Mechanical vibrations**	**Torque**	**Rotating speed & Position**
Coverage amplitude range	25~200 ℃	0~1 mm (by displacement) upper limit:39.2 mm/s^2 (by acceleration)	0~500 N·m (continuously increasing with power supply)	3000~20000 rpm (314~2094 rad/s)
Accuracy	±5 ℃	± 5 % for instant corresponding value	± 5 % for instant correspondin g value	± 5 % for instant corresponding value
Sensitivity	±5 %	±5 %	±5 %	±5 %

Spatial resolution	10 cm	Flexible (For conventional piezo electronic sensor, 2 sets (x, y, z axis for each set) on both ends of shaft bearing, minimum 6 sensors in total)	/	/
Frequency domain	1-10 Hz	50~500 Hz	1-10 Hz	50~300 Hz (derived from the rotation speed range above)
Related subassemblies of EM	Stator (mainly stator windings) Rotor Bearing	Stator core & windings Rotor Shaft Bearing	Rotor shaft	Rotor shaft

Table 2.3 above indicates that the frequency domain for each target parameter is quite different, which represents that the optical signals (or the converted electronic signals) would require various bandwidths of demodulation module to finish the sensing task. It may be very difficult to achieve multiple parameter sensing with only single optical fibre path through one demodulation channel. Several optical fibres are needed to be responsible for multiple EM parameter sensing. Ideally, different kinds of FOS principles (e.g. FBG, interferometric, distributed, reflective FOS) can be integrated together within such FOS system so that each FOS mechanism can focus on the corresponding target parameter monitoring. However, the hardware (e.g. light source, demodulation scheme) for each type of FOS principle differ dramatically, for instance, the FBG sensor requires a broadband or tunable laser source while DFOS needs pulsed laser as light source. Therefore, even with a wide range of FOS principles used for EM monitoring, one most

appropriate FOS principle with wide sensing parameter applicability should be chosen to construct our proposed highly integrated FOS sensor system for EM monitoring in this project.

Most EM parameters were measured simultaneously using FBG sensors installed on an EM in the test bench [29] as mentioned in previous section. The measured parameters included mechanical vibration, rotor speed, torque, and direction of rotation, temperature distribution along the stator windings and on the rotor surface. A FBG-based sensor may be considered as the most suitable mechanism for EM multi-parameter monitoring: sensitive to both temperature and strain, quasi-distributed sensing, customizable sensor layout design, compact and simple sensor setup, and fast optic spectral response. However, the **cross-effect of FBG** temperature and strain sensitivity will be the top issues which need to be solved for our proposed FBG sensor system. Generally, the FBG cross-sensitivity can be divided theoretically by setting an additional reference FBG sensor: by matrix calculation, the contribution of each sensitivity (temperature and strain sensitivities of FBG1 and FBG2) to the overall sensor wavelength shift can be identified, and therefore the variation of temperature and strain can be determined separately [158]. Another issue is the FOS performance limitation due to immature sensor technologies: including the measuring span and the accuracy. For instance, the monitoring of a high-speed rotating part is always a challenge for both mounting strength and frequency resolution of FOS: currently no FOS systems can achieve reliable rotating speed monitoring over 10k rpm.

The second systematic challenge is the **implementation positions and packaging** issues of FOS. As discussed in the previous section, many FOS systems are contact sensors and attached with pastes or glue on the EM component's surface, which is quite hard to remove and manufactured in a portable system for monitoring other EMs. Additionally, the free space inside EM is quite

limited (e.g. air-gap about 1mm), combing the internal structure deformation caused by EM operation, the implementation method of FOS for EM should be considered in advance to ensure the proper operation of FOS. In addition, the sensing carrier of intrinsic FOS system is optical fibre, which presents fragility issues where strong mechanical stresses or bending are applied. The external package will be required for optical fibres when they are installed within EM components, for instance, a Teflon tube was employed for FBG thermal sensor to investigate the thermal field within EM copper windings [159]. In addition, extensive experimental data and prediction modelling results of various EM parameters are required to determine the optimal positions of FOSs installed on or within EMs.

Another problem is the **integration of whole FOS system**. The tunable laser or demodulation modules used in the lab are of relatively large size and weight. Since the spectral analysis techniques are mostly accepted in industrial FOS systems, the high-cost of the spectral interrogator will limit the promotion of FOS used for EM monitoring. Fortunately, it still depends on the application scenarios of EMs: for instance, in terms of the EMs for aerospace an aviation applications, safety and reliability will be the first consideration rather than cost. The research in the future would focus on highly integrated [160] and low cost optical devices (e.g. butterfly tunable laser module) for portable FOS multi-parameter sensing system construction with flexibility.

To sum up, FBG-based fibre optic sensors will be considered as the most suitable techniques for EM monitoring regarding its characteristics mentioned above. Nevertheless, there are still some practical engineering issues for FBG sensors implemented within EMs in terms of sensor implementation, maintenance, and integration.

2.6 Machine learning (ML) algorithms used for EM monitoring

Multiple types of sensors used for different EM physical parameter monitoring (temperature, vibration, rotating speed, torque etc.) were reviewed and discussed in previous section, including both conventional electric or mechanical sensors and advanced fibre optic sensor systems. The comparison between conventional and FOS methods were made, which reveals the advantages of a FOS system used for EM monitoring.

However, there are still several obstacles regarding the construction of an integrated FOS system for online EM parameters monitoring, as we discussed at the end of the last section. We need to find a solution for these sensor implementation, integration and maintenance issues. Additionally, the optimization of sensor layout design should be considered. We still need to solve the following questions for instance: How to use optimal number of sensors to for comprehensive monitoring of EMs? How to achieve ex-situ thermal sensing of EMs?

Machine learning combined with FBG sensors will beis a method worth trying. In recent years, machine learning algorithms [24] have been widely employed for sequential forecasting, fault prognostics and condition monitoring of electric machines [153, 154] and relative industrial applications [155, 156]. In our project, ML algorithms may help sensor users to avoid some intrinsic defects of FBG sensors: the relation of target EM parameters and FBG spectral data can be trained and matched automatically by ML models, unlike the conventional FBG sensing data demodulation method, the cross-effect of FBG sensor may be cancelled and fixed by ML algorithms based on large-scale and well-organized training datasets. The details of sensor prototypes construction and validation will be presented in the following chapters of this thesis.

Therefore, after the literature review of FOS techniques and ML algorithms, we will propose a solution to answer the research questions mentioned in Chapter 1:

Potential Solution of the research questions:

Combining multi-sensor system (FBG sensor as the core sensing technique) of EM with machine learning models to achieve accurate and comprehensive thermal monitoring of EMs. The sensor prototypes of proposed solution must be constructed and validated progressively.

2.7 Conceptual framework of research

To complete the proposed novel FBG-ML monitoring system, a conceptual framework of this PhD project needs to be presented in advance (Figure 2.3): the main objective is monitoring the thermal distribution of EM, therefore our thermal sensor prototypes should be constructed and validated step by step as follows:

- FBG sensor thermal EXPs: Proof-of-concept
- FBG sensor thermal EXPs on copper windings
- FBG sensor thermal EXPs on motorette
- FBG sensor thermal EXPs on operating EM

A novel modern FBG sensor system design and implementation should be completed through along this PhD project for EM thermal monitoring. At the beginning stage, a simplified FBG temperature sensor prototype required to be constructed and tested to explore and demonstrate the feasibility of our proposed new concept: using FBG sensors for thermal monitoring of electric

machines. For the proof-of-concept stage, the planned object under test (OUT) should be simple and easy for sensor installation and dismounting. Here we planned to employ ceramic power resistors as the OUT at proof-of-concept experiment stage. Additionally, the FBG sensor system should be designed and implemented in terms of both hardware (component devices) and software (raw sensory data processing algorithm).

Once the feasibility of FBG sensor for thermal monitoring has been demonstrated and verified, our experimental design should move to next stage. The OUT will be updated to bare enameled copper windings, and then motorette [165], a physical model represents an equivalent, complete EM winding system. A typical motorette model consists of a multi-slots steel frame with EM copper windings embedded in slots as EM design scheme. The design and implementation of FBG sensor prototypes of copper windings and motorette, with multiple duty-cycle modes of actual EM operations [166] applied will be the interim experimental stage of our project. In addition, machine learning algorithms will be introduced to conduct some sensor number optimization tasks. The construction of initial versions of ML models can be considered as the proof-of-concept modelling of ML algorithms used in our EM thermal monitoring applications.

The final and vital experimental stage of this project is to achieve comprehensive thermal monitoring of operating EM using FBG sensors with various ML algorithms. A validated, lab-version prototype of our FBG-ML thermal monitoring system for EMs will be presented with details as a disclosure of this PhD project.

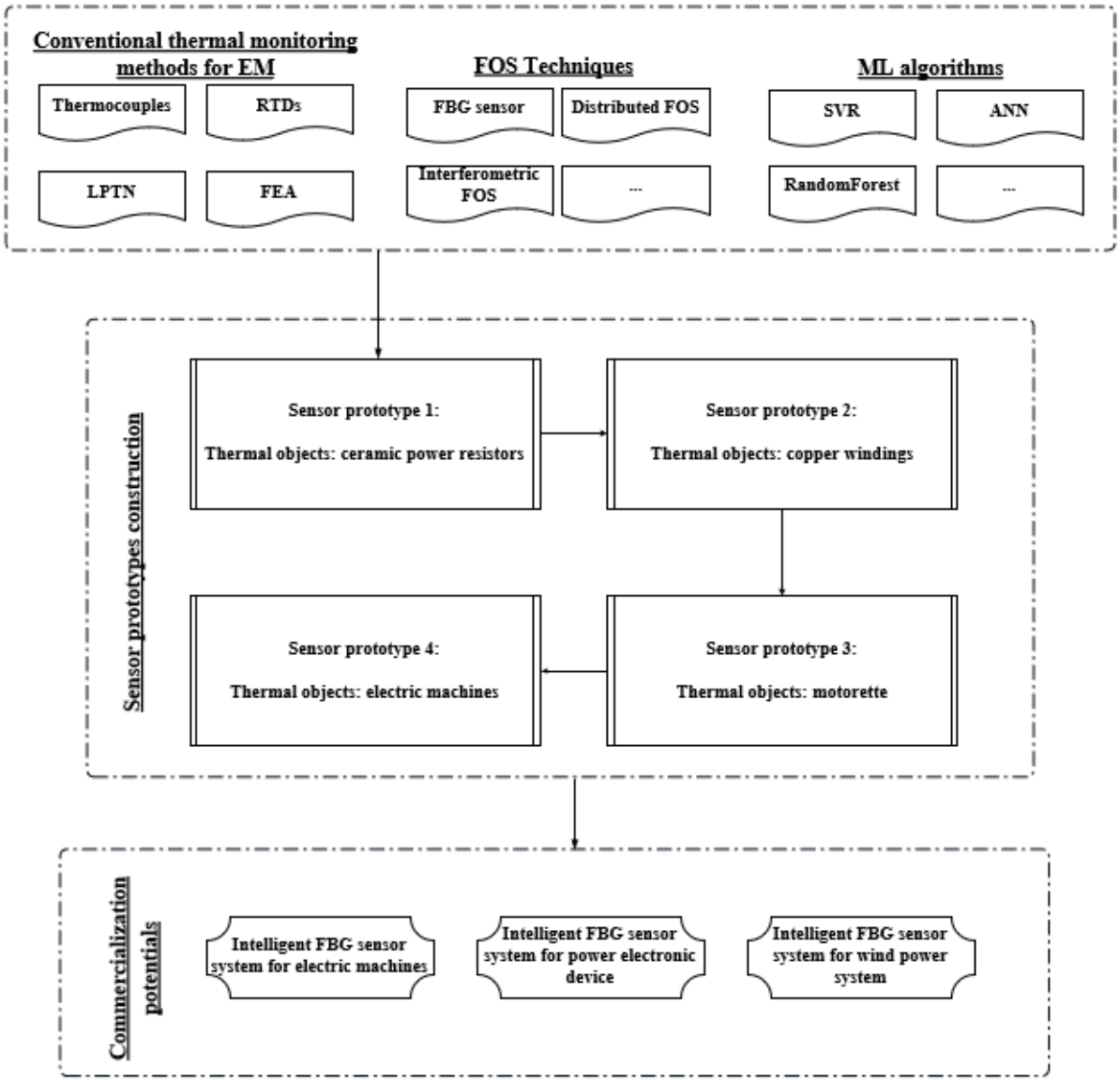

Figure 2.3. Conceptual framework diagram of PhD research project.

2.8 Organization of this thesis

This PhD project thesis has been organized and presented systematically, with thesis structure framework shown in Figure 2.4. The brief state-of-the-art review of EM thermal monitoring methods and the temporal research gaps will be outlined and discussed in Chapter 1. Then, the

literature review and theoretical research for FBG sensor system for EM will be investigated in Chapter 2, which was divided into three sections: review of conventional EM thermal monitoring methods, fibre optic sensors used for EM monitoring, and ML algorithms used for EM monitoring. After the comprehensive literature review and sensing technology analysis, we presented a novel EM thermal sensor system design that combines FBG sensing technology and ML algorithms at the end of Chapter 2. For the validation of proposed intelligent FBG-ML sensor system design, the experimental validation has been conducted and presented from Chapter 3 to Chapter 6. The FBG sensing prototypes were designed, implemented, and validated progressively by alternating the target thermal objects: ceramic power resistors (Chapter 2), enameled copper windings (Chapter 3), motorette (Chapter 4), and eventually electric machine (Chapter 6). Finally, this PhD project has been concluded in Chapter 7, additionally, the limitations, future work directions and commercialization translational potentials of this PhD project has been discussed and presented.

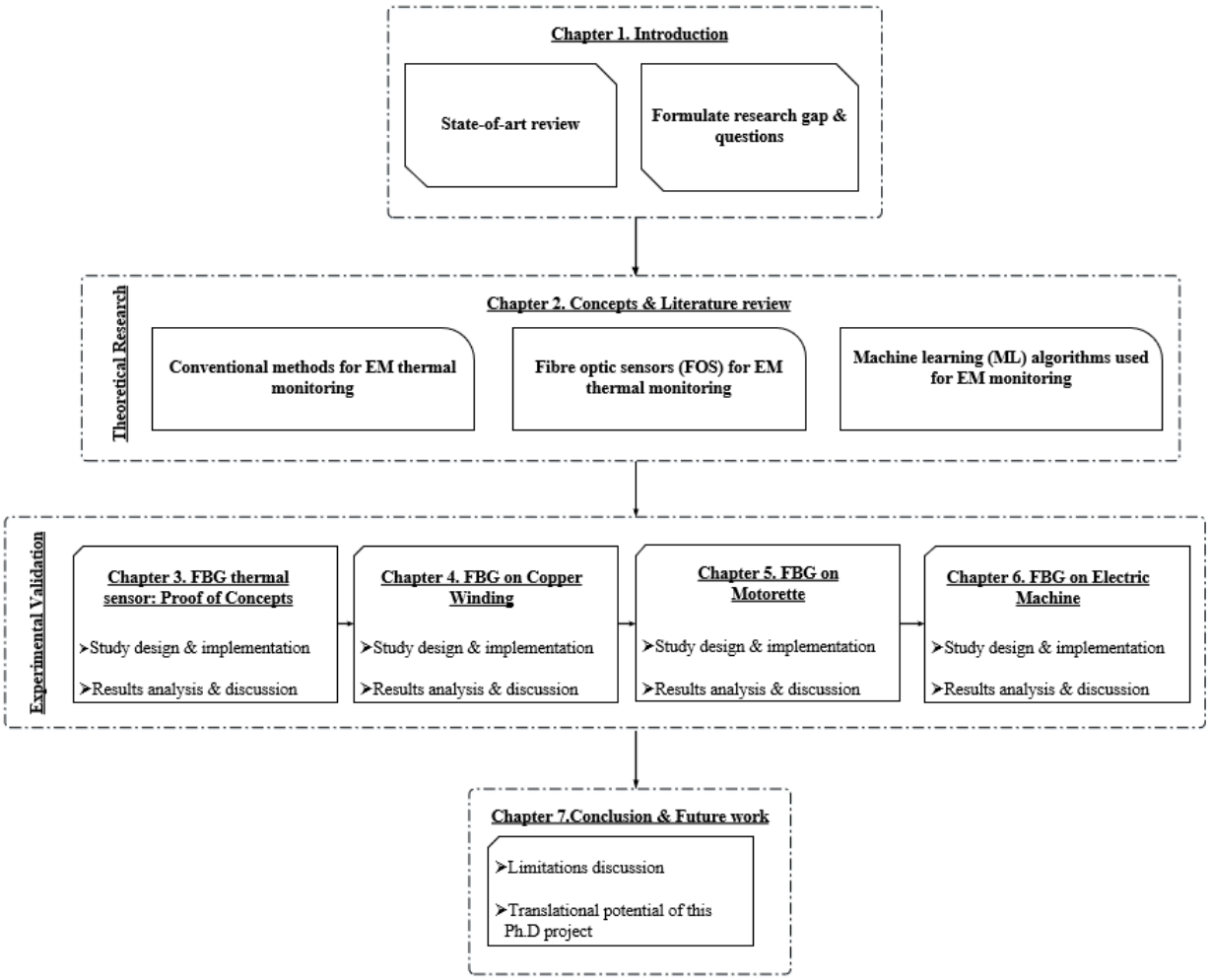

Figure 2.4. Structure of thesis organization with the key points of each chapter.

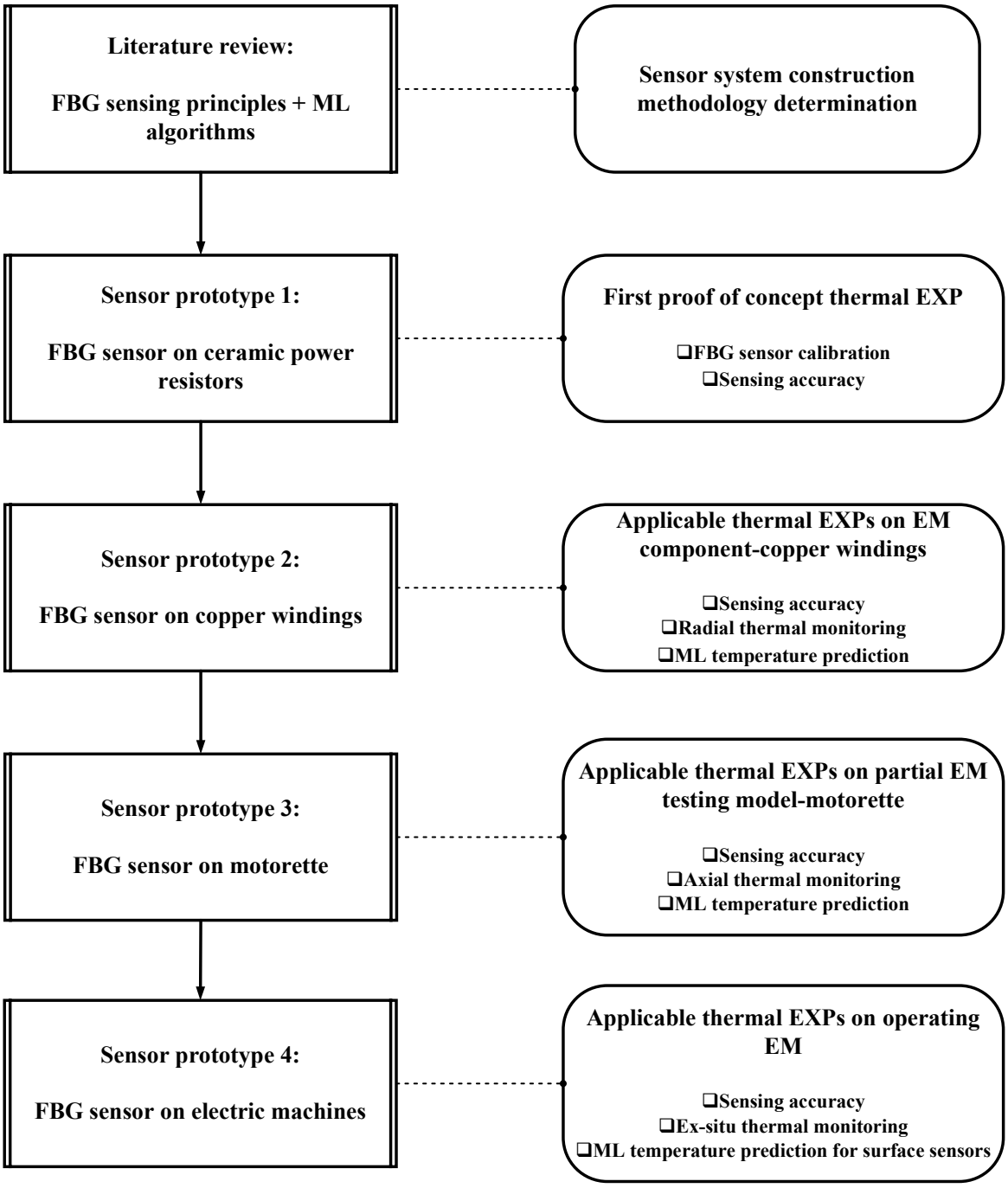

Figure 2.5. The study design flowchart of the PhD project. Literature review will be conducted for the sensor system methodology completion, then several versions of thermal sensor prototypes

with different target objects will be constructed and validated step by step. The objectives of each sensor prototype version were listed in the corresponding right-side box.

The study design structure of the "body chapters" in this thesis was shown in Figure 2.5. Four versions of sensor prototypes will be designed and validated progressively with different objectives. For instance, regarding the first FBG sensor prototype, the calibration of sensor and sensing accuracy validation will be the prime tasks to be verified. From the stage of thermal EXPs on copper windings, the ML algorithms will be introduced for their temperature prediction performance evaluation. As the target thermal objects became more complicated, the final sensor prototype will be able to achieve comprehensive thermal monitoring of EM using optimized sensor number with machine learning algorithms employed.

3 Basic principles and the proof-of-concept for FBG temperature measurements

In this chapter, as we planned, the proof-of-concept FBG sensor thermal experiments will be designed and implemented. Several versions of experimental prototypes with their measurement results were displayed. For each version, system schematic design, experimental procedure, test-rig implementation, and results analysis were included. More importantly, the improvements of new version compared to the previous one will be explained in terms of both hardware and modelling aspects. Ceramic power resistors were chosen as the OUTs at this early stage of experimental validation. It is necessary to build such physical "toy" prototypes before we implement our FBG thermal monitoring system within operating electric machines, it shall be helpful to check the feasibility and reliability of our sensor design hypothesis: using FBG sensor for EM thermal monitoring.

3.1 FBG with Power resistors: thermal experiment V1.0

The first version of proof-of-concept thermal experiment will be presented in this section, including study design, prototype construction and experimental results analysis.

Study Design

FBG temperature sensor is chosen as our sensing method for temperature monitoring considering its spatial resolution superior for heat spot location task. The schematic design of first version prototype is shown in Figure 3.1.

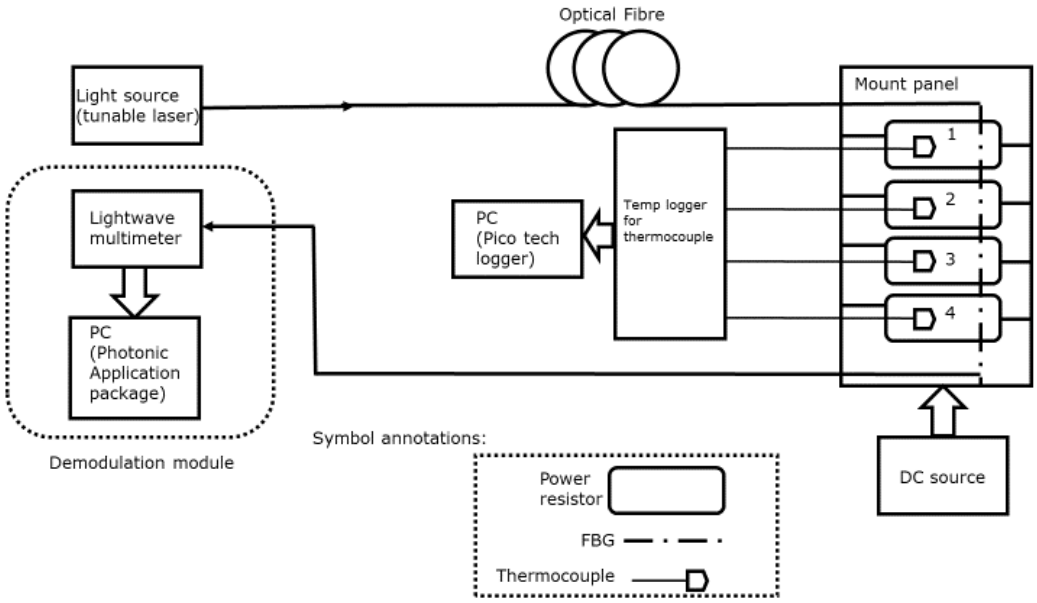

Figure 3.1. Schematic of FBG based temperature measurement prototype V1.0 design. In our first version design, Agilent tunable laser 81960A is employed as light source and demodulation module includes Agilent light wave multimeter N7745 and its corresponding Keysight Insertion loss Engine (IL Engine) software for spectral to temperature conversion. In this setup, thermocouples and FBGs are both used for temperature monitoring while thermocouples with its logger are employed as reference measuring technique to check the performance of our FBG temperature monitoring system.

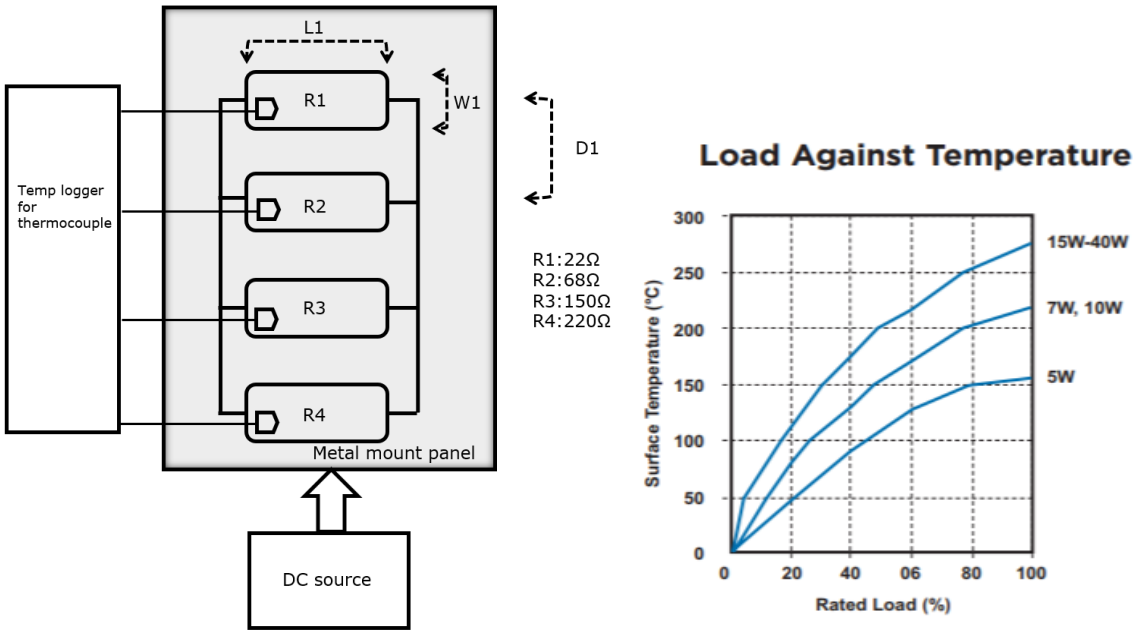

a) b)

Figure 3.2. a) Schematic design of four heat objects on a metal mount panel. b) Ceramic power resistors T-load curves from TE connectivity SQ series datasheet.

To achieve temperature gradient for four resistors **R1~R4**, we choose four resistors with same product type (TE connectivity SQ series [167]) and all other parameters except resistance. With one DC source connected in parallel, the load power for each resistor will be different and so as their surface temperatures, which is shown in Figure 3.2.

Applying $i = 1,2,3,4$ to label four power resistors, we have:

$$V_1 \sim V_4 = V_{DC}, I_1 \sim I_4 = \frac{V_{DC}}{R_i}, P_1 \sim P_4 = \frac{V_{DC}^2}{R_i}$$

Therefore, for four resistors with different resistances, we can obtain four different temperature points presented with range covering 20~200 ℃ by adjusting the DC voltage supply. To be noticed, metal mount panel should be covered by heat insulation materials (e.g. ceramic fibre paper). Besides, L1=5cm, W1=4cm, D1=10cm for resistor position arrangement.

Test Rig Construction & Experimental Conduction

Since the schematic design of the FBG sensor system was completed, the experimental procedure based on the experimental design should be described here with following steps shown in Table 3.1:

Table 3.1. Steps for proof-of-concept thermal experiment: FBG on power resistors test bench. The procedure was designed for the setup schematic shown in Figure 3.1.

Experimental procedure of "Power Resistors test-rig"
1. Set up the experimental prototype based on the schematic design above. Each power resistor will be measured by both a thermocouple and an FBG temperature sensor simultaneously.
2. Switch on the DC power supply, record the voltage supply $\boldsymbol{V_{DC}}$, current supply $\boldsymbol{I_{DC}}$ and corresponding temperature reading from thermocouple $\boldsymbol{T_{tc}}$ and loss optical spectrum of FBGs by IL engine software.
3. Adjust the power resistor surface temperatures by varying DC supply. Record the new voltage supply $\boldsymbol{V_{DC}}$, current supply $\boldsymbol{I_{DC}}$ and corresponding temperature reading from thermocouple $\boldsymbol{T_{tc}}$ and loss optical spectrum of FBGs by IL engine software.
4. Repeat 2 &3, till the DV supply covers the range from 5V to 22V with 1V step.
5. Read the loss optical spectrum of FBGs, find the central wavelength shift $\boldsymbol{\Delta\lambda}$ manually, convert the spectral data to temperature reading $\boldsymbol{T_{FBG}}$ with known room temperature $\boldsymbol{T_{ref}}$ and its corresponding central wavelength $\boldsymbol{\lambda_{ref}}$: $\boldsymbol{T_{FBG} = T_{ref} + \Delta\lambda / t_{coe}}$, where $\boldsymbol{t_{coe}}$ is the thermal sensitivity of FBG, for silica FBG, it around 10 pm/℃.
6. Plot graphs to $\boldsymbol{T_{FBG}}$ and $\boldsymbol{T_{tc}}$ under same conditions, check the validity of FBG temperature sensing method.

The power resistor test rig based was implemented (Figure 3.3) for thermal experiments conductions. The OUTs and devices used for construction followed our previous design.

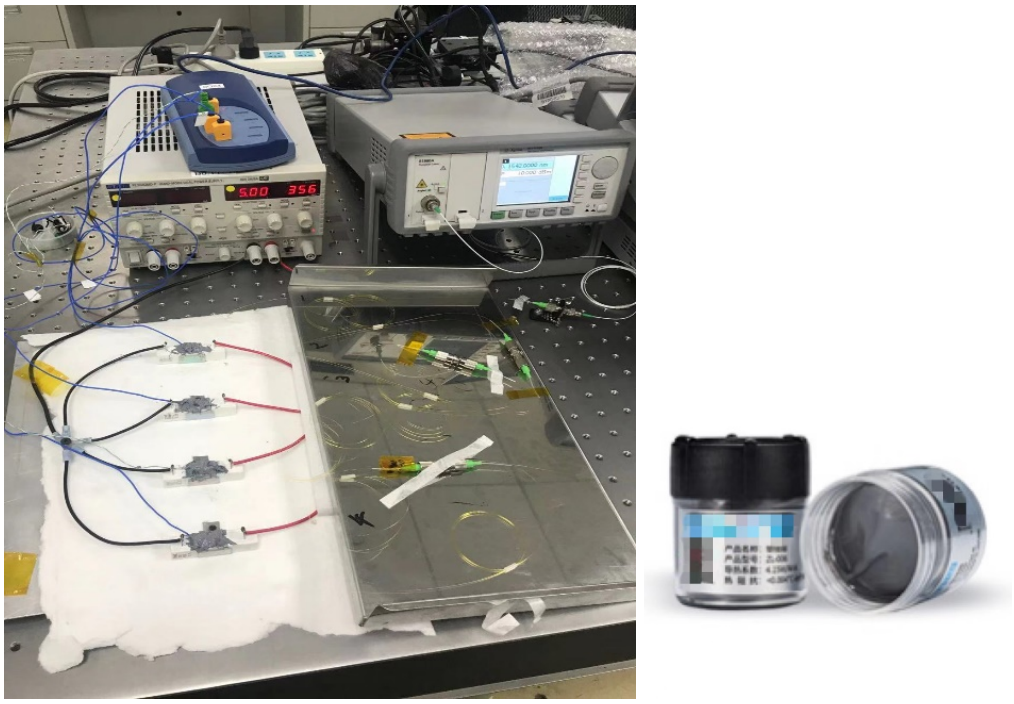

a) *b)*

Figure 3.3. a) Photo of experimental setup of temperature monitoring prototype V1.0 with thermal paste b) placed on the surfaces of four power resistors. The thermal conductivity of the thermal paste is about 4.15 W/(m·K), which can help to create a uniform thermal environment of resistor surfaces and provide tight contact between sensors and resistors. Both FBGs and thermocouples are placed within the thermal paste, therefore, theoretically, the thermocouple and FBG at same resistor surface may be under same temperature. By comparing the temperature readings of thermocouples and FBGs, the performance of our FBG thermal sensing system can be evaluated.

Results & Discussion

The temperature plots of design test bench were shown in Figure 3.4 proved the validity of our prototype design as well as the FBG temperature sensing method. Our first version of prototype can provide four heat points covering 23~190 ℃ with temperature gradient. High correlation between thermocouple measured and FBG measured temperatures with error within ±5 ℃ is shown in Figure 3.4-c). However, there were undesired temperature fluctuations at position_2 when the DC power supply value was tuned to 20 and 21 volts, both TC and FBG sensors were able to capture such variation. It has been found that the fluctuation was led by the poor contact between resistor and DC power supply. Additionally, combing the FBG spectral characteristics shown in Figure 3.4-b) with temperature comparison plot c), we found that temperature variation is proportional to the central wavelength shift, which agreed with the sensing principle of FBG temperature sensor.

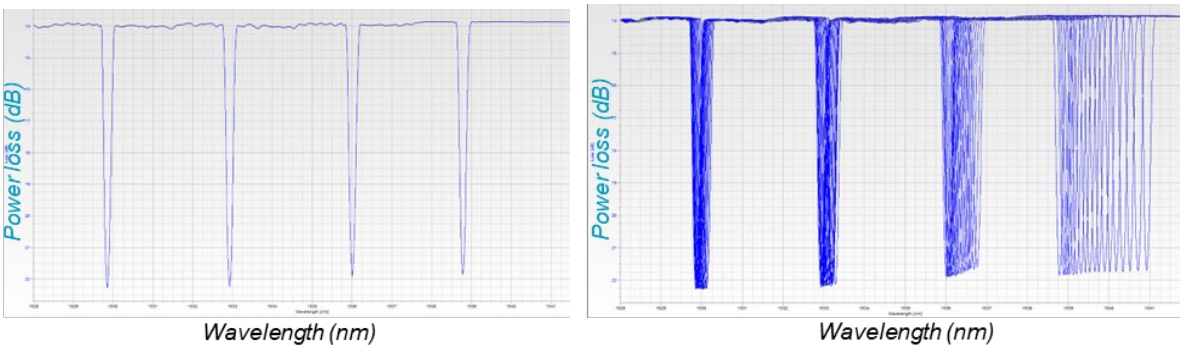

a) ***b)***

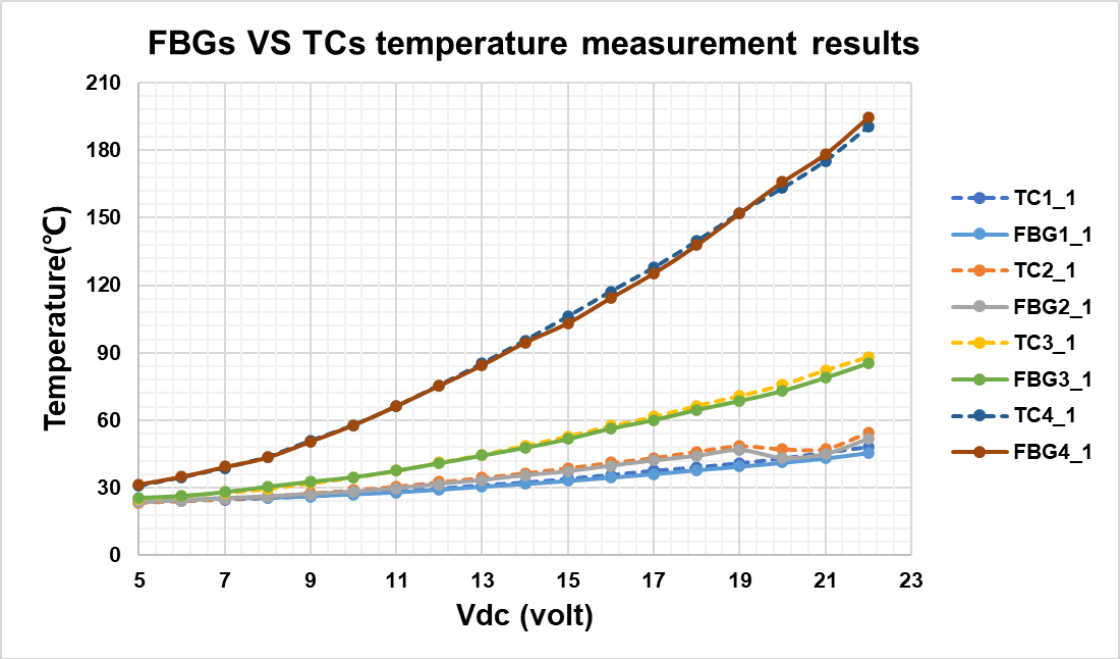

c)

Figure 3.4**.** A set of temperature sensing results of prototype V1.0: a) Intensity-wavelength spectral of four FBG sensors at room temperature 23 ℃, while b) presents a set of central wavelength shifts of four FBG sensors as resistor surface temperatures were adjusted by varying DC supply. c) Plot of temperature measurements of both thermocouples and FBGs at four different power resistors with varying power supply labelled by DC voltage source values in x-axis. FBG with Power resistors: thermal experiment V1.1

We have successfully measured the temperature with high accuracy within 23~190 ℃ in our first version prototype. However, one big drawback of prototype V1.0 is that the temperature reading measured by FBGs cannot be displayed simultaneously. Temperature readings measured by FBGs

were calculated after we obtained and analyzed the FBG spectral characteristics, which is very inefficient and not acceptable for an EM online thermal monitoring system.

For improving the demodulation efficiency of our FBG thermal sensing system, a self-written novel demodulation program with Matlab software was developed (check the detailed code with comments in *Appendix-1. Matlab code for FBG sensor demodulation*). It can invoke optical spectral information back to Matlab program for data analysis & temperature demodulation. A simple temperature-sensitivity test of this program was shown in Figure 3.5. Therefore, a complete real-time multi-points temperature measurement by FBGs can be finished by fully Matlab control with both CWs of FBGs and demodulated temperature readings displayed for users (Figure 3.6). The experimental procedure and hardware setup of V1.1 is exactly same as V1.0, with only demodulation program improved. There is no more post-data analysis required for our FBG temperature sensing setup.

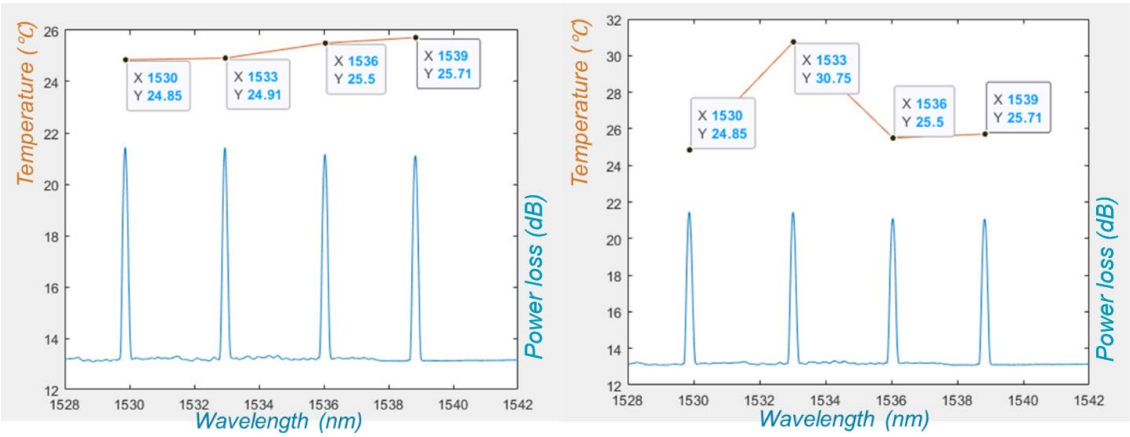

a) b)

Figure 3.5. Testing of self-programming code for FBG central wavelengths demodulation. Where X-axis presented wavelength and Y-axis presented the optical power loss in dB for blue spectrum curve while temperature in ℃ for orange measurand curve. We held FBG_2 by hand and left others at room temperature at 25 ℃. It can be observed that an increased temperature value of FBG_2 (~ 30.75℃), which proved the program is well-functioning with temperature variation captured.

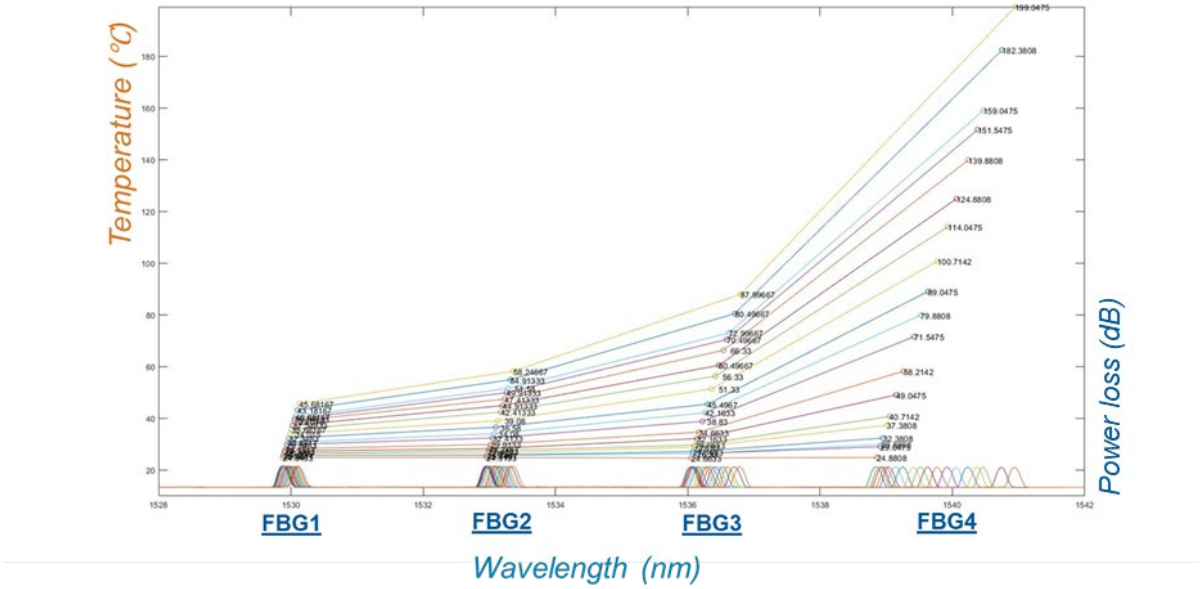

Figure 3.6. FBG temperature measurement display window by Matlab. FBG spectral power loss of four FBGs on four power resistors are shown at bottom & their corresponding demodulated FBG temperature values are shown above. Four temperature values connected in the same solid line represents the 4 different power resistors' temperature measured by FBGs with one fixed DC source applied. By adjusting the DC supply, we obtained several sets of temperature data at different DC supply.

3.2 FBG with Power resistors: thermal experiment V2.0

The second version of proof-of-concept thermal experiment will be presented in this section, including study design, prototype construction and experimental results analysis. Compared to the previous sensor prototype, the improvement of FBG demodulation hardware will be the main update of the sensor prototype.

Study Design

Real-time temperature measurement of multiple points using FBG sensors can be completed by prototype V1.1 with self-written Matlab program. However, the real-time temperature measurement speed is limited by the lab-level devices: In our prototype V1.1, once complete temperature measurement process takes about 11 seconds (i.e. 0.09 Hz), which is the intrinsic limitation caused by the scanning frequency of Agilent tunable laser 81960A and light wave multimeter N7745 products. Such demodulation speed is sufficient for general EM static thermal health monitoring. However, considering other dynamic EM thermal field monitoring conditions, for instance, monitoring copper winding temperature field rising distribution at EM start-stage, such speed is far from the required data acquisition rate, which is at least 1 Hz scanning frequency for sufficient temperature sampling rate for electric machines. To achieve such high canning frequency of FBG sensors, we need to employ an optical device called FBG interrogator with internal design shown in Figure 3.7, and the new FBG thermal sensing schematic design with FBG interrogator is shown in Figure 3.8.

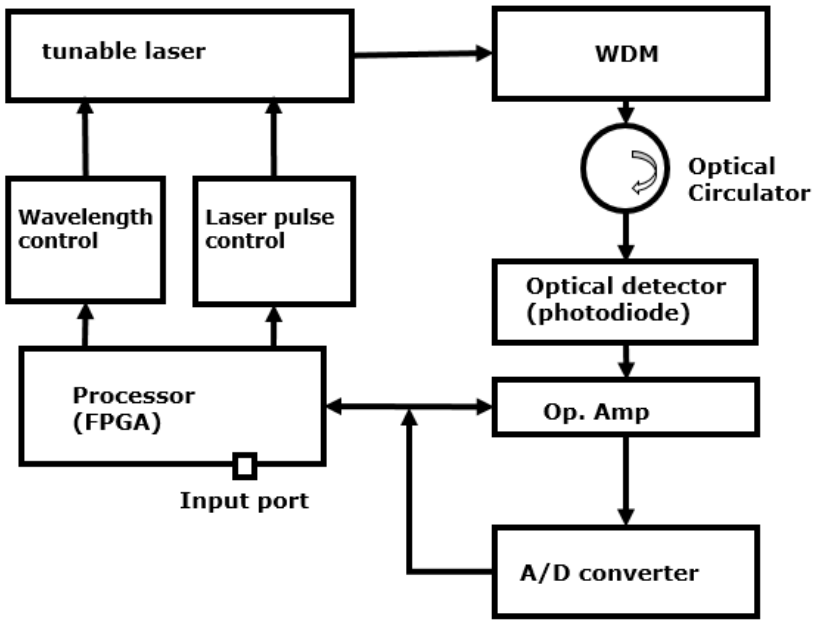

Figure 3.7. Detailed structure of FBG interrogator demodulation module by Arcadia Optronix Inc [168]. The demodulation module of Arcadia FBG interrogator employs WDM technique with fast FPGA processor for tunable laser control. With the help of WDM and high-speed processor, it is capable of outputting "multiple laser pulses at multiple wavelength" simultaneously, combing with the spectral peak-tracking algorithm, this demodulation module can determine the FBG central wavelengths with maximum speed 1 kHz each channel. This WDM demodulation method is much faster than V1.1 setup using "step by step wavelength scanning for whole bandwidth".

For the validation of new version of FBG sensor system with FBG interrogator product introduced, thermal experiment V2.0 were introduced: four power resistors were connected in parallel to resemble distributed heat spots. Four power resistors from Tyco Electronics [167] with electric resistances of 220Ω, 150Ω, 68Ω, 22Ω, respectively, and were arranged in parallel and labelled as resistor 1 to 4. This arrangement resembles four different heating powers, and therefore result in different surface temperatures. Our design covered the range of 20-200℃ for temperature

measurement. The power resistors were chosen to mimic practical heating power range of one stator tooth of EM windings with a natural air-cooling system, representing heating power range from 1 to 20 watts. Both the FBG sensors and TCs were fixed on the surfaces of each power resistor for temperature monitoring and the validation of FBG measurements.

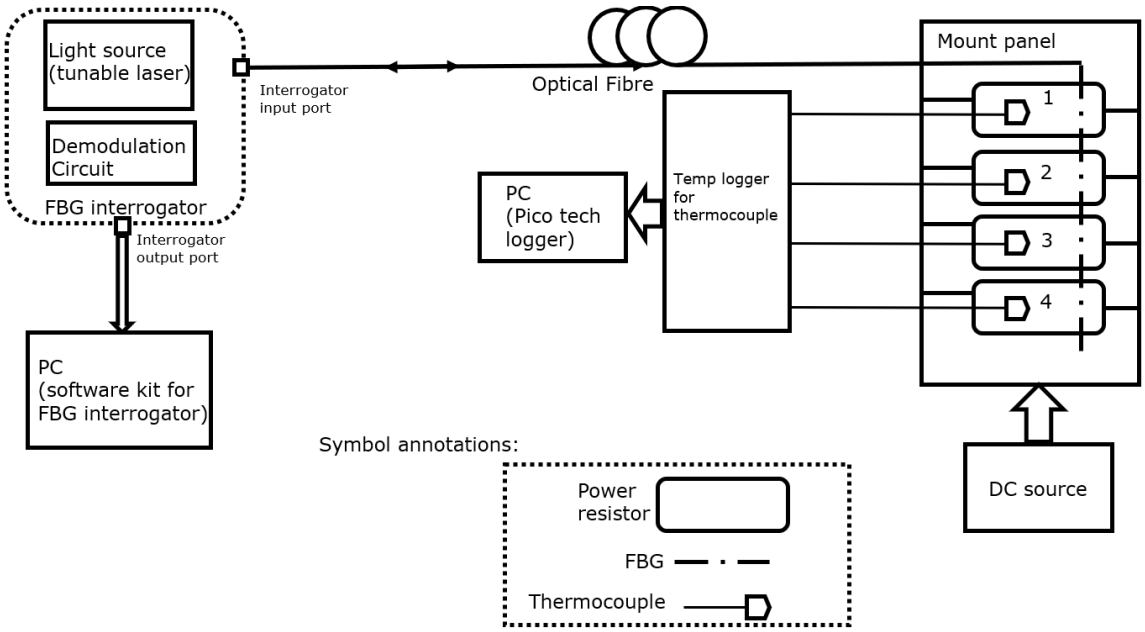

Figure 3.8. Schematic of FBG based temperature measurement prototype V2.0 design. Compared to the previous version, power resistor (heat point) board, thermocouples are exactly same setup. Only the demodulation module for FBG changed from: "Agilent tunable laser and light wave multimeter +Matlab Demodulation Program" to "FBG interrogator product+ its own software kit". The FBG interrogator product purchased from Arcadia Optronix can provide maximum 1kHz scanning frequency with 8 independent operating channels, each channel has maximum capacity of 30 FBG sensors. Therefore, theoretically, maximum 240 temperature values measured by FBGs can be calculated & displayed on the PC every 1ms, which is much faster.

The temperature measurement procedure of V2.0 is similar with that of V1.0 but more efficient. Once we finished the FBG interrogator software initial settings based on our FBG sensors, The FBG interrogator will record all the temperature readings measured by FBG sensors automatically and directly with large amount of data due to the high scanning frequency. The constructed sensor prototype is shown in Figure 3.9.

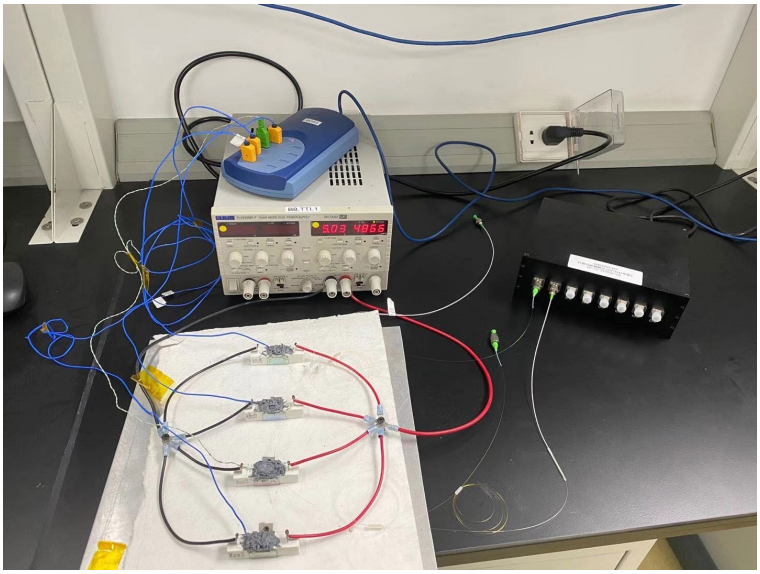

Figure 3.9. Photo of experimental setup of temperature monitoring prototype V2.0. The black box is the FBG interrogator product. Such high speed FBG interrogator is very useful for other high-frequency target parameters as well (e.g. vibrations, rotating speed).

Results & Discussion

Thermal maps shown in Figure 3.10 were plotted by Matlab using temperature data from the FBG interrogator [169]. These data represent static temperature readings of four power resistors when $V_{DC} = 20\ volts$ was kept on for 20 minutes in a natural air-cooling environment. The experimental setup (Figure 1) was used under constant environmental temperature of 23 °C. The hot-spots

thermal map measured by FBG sensors (Figure 3.10-a) was compared with the thermal map measured by thermocouples (Figure 3.10-b). The four temperatures measured by FBG sensors were 3.2% (3.5 ± 1.35) higher than these measured by thermocouples. The thermal maps showed four heat points with temperatures ranging from 35 to 202 °C. This temperature range has completely covered the temperature standard for four insulation classes (A, B, F and H) of electric machines defined by NEMA [122]. These experimental results illustrated that the polyimide-coated FBG sensors are applicable for EM thermal monitoring with required measurement accuracy.

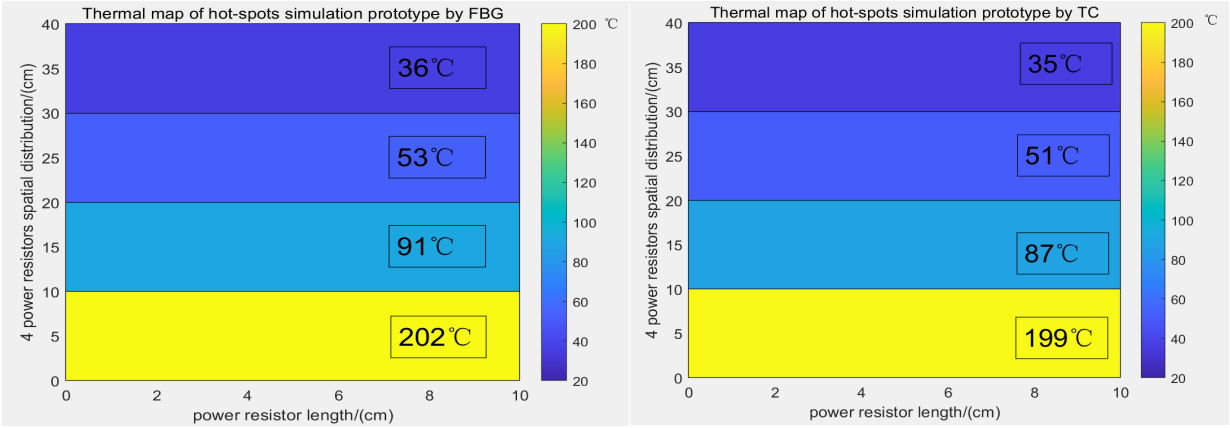

Figure 3.10. Thermal maps of equivalent hot-spots prototype measured by a) FBG sensors and b) thermocouples

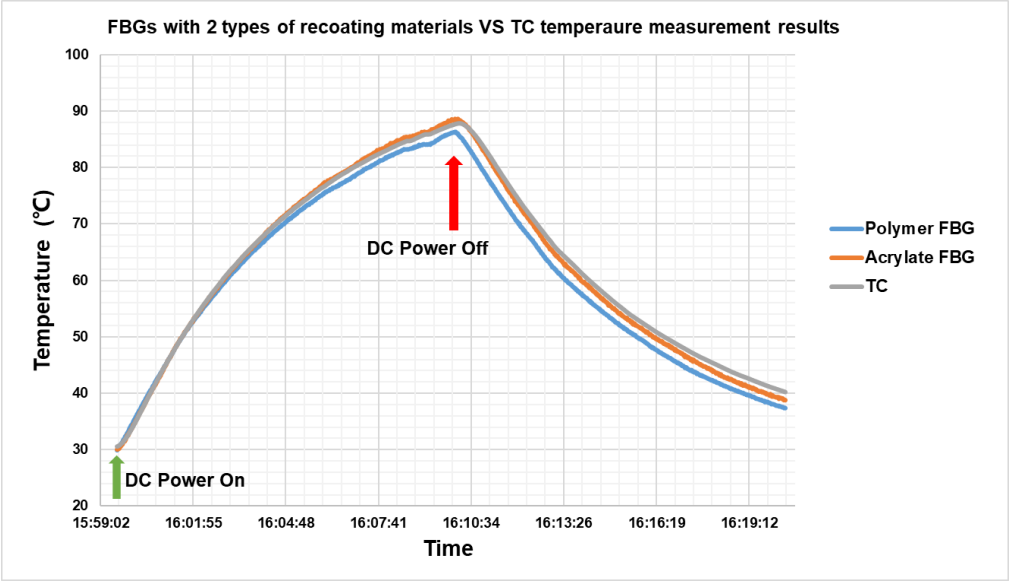

Figure 3.11. Temperature monitoring window of one power resistor for a certain period (about 20 minutes). This monitoring system record both heating and cooling duration by switching the DC supply. To be noticed, unlike the previous version measurement, $V_{DC} = 20\ volts$ was fixed when DC supply is on during the measurement, which mimicked the actual EM start-stage thermal distribution along timeline. Two types of FBG sensors and one thermocouple were used, high correlation among these three types of sensors with error within 5 ℃ was shown, thus, the temperature reading difference can be attributed to random statistic errors, which is acceptable.

Both polyimide-coated and acrylate-coated FBGs were employed for the temperature measurement comparison shown in Figure 3.11.

3.3 FBG with Power resistors: summary of the findings

In this chapter, from FBG temperature sensing prototypes V1.0 to V2.0, we have successfully built and validated the working principle of FBG thermal sensor (V1.0), developed automatic real-time Matlab temperature demodulation program (V1.1) cooperated with Keysight optical devices, and constructed a 1kHz high speed FBG thermal sensing system with big data storage for long-period monitoring (V2.0). The FBG thermal sensor system V2.0 will be employed for further thermal experiments in our research. In addition, however, the OUT of thermal experiments in this chapter was limited to ceramic power resistors. FBG sensor system implementation in critical EM component - copper windings, will be conducted for next stage sensor prototype construction as we planned.

4 Thermal Experiments: FBG on copper windings

In this chapter, the thermal experiments of FBG sensor on copper windings will be conducted since the proof-of-concept experiments were validated in last chapter. Several versions of copper winding thermal experiments will be presented as well as the thermal modelling results of corresponding copper windings. The comparison and analysis of copper winding thermal experiments would verify the feasibility of FBG for EM thermal monitoring further. Additionally, the very initial ML-based copper winding temperature prediction model will be designed, built and analyzed in this chapter. Support vector regression (SVR) algorithm was chosen as the base algorithm for ML modelling.

4.1 3-point FBGs on copper winding

Experimental design and setup

The thermal experiment setup of 3-point FBG is shown in the Figure 4.1. The whole thermal test bench consists of FBG sensor system, DC power supply (KORAD KA3305P) and target thermal object (self-manufactured copper winding). Three points of sensors were chosen at typically vulnerable positions: the centre of one-side end-winding (FBG 1) and two corners of the other side end-winding (FBG 2 & 3).

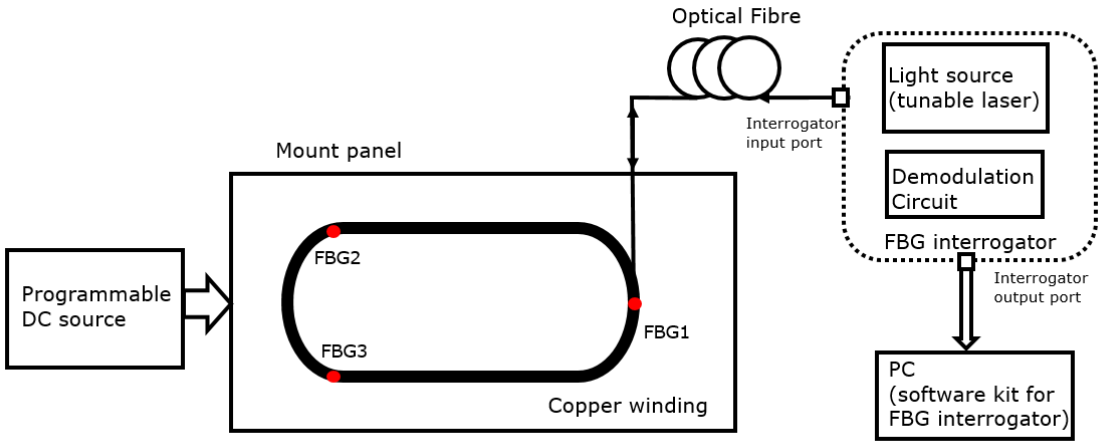

Figure 4.1. Schematic of copper winding thermal experiment setup with 3-points FBG sensors placed.

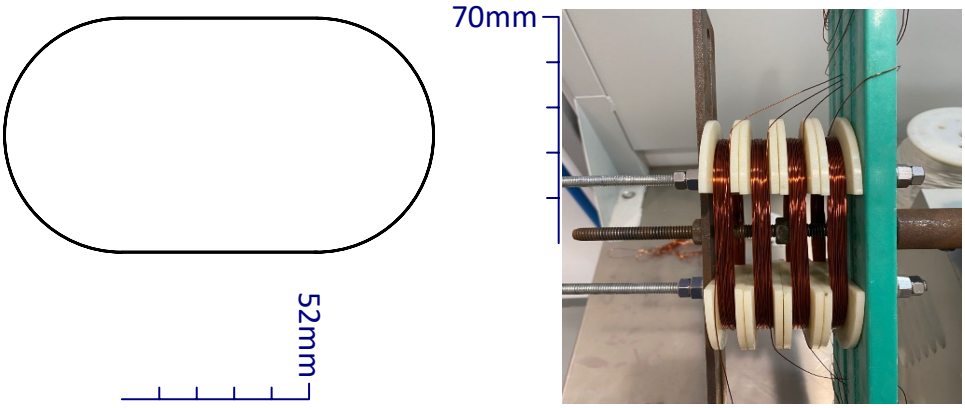

Figure 4.2. Dimension scheme of copper winding (left) and photo of winding machine manufacturing process (right)

Table 4.1 Parameters used in copper winding thermal simulation.

Values of parameters used for Siemens MagNet and ThermoNet simulation model construction	
Diameter of cooper wire	0.46mm
Cross-section area of single copper wire	0.16619 mm^2
Number of winding turns	50
Total length of each winding	16.195m
Electrical resistivity of copper	$0.0172\Omega \cdot mm^2 \cdot m^{-1}$
Actual electrical resistance of one manufactured copper winding	1.67617 Ω
Cross-section area of single modelling copper wire	0.16619 mm^2
Theoretical overall drawing area of copper winding	23.7414 mm^2
Copper space factor	0.35
Radius of one drawing copper winding model	2.749 mm
Simulated electrical resistance of one copper winding model	1.695 Ω
Electric conductivity of copper	5.77e7 Siemens· m^{-1}
Thermal conductivity of copper	401 W/$(m \cdot K)$ (Constant during thermal simulation)

The physical dimensions of copper winding used in experiment and manufacturing process are shown in Figure 4.2. The actual parameters are shown, diameter of cooper wire (**D_wire** =0.46mm),

cross-section area of single copper wire (**s_wire**= 0.16619 mm^2), and number of turns (**N** = 50 turns). The length of one winding (**L** = 219.9mm * 50 turns = 16.195m) while electrical resistivity of copper is assumed as **ρ**=0.0172$\Omega \cdot mm^2 \cdot m^{-1}$. Therefore, the actual electrical resistance of one manufactured copper winding can be calculated as **R_actual**= **ρL/s**= 1.67617 Ω.

Simulation model construction

The simulation model (Figure 4.3) is built based on the actual copper winding we made shown in Figure 4.2. The modelling process is shown: the overall copper winding (Strand coil type) geometry should be drew with some assumptions: Assume copper space factor is 0.35 (other space default as natural air) and we know cross-section area of single modelling copper wire (**s_strand**=**s_wire** = 0.16619 mm^2), **N** = 50 turns. Thus, the theoretical overall drawing area **S_draw** =(s_strand * N)/copper space factor = 23.7414 mm^2, then we got **r_draw** = 2.749 mm. Other geometric parameters were set as the same values with those of the actual copper winding. Finally, comparing electric resistances of model **R_sim** = 1.695 Ω while **R_actual** = 1.67617 Ω. Therefore, both geometry & electric resistance of winding model are comparable to those of actual copper coil, we can use this model for thermal simulation.

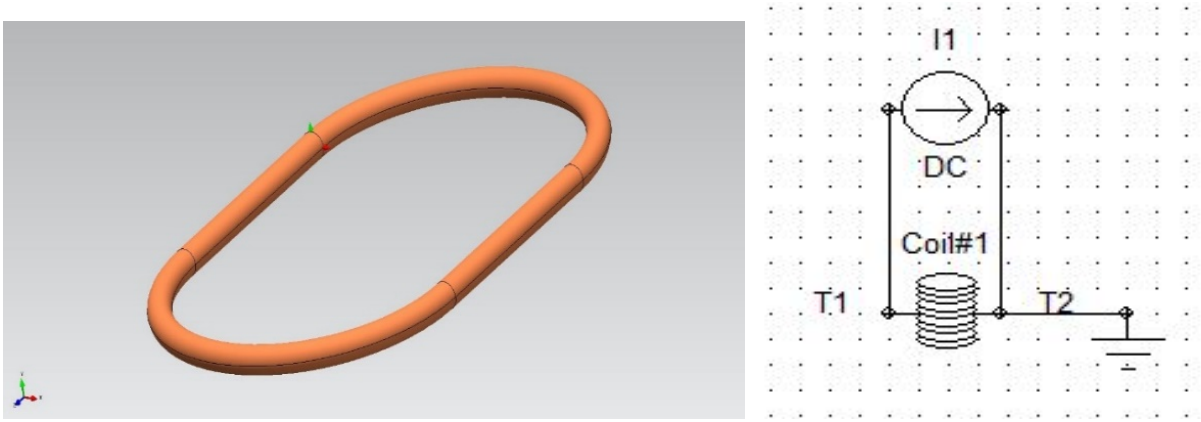

Figure 4.3. Scheme of copper winding model built by Siemens Magnet and ThermoNet (left), the equivalent circuit for winding thermal simulation (right). Copper material settings of copper modelling followed the default values of 'Copper: 5.77e7 Siemens/meter', where thermal environment was set as "natural air environment", convection body type as "Horizontal cylinder" and no extra forced convection was introduced.

Results and discussion

The S2, S3 and S9 EM duty-cycle modes [166] were applied experimentally for the validation of FBG temperature sensors used for copper windings. The ambient was always under natural-air cooling environment.

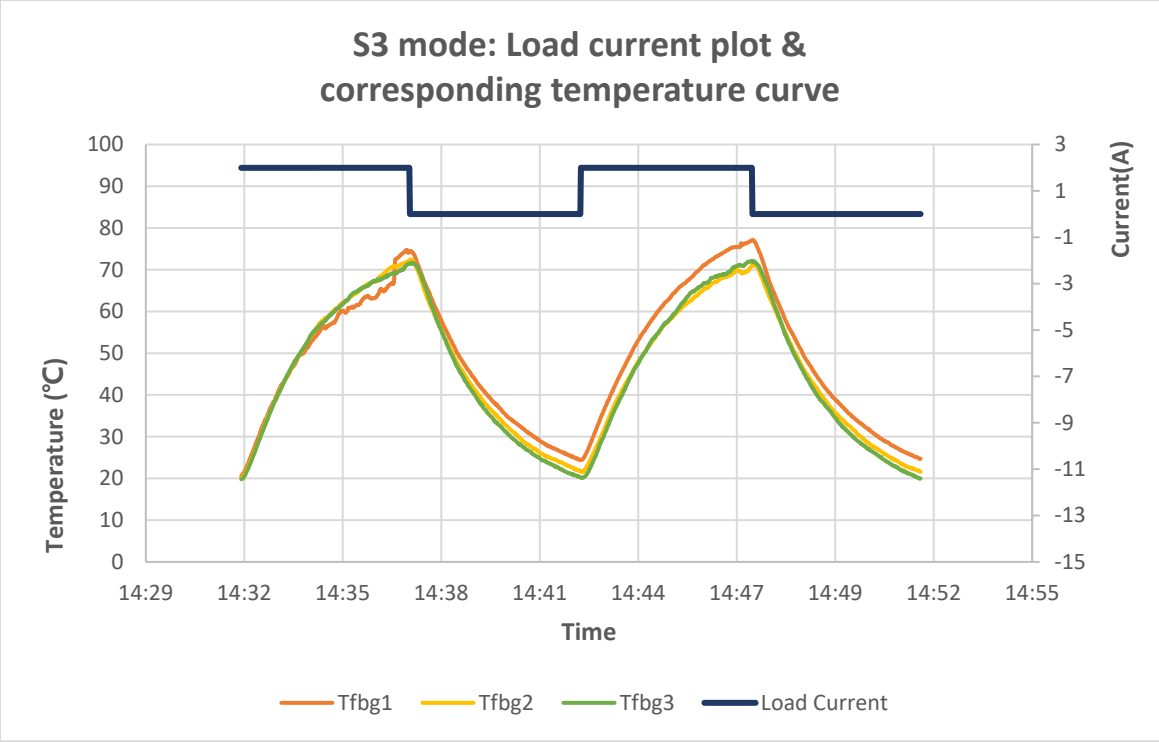

Figure 4.4. Temperatures at three positions of copper winding with S3 mode applied. S3 load current pattern is shown in the top line. The unstable temperature fluctuation (± 8℃) of FBG1 between 14:35-14.37 should be led by the unexpected expansion of thermal paste, it was a random error of measurement and the error range was acceptable for this copper winding thermal monitoring task.

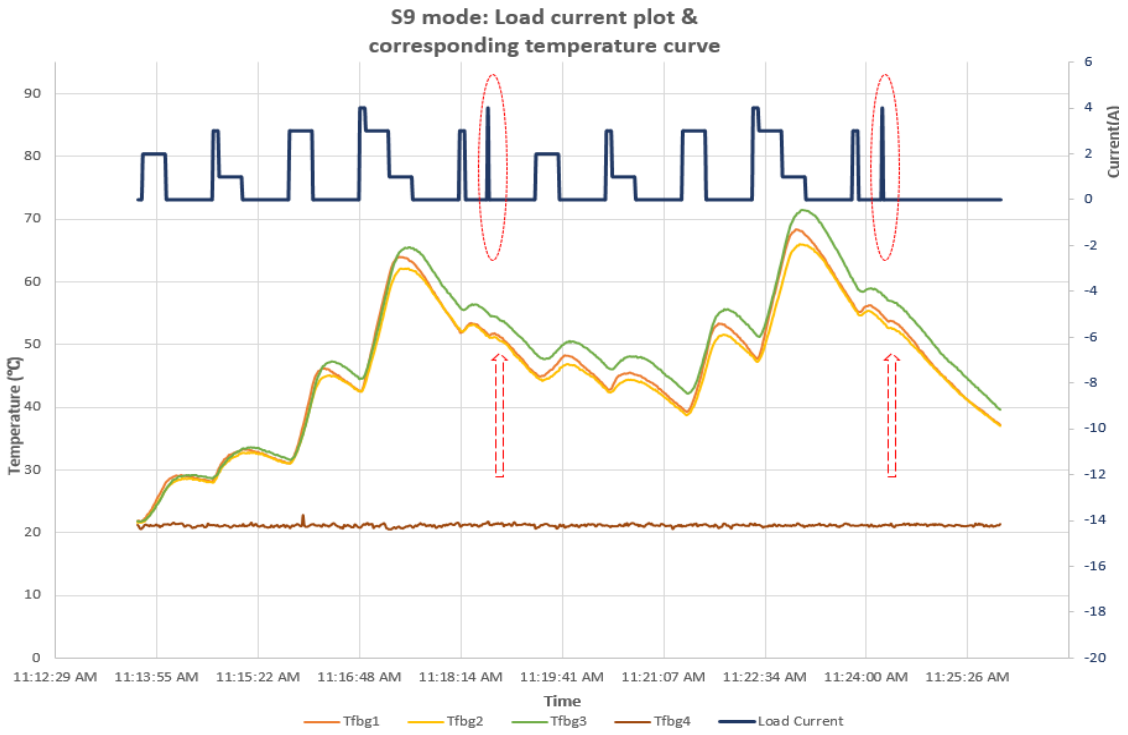

Figure 4.5. Temperatures at three positions of copper winding with S9 mode applied. S9 load current pattern is shown in the top line. In addition, FBG4 was employed as reference sensor for ambient temperature monitoring. It can be observed that in S9 mode test, rather than periodic and long-term load, random and pulsed load current supplies were applied. Short-pulsed load current (1 second) were applied to the copper winding and the plot indicated temperature of copper winding was affected by the pulsed current. FBG sensors are able to capture those 'thermal ripple' with sufficient sensing response.

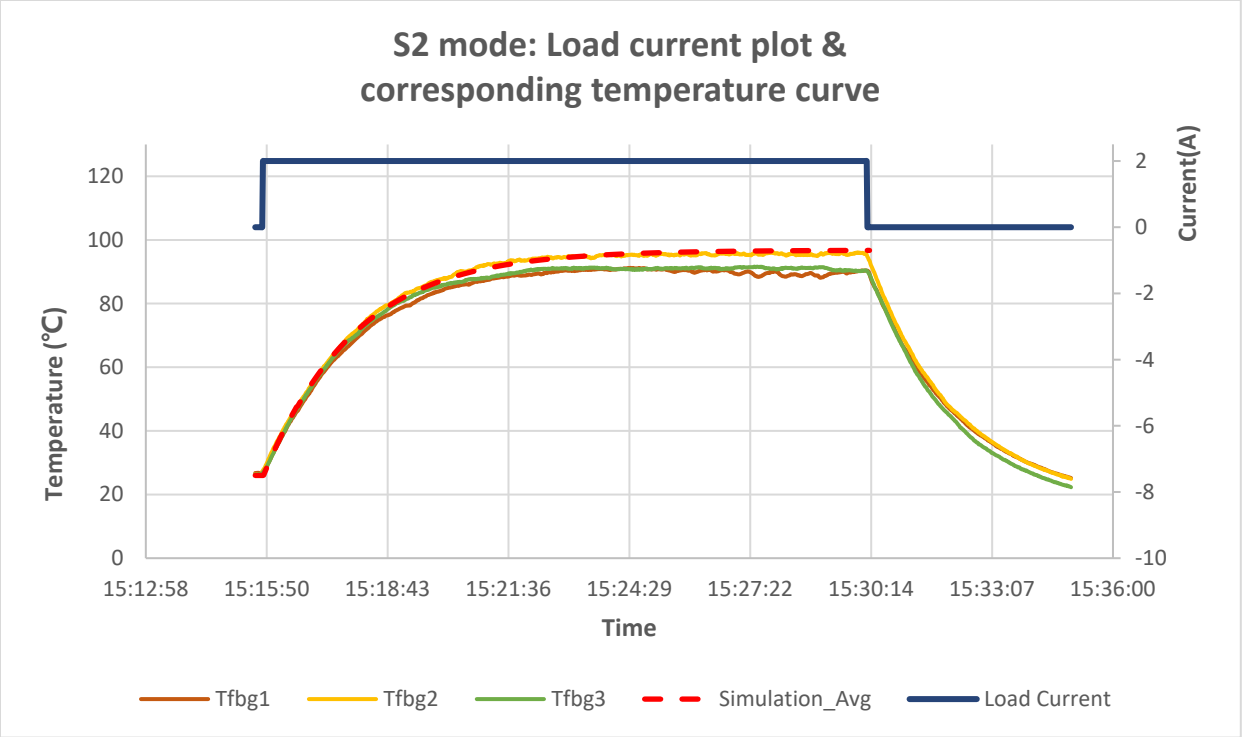

Figure 4.6. Temperatures at three positions of copper winding with S2 mode applied. S2 load current pattern is shown in the top line. The average temperature curve generated by thermal model is plotted in dash red line.

The simulation results (dash line in *Figure 4.6)* that the temperature distribution over the copper winding is relatively uniform, therefore, only the 'average temperature curve' is chosen to compare with the experimental results measured by FBGs.

We can see that, there are temperature difference at different position of the copper windings (within 5 °C) measured by FBG sensors, such temperature difference is larger than the simulation results, it may be caused by several practical engineering reasons:

1. Conductivity of the thermal paste is not uniform.

2. Random error led by FBG sensor implementation difference.
3. Expansion and Contraction of copper winding will apply extra strain to the FBG, such strain will also lead to measuring error of FBG temperature sensor (i.e. strain-thermal cross-effect of FBG).

4.2 8-point FBGs on copper winding

Experimental design and setup

The thermal experiment setup of 8-point FBG is shown in the Figure 4.7. The whole thermal test bench consists of FBG sensor system, DC power supply (KORAD KA3305P) and target thermal object (self-manufactured copper winding). Eight points of FBG sensors (FBG1~8) were uniformly distributed within the copper winding for a more comprehensive thermal mapping of copper winding using FBG sensors.

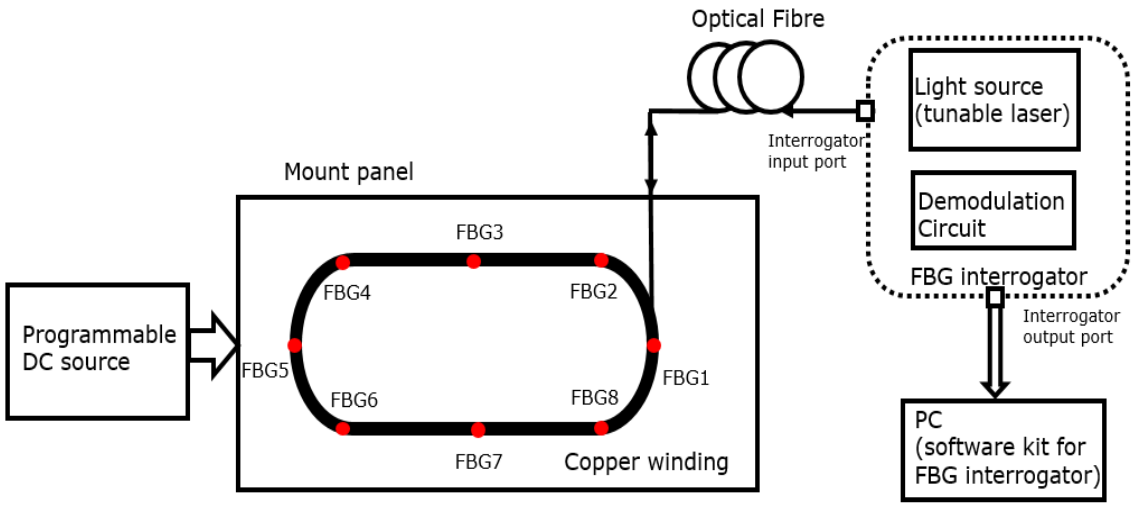

Figure 4.7. Schematic of copper winding thermal experiment setup with 8-points FBG sensors placed.

Results and discussion

Since the regular periodic EM duty load modes (S2 & S3) have been experimentally conducted in previous section, random load mode S9 will be focused on this 8-point FBG sensor setup thermal experiment with plots shown in Figure 4.8.

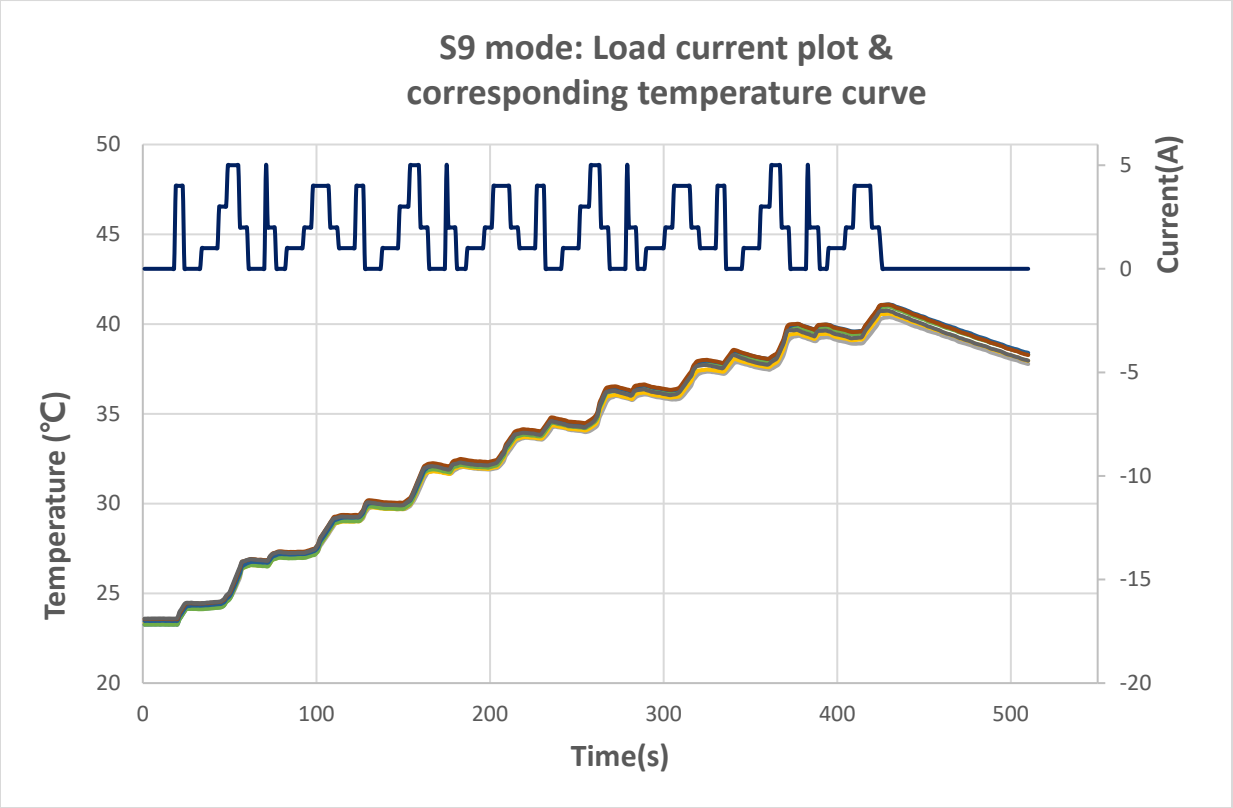

Figure 4.8. Temperatures at eight positions of copper winding with S9 mode applied. S9 load current pattern is shown in the top line. 8-FBGs are uniformly distributed at eight positions along the axial direction of copper winding as shown in the experimental setup scheme. The temperature difference among these positions is not obvious as shown in the temperature curves measured by FBG sensors.

Combing the temperature experiments results from both 3-point and 8-point test benches, we found that the temperature difference along axial direction of copper winding is not large. This may led by the thermal characteristics of copper: it has a great thermal conductivity of 401 $\mathrm{W}m^{-1}K^{-1}$. This property causes uniform temperature distribution of copper winding along copper winding. Additionally, the natural-air ambient also leads to a non-gradient temperature distribution of winding. To investigate the FBG thermal sensor for copper winding application, we should focus on the radial direction of copper winding rather than only axial and also consider to introduce the forced cooling system. An FBG sensing array should be implemented and validated to achieve comprehensive thermal monitoring of copper windings.

4.3 Polyimide-coated FBGs for EM copper winding thermal monitoring

4.3.1 Study Design

On completion of FBG thermal monitoring on power-resistor panel and copper winding in 2-D plane, a further experiment using copper coils as thermal targets was performed. Such coil resembles the bending conditions on real EM windings. The purpose of this experiment was to assess the feasibility of FBG sensor system for temperature monitoring when attached to EM coils. The configuration of one string of the Polyimide-coated multi-FBG is shown in Figure 4.9, which contains 8 serially ordered Bragg gratings of FBG sensors. Three such multi-FBG strings, coiled and buried in the middle of an EM copper windings connected to a DC voltage supply as shown in Figure 4.7, and the WDM technique of FBG Bragg wavelengths were implemented for the thermal monitoring of EM windings. Two thermal maps were generated- the axial thermal map of winding is shown in Figure 4.10 on the x-z plane while radial thermal map on the y-z plane.

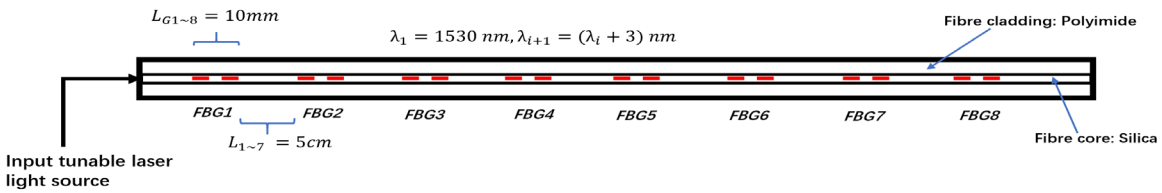

Figure 4.9. Structure of Polyimide-coated multi-FBG string. The length of grating area and the distance between gratings were labelled.

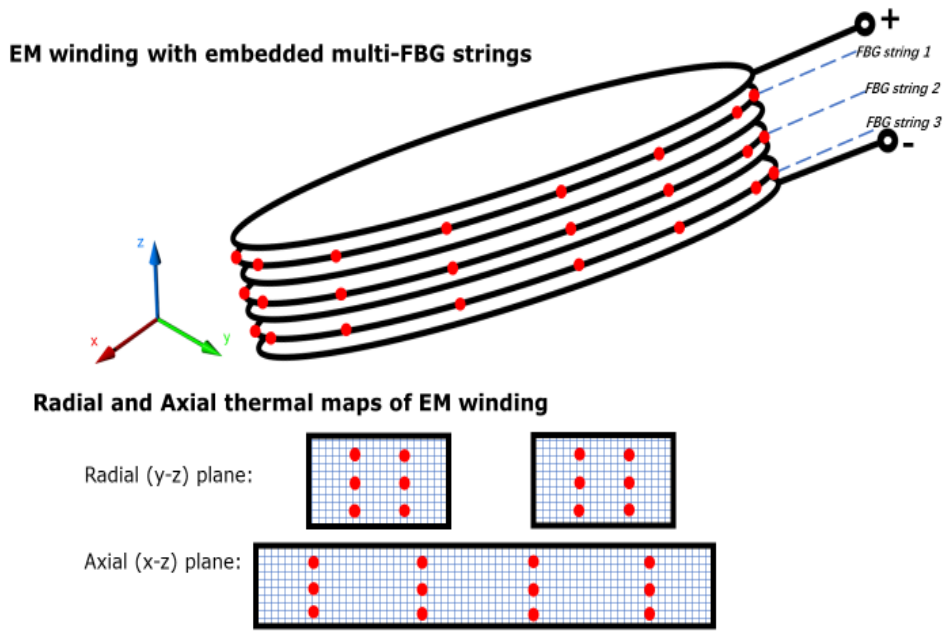

Figure 4.10. Schematic of three multi-FBG strings embedded together with an EM windings.

The thermal experiments will be conducted to check the thermal mapping for copper windings once the experimental test bench completed based on the study design above.

4.3.2 Results & Discussion

For thermal mapping, sensors (FBGs) were attached to the real copper coils, as shown in Figure 4.10. The hot spots shown in Figure 4.11-a) (radial thermal maps) and Figure 4.11-b) (axial thermal maps), were located with a spatial resolution of 6 cm matching the FBG inter-grating distance shown in Figure 4.9. The locations of these hot-spots indicated that the central and end-winding positions within the EM copper coils are prone to the overheating problems. Spatial resolution can be improved by either using denser spaced multi-FBG sensors or optimized locations of multi-FBG sensors based on mathematical modeling.

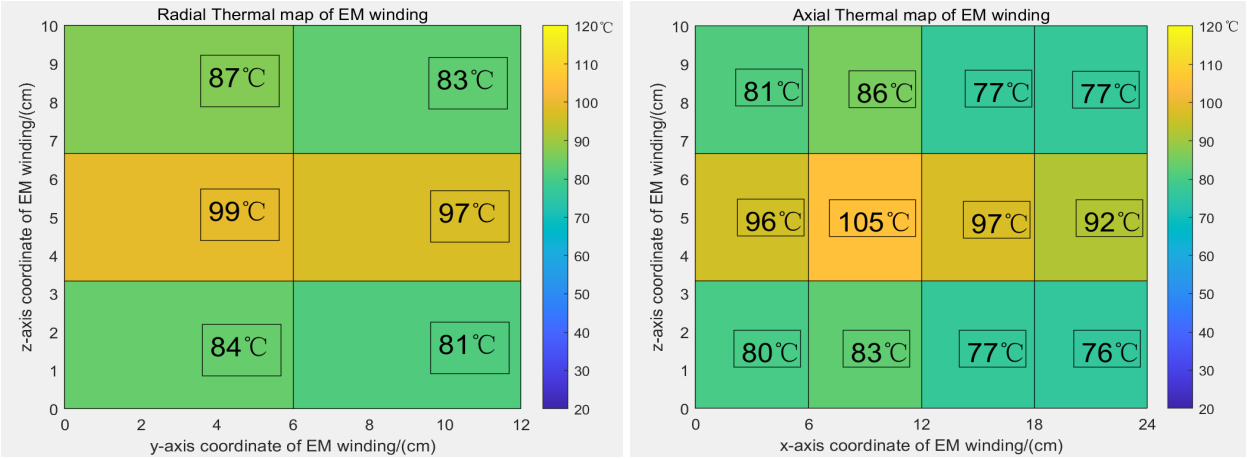

Figure 4.11. a) Radial thermal map (left panel), and b) axial thermal maps (right panel) of EM windings with multi-FBG string embedded prototype.

Polyimide-coated multi-grating FBG sensor strings were used to construct a prototype for efficient measurement and real-time construction of 2-D thermal maps of electric machine copper windings, in both radial and axial directions [107]. The FBG thermal sensing system prototype based on tunable laser technology demonstrated advantages for thermal mapping of EM coils: broad temperature detection range (20-200°C), adequate spatial resolution (6 cm) and fast wavelength sweeping frequency (up to 1kHz). Simultaneous thermal maps can be used for real-time

monitoring of the distribution and spatial localisation of thermal hot spots within the EM windings. These hot-spot locations are the primary locations for the degradation of winding insulation, a principal cause of the lifespan reduction of the EMs. The design concept of FBG sensor system presented can be used to track thermally vulnerable points, select safe operational regimes, and optimize EM maintenance.

4.4 FBGs on copper windings with temperature prediction models

Till now, we have developed and validated the FBG temperature sensor prototypes for EM copper windings in lab-version. However, to solve one of our focused research questions, we shall introduce ML algorithms to optimize (i.e. minimize) the sensor number without the loss of thermal monitoring resolutions.

Machine learning algorithms are far-ranging employed for electric machine health monitoring and fault diagnosis [170]. Support vector machine for regression (SVR) is one of popular machine learning algorithms for target value prediction model construction in electrical systems [171]. A well-trained SVR statistical model can be used to speculate and predict the temperature on specific location of EM winding, such physical location would no longer need to be implemented with in-situ temperature sensor, therefore, and number of sensors can be reduced with no accurate temperature data missing. It is an efficient solution for optimizing the sensor number of EM monitoring as long as the SVR prediction model demonstrates a reliable performance.

An SVR model for EM copper winding temperature prediction, with Polyimide-coated FBG string sensor system [107] for comprehensive thermal features data collection, is reported in this section. 11 features categorized into three sections were chosen to be the input features of SVR model

while the target output is temperature value at one specific position of EM copper winding. Finally, we can used seven in-situ temperature sensors to obtained eight temperature readings of EM winding, and this ratio will be optimized in future.

4.4.1 Example of ML temperature prediction model

SVR is a type of supervised machine learning algorithm for solving regression problem evolved from Support Vector Machine (SVM) algorithm [172]. It is a statistical modelling method suitable for small sample size engineering case, it can be employed for classification (SVC) or regression (SVR) problem depending on the specific application scenarios: our propose is to continuously predict the temperature at specific position on copper winding with known EM operation load pattern, therefore, SVR model is chosen for EM copper winding temperature prediction. Generally, SVR algorithm has some outstanding advantages when the number of features (i.e. input variables of model) and sample size is not massive, including: strong generalization ability, high prediction accuracy, relatively simple statistical math model and diverse choices of kernel functions.

SVR modelling task is to seek a function $f(x)$ that can predict the desired information with known features provided. The mathematical function of predicted values y_i' is shown:

$$y_i' = f(x_i) = \boldsymbol{\omega} \cdot \boldsymbol{\varphi}(x_i) + \boldsymbol{b} \tag{4.1}$$

Assuming that an experimental data set $(x_i,\ y_i)$ with sample size N are collected through EM winding thermal experiments, where x_i are the input features and y_i is the target output physical quantity. The aim of SVR prediction model is to solve a function $f(x)$ that enables predicted target output y_i' matched with the actual values of target output y_i, as close as possible. The SVR model construction is by using the given training data set $(x_i,\ y_i)$ to solve the optimal values of weight vector $\boldsymbol{\omega}$ and $\boldsymbol{b}$ bias terms, so that $f(x)$ can output target values with only input features x_i

provided to the trained SVR model. The construction of our ML models was based on "Scikit-Learn" open access Python machine leaning development environment [173].

4.4.2 Experimental setup

An experimental FBG sensor prototype of EM copper winding for thermal measurement was built based on the test bench design shown in Figure 4.12. A Polyimide-coated multi-FBG string [43] with WDM technology (eight sensor points in total) was placed and spatially uniform distributed on the EM winding (100 turns, diameter of enamelled copper wire: 0.9 mm), which was identical to the 8-point FBG sensor setup (Figure 4.7). However, for the ML model construction data collection, short-circuit tests with different programmed load patterns were applied to the EM winding, meanwhile, by using an FBG interrogator from Arcopt Inc [169], wavelength shift $\Delta\lambda_B$ of FBG 1~8 were collected with sample rate 1 Hz. All thermal experiments were conducted in a natural air cooling environment with multi-sensors data recorded continuously at 1Hz sampling rate.

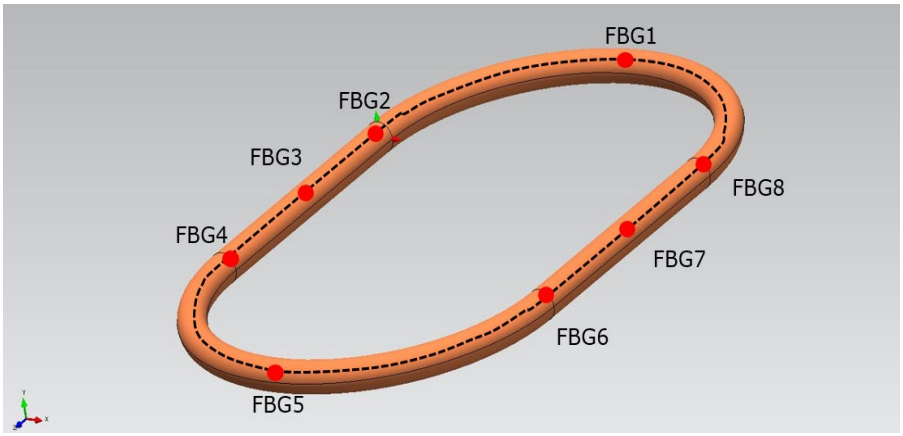

a)

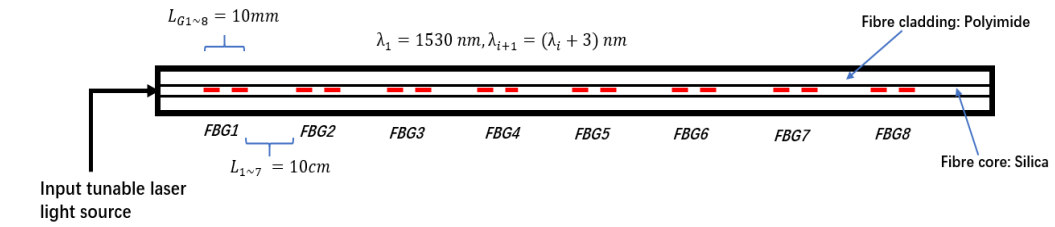

b)

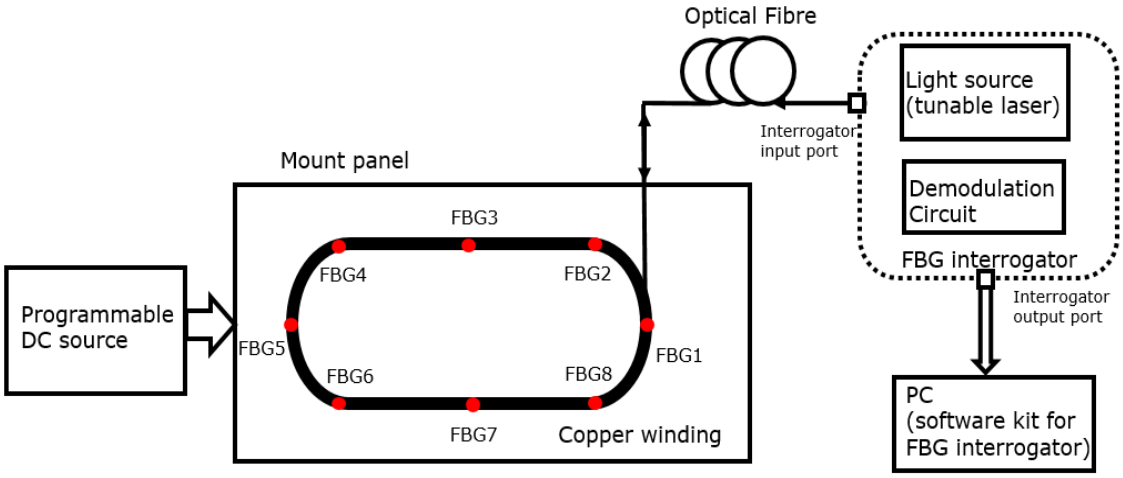

c)

Figure 4.12. Schematics of EM winding thermal experiment setup: a) 3D model view (by Siemens MagNet software) of EM copper winding with multi-FBG string sensors placed b) Structure of Polyimide-coated multi-FBG string used for EM copper winding temperature measurement. c) Scheme of thermal test bench of EM copper winding.

The test bench for ML temperature modelling was same as "8-point FBGs" experimental setup shown in Figure 4.7. The thermal experiments with different electrical load patterns will be

conducted using this test bench for raw data collection. The ML model design process and temperature prediction results will be presented in the following sections.

4.4.3 Design process of SVR model for EM winding temperature prediction

Once the thermal experiment prototype was set up, the thermal experiments will be conducted with all input features and target output data recorded. The input features were categorized into three sections [174]: sensor measurement, electrical and environmental variables. The sensor measurement variables consists of seven real-time Bragg central wavelengths (CW) of FBG 1~7. These optic spectral parameters are chosen as inputs of SVR model because the in-situ temperature variation $\boldsymbol{\Delta T}$ at different positions of EM winding are strongly correlated with Bragg central wavelength shift $\boldsymbol{\Delta \lambda_B}$ as discussed previously, the SVR model should be capable of learning the mathematical expression between the CWs and the temperatures. In terms of the electrical variables, load current $\boldsymbol{I}$, load voltage $\boldsymbol{V}$ and heat power $\boldsymbol{W}$ were recorded. For environmental variable, since the present EM winding thermal prototype is under natural-air cooling environment, only the ambient temperature $\boldsymbol{T_{ambient}}$ was recorded. All data was collected with sample rate at 1 Hz, and target output $\boldsymbol{T}$ is the temperature at position_8 of EM winding.

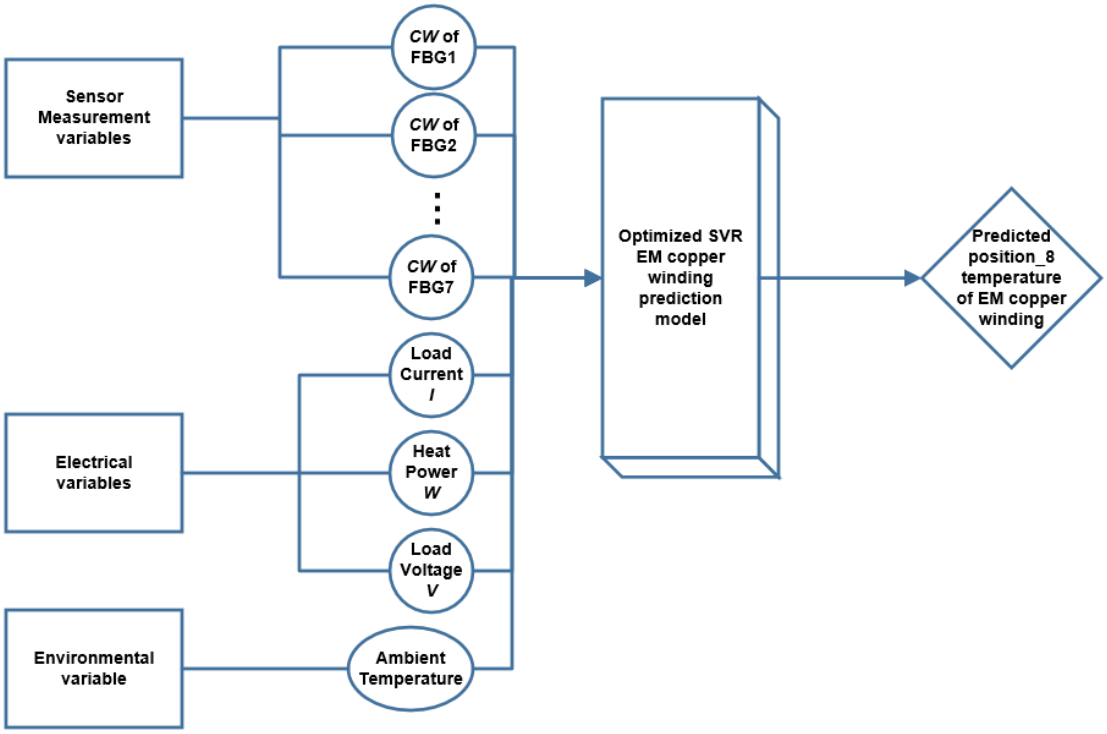

Figure 4.13. Structure of SVR copper winding temperature predict model, the SVR input variables $x_i = [CW1, CW2 \dots CW7, I, W, V, T_{ambient}]_i$ *and output target* $y_i = [T]_i$ *where* $i = N$*, which is the sample size of dataset.*

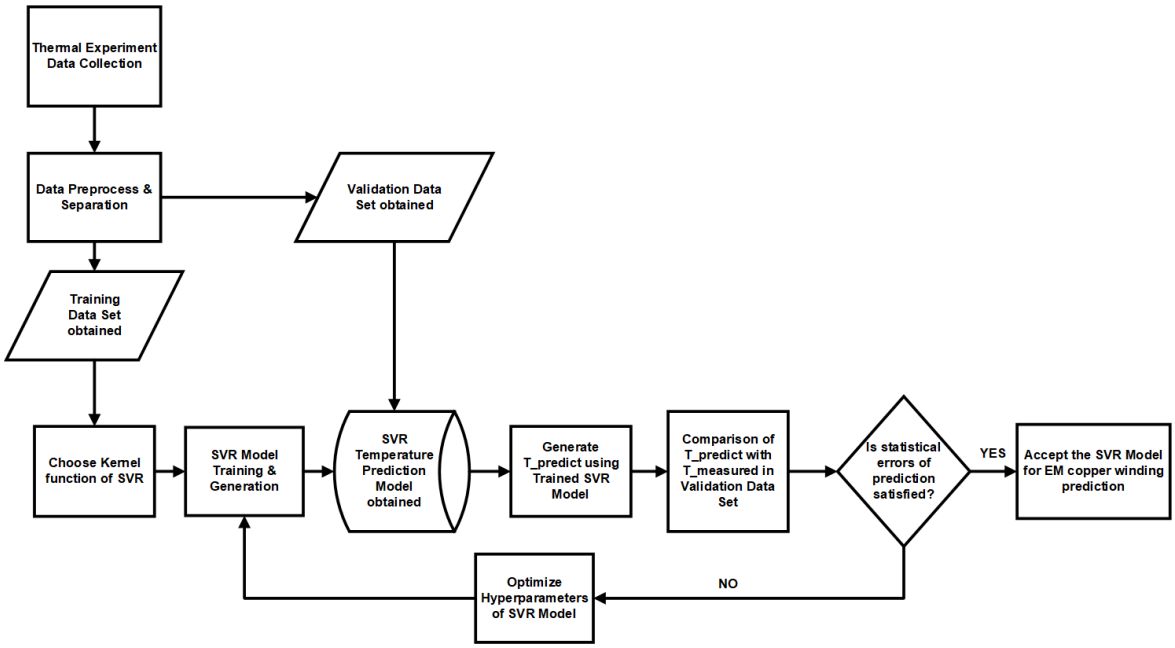

Figure 4.14. Design and optimization process of SVR copper winding temperature prediction model.

Once the structure of SVR model was confirmed as shown in Figure 4.13, the overall design and optimization process of SVR winding temperature prediction model should be considered. Overall process to generate a well-performed SVR EM winding temperature prediction model is shown in Figure 4.14: firstly, all experimental data including input features and target outputs were collected. Then several groups of measured data were separated into training datasets and validation datasets. Both types of datasets need to be pre-processed: normalization of input features was necessary for the sake of SVR model performance [175] by using function: $x_i^* = (x_i - x_i^{min}/x_i^{max} - x_i^{min})$, because the input features are quantities with different dimensions. Training dataset was used to generate the SVR model while the validation dataset is to check the prediction performance of SVR model, K-fold cross validation method was also applied during the SVR model training step, the training step will be repeated until the SVR model with suitable hyperparameters can provide

satisfied prediction results. In this paper, four statistical error indexes were calculated to evaluate the prediction performance of the model [176] by comparing the values of experimental measured values $\boldsymbol{T_{mesured}}$ and $\boldsymbol{T_{predict}}$:

$$\text{Mean absolute error (MAE): } e_{MAE} = \frac{1}{N}\sum_{i=1}^{N}\left|T^i_{measured} - T^i_{predict}\right| \tag{4.2}$$

$$\text{Mean absolute percentage error (MAPE): } e_{MAPE} = \frac{100\%}{N}\sum_{i=1}^{N}\left|\frac{T^i_{measured} - T^i_{predict}}{T^i_{measured}}\right| \tag{4.3}$$

$$\text{Root mean squared error (RMSE): } e_{RMSE} = \sqrt{\frac{1}{N}\sum_{i=1}^{N}\left(T^i_{measured} - T^i_{predict}\right)^2} \tag{4.4}$$

$$\text{Correlation coefficient } (R^2)\text{: } R^2 = 1 - \frac{\sum_{i=1}^{N}\left(T^i_{measured} - T^i_{predict}\right)^2}{\sum_{i=1}^{N}\left(T^i_{measured} - \bar{T}^i_{measured}\right)^2} \tag{4.5}$$

By checking the acceptability of above four regression performance indices (formula 4.2-4.5), we can decide the whether the trained ML model is good enough for the task of copper winding temperature prediction.

4.4.4 Results & Discussion

The plots of some input features in time domain for SVR model training are demonstrated in Figure 4.15, including the central Bragg wavelength of FBG1, load current $\boldsymbol{I}$, heat power $\boldsymbol{W}$ and ambient temperature, other input features shown in Figure 4.13 are not plotted for space-saving. In the experimental stage of EM winding short-circuit thermal tests, there were different electrical load

patterns (i.e. different time-varying load current modes applied to EM windings) designed and provided through programmable DC supply, with all variables data collected in groups of datasets. The electrical load pattern shown in Figure 4.15 used for SVR model training process is labelled as load pattern 1, the experimental validation datasets in same load (load pattern 1) and another load (load pattern 2) will be both applied to the SVR model to check the performance and generalization ability of the trained SVR model.

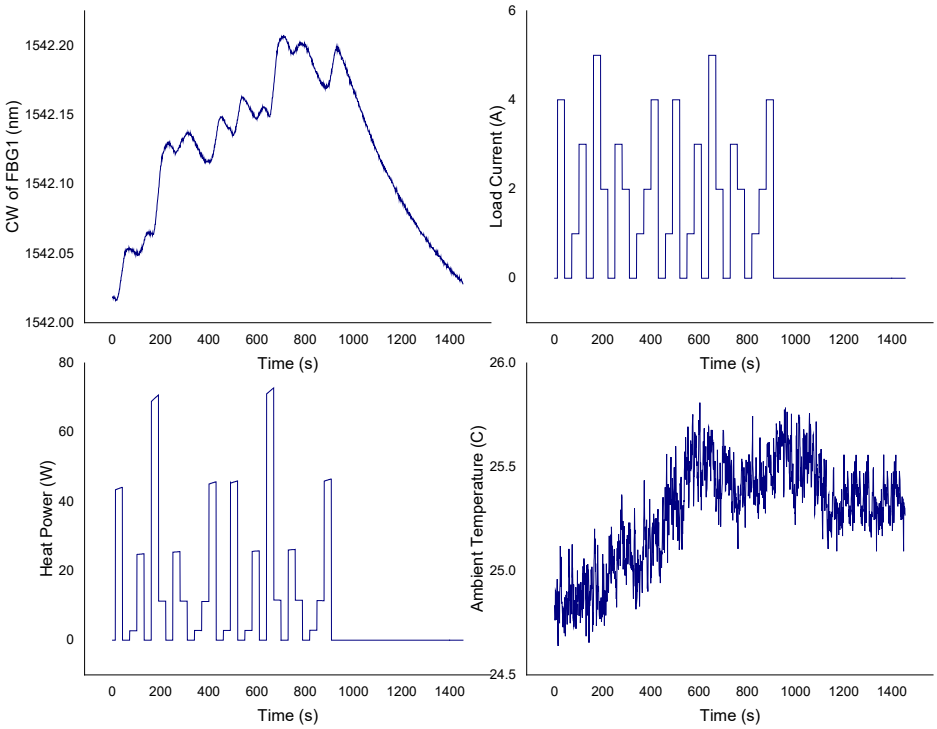

Figure 4.15. Sequential data plots of part of input variables for SVR EM winding temperature prediction model construction, the electrical load pattern shown in load current and heat power plots is labelled as load pattern 1.

The prediction results of temperature at position_8 on EM winding are shown in Figure 4.16. The electrical load pattern of training dataset is load pattern 1, therefore, the SVR model prediction performance was firstly validated using the same load pattern experimental dataset as shown in Figure 4.16).

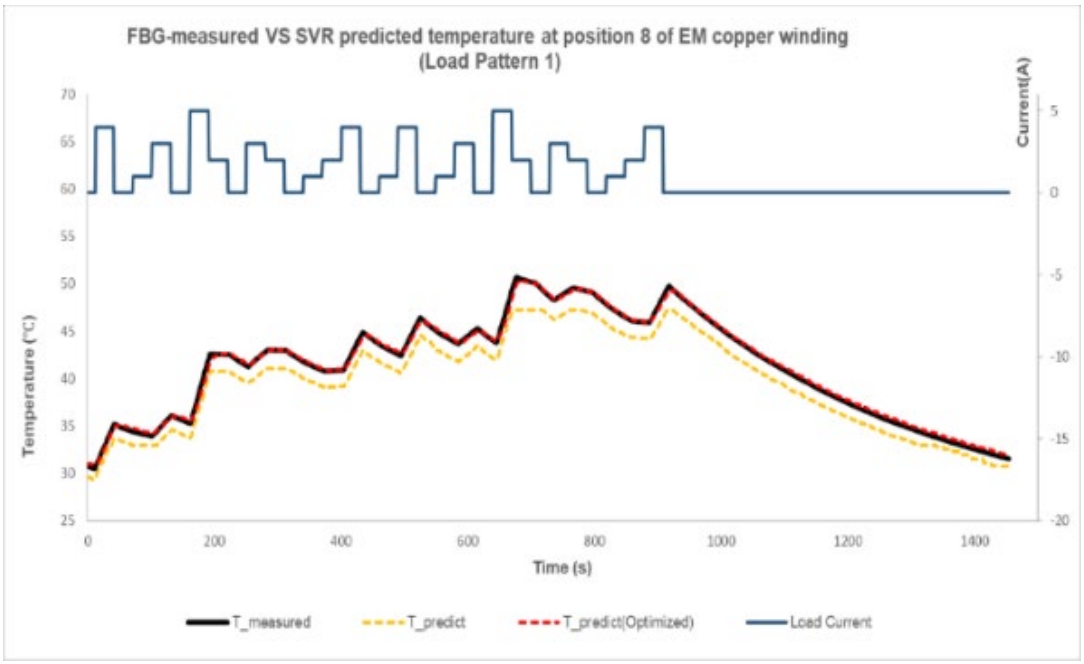
FBG-measured VS SVR predicted temperature at position 8 of EM copper winding
(Load Pattern 1)
Temperature (°C)
Current(A)
Time (s)
T_measured
T_predict
T_predict(Optimized)
Load Current

a)

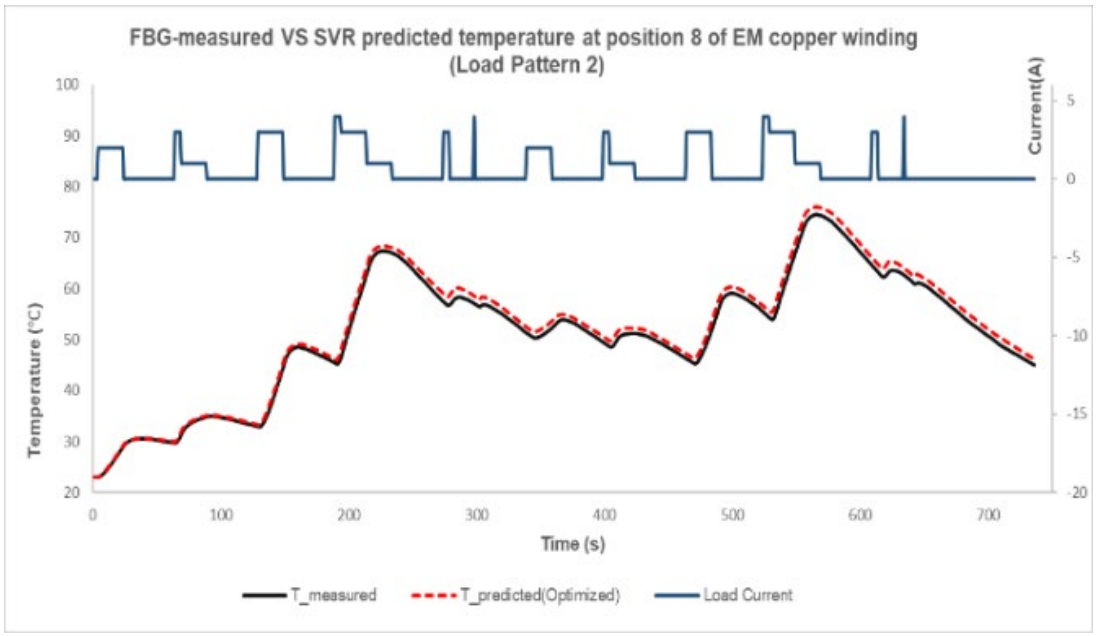
FBG-measured VS SVR predicted temperature at position 8 of EM copper winding
(Load Pattern 2)
Temperature (°C)
Current(A)
Time (s)
T_measured
T_predicted(Optimized)
Load Current

b)

Figure 4.16. Plots of SVR EM temperature prediction results. a) In load pattern 1, Experimental FBG-measured temperature $T\_measured$ *VS predicted temperature* $T\_predict$ *by the early-stage SVR prediction model, and predicted temperature* $T\_predict(optimal)$ *by the optimized SVR prediction model. b) In load pattern 2, Experimental FBG-measured temperature* $T\_measured$ *VS predicted temperature* $T\_predict(optimal)$ *by the optimized SVR prediction model.*

For the early-stage SVR prediction model, comparing prediction temperature results T_ predict with the FBG measured experimental temperatures T_ measured, four indexes are $e_{MAE} = 1.7258, e_{MAPE} = 4.12\%, e_{RMSE} = 1.7754, R^2 = 0.8928$. After applying the SVR model optimization steps, which represents using the machine learning process to choose the optimal hyperparameters of SVR model, including Kernel function type, Epsilon **ε**, Box constraint and Kernel scale, an optimized SVR model was obtained. Comparing prediction temperature results T_ predicted(optimised) with the FBG measured experimental temperatures T_ measured, new four indexes are $e_{MAE} = 0.2429, e_{MAPE} = 0.61\%, e_{RMSE} = 0.2987, R^2 = 0.997$. There is a significant improvement of prediction model performance. It can be concluded that the optimized SVR temperature prediction model can provide a well-performance for EM winding temperature prediction when the input electrical load pattern is same with that of the training dataset.

The SVR prediction performance for different electrical load pattern should be checked as well. A new electrical load pattern (load pattern 2) for SVR model performance test was generated and shown in Figure 4.16). In load pattern 2, comparing prediction temperature results T_ predicted(optimised) with the FBG measured experimental temperatures T_ measured, four statistical indexes are $e_{MAE} = 1.1209, e_{MAPE} = 2.08\%, e_{RMSE} = 1.2258, R^2 = 0.9896$. The

predicted performance are not as good as previous results when load pattern of training and validation dataset are same. However, such statistical analysis results still illustrates that the optimized SVR EM temperature prediction model has a relative strong generalization capability: for different patterns of input features, the model can still can provide relatively accurate target output temperature values.

4.5 FBG on copper windings: summary of the findings

To sum up, we designed, implemented and validated several versions of FBG thermal sensor prototypes for bare enameled copper windings. The number of effective FBG sensing points increased from 3-point, 8-point, then to final 24-point version for comprehensive thermal monitoring of copper windings using FBG sensors implemented within. Additionally, the thermal modelling of manufactured copper windings was conducted using Siemens MagNet & ThermoNet software environment, the simulation results demonstrated a strong agreement with the FBG temperature measurement results. Finally, an example of ML temperature prediction model was designed and constructed based on SVR algorithm. The trained model presented an accurate winding temperature prediction performance with multiple input feature data employed. Such achievement indicated the proper research direction of using FBG-ML combined method for EM copper winding temperature prediction. For next stage experimental validation of our sensor prototype, motorette will be investigated as the interim thermal object between bare copper windings and real operating electric machines.

5 Thermal Experiments: FBG with Motorette

In this chapter, the thermal experiments of FBG sensor on motorette will be conducted since the copper windings thermal experiments were validated in last chapter. Two versions of motorette thermal setups (natural-air cooling & forced water cooling) will be presented as well as the thermal modelling results of corresponding motorette. The verification and analysis of motorette thermal experiments are the important "intermediate state" between the copper winding prototypes and the future final EM thermal monitoring prototype. Additionally, based on the SVR copper winding temperature prediction model presented in last chapter, a new SVR model will be designed, built and analyzed for motorette FBG sensor prototype.

5.1 FBGs with motorette

5.1.1 Experimental design and setup

An experimental prototype of EM stator with copper windings for thermal measurements was built based on Figure 5.2. The target thermal object is a complete EM motorette (Figure 5.1) physical model: a 6-slot steel stator frame with three-phase copper windings embedded within all slots. In terms of the temperature sensor system, polyimide-coated FBG sensors with WDM technology (six sensing points in total) were placed and spatially uniform distributed among a one-slot radial plane of EM winding. A programmable DC power supply (KORAD KA3305P) is parallelly connected to three phases of EM windings: short-circuit thermal tests of EM windings with two different international standard load duty/cycles of electric machines were applied: S3 mode (periodic intermittent duty) is a sequential loading of identical cycles, each cycle is composed of a time with constant loading and a pause with customized duty factor while S9 mode consists of

random loading combination within the permissible operating range [166]. These two EM operating modes were chosen since they are typical for EM thermal tests: S3 can be used for demonstrating the thermal distribution of EM winding at a stable and constant load/speed while S9 can be used for that under a rapidly varying load/speed condition. Meanwhile, by using an FBG interrogator from Arcopt.Inc [169], wavelength shift $\Delta\lambda_B$ of FBG 1~6 were collected with sample rate at 1 Hz for real-time thermal monitoring of EM winding. The photo of completed test bench was shown in c)*d).*

Figure 5.3. In addition, for the forced water cooling thermal experiments, industrial water cooler machine S&A CW-3000 was employed.

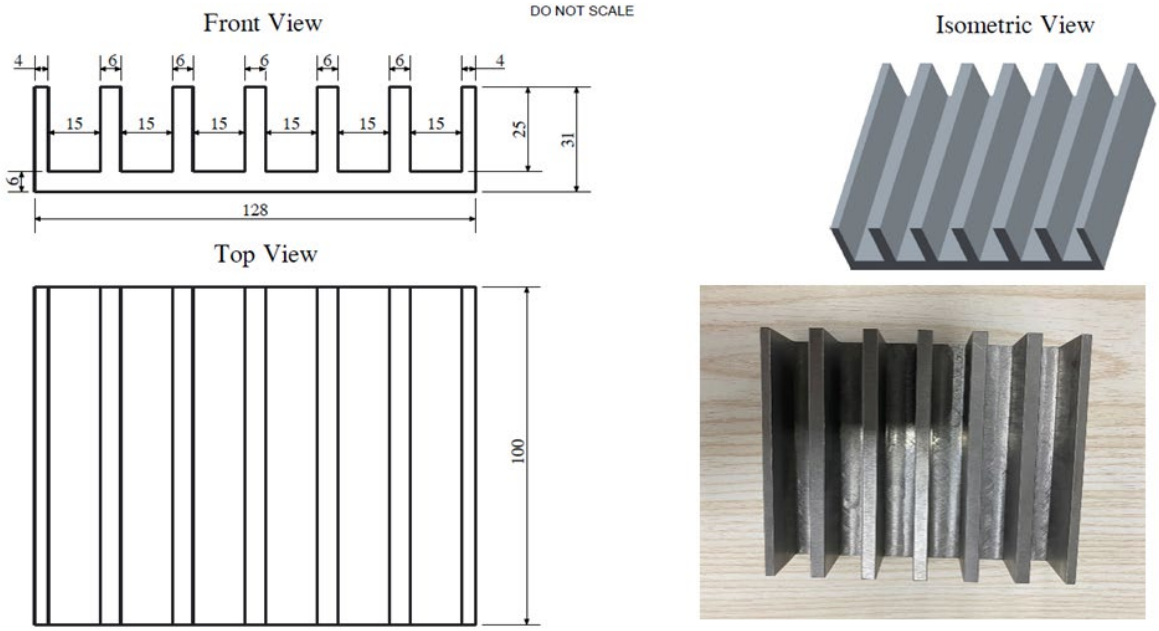

Figure 5.1. Layout drawing and photo of bare motorette frame employed for the thermal experiments. The unit shown in layout drawing is millimeter (mm).

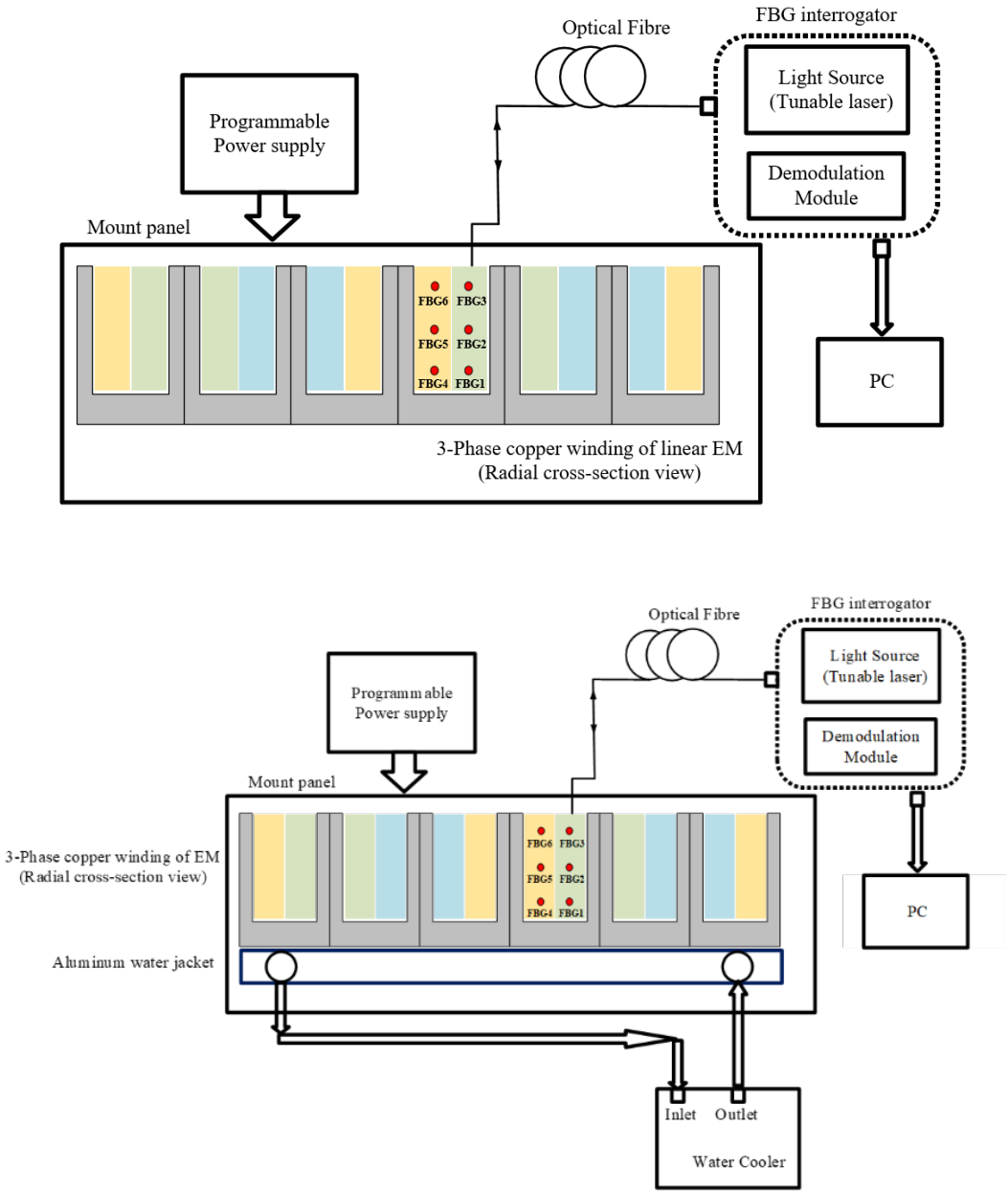

Figure 5.2. Scheme of motorette test rigs (natural air cooling & forced water cooling) with FBG sensors embedded, centralized three phase windings were labelled by three colors (yellow, blue, and green).

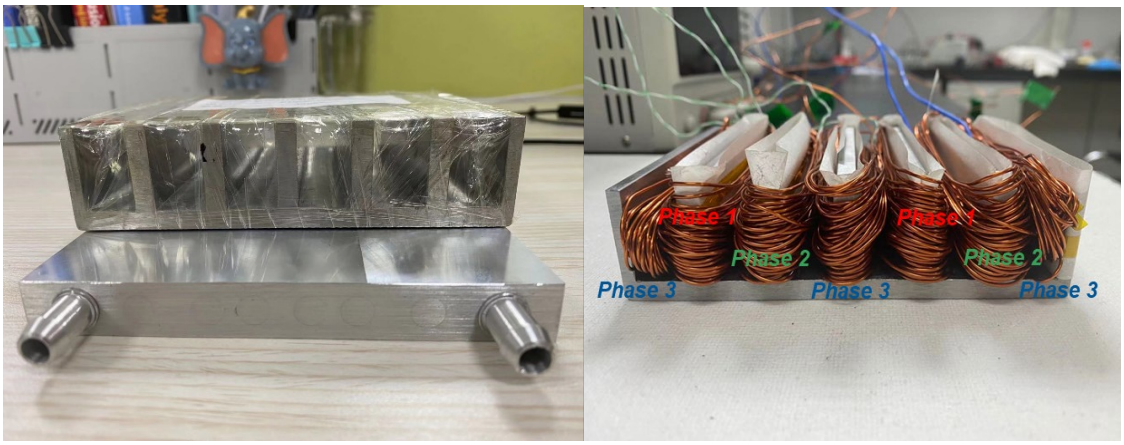

a) *b)*

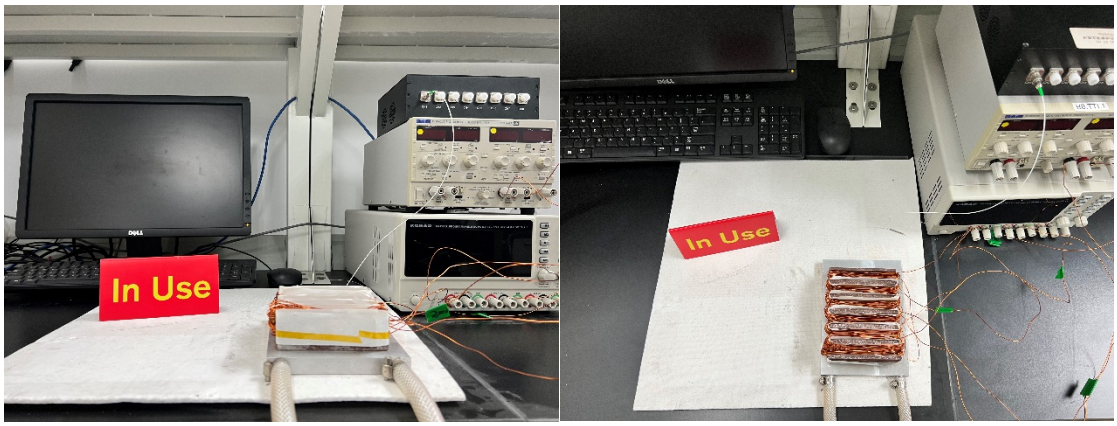

c) *d)*

Figure 5.3. Photos of a) Bare motorette and Aluminum waster jacket. b) Motorette with centralized three phase windings embedded. c) & d) Test-rig motorette with sensors embedded (two views).

The thermal experiments of motorette will be conducted once the experimental test bench completed based on the setup design above.

5.1.2 Simulation model construction

A lumped parameter thermal network (LPTN) model (Figure 5.4) of a 2-D one-slot radial cross-section of the thermal object (motorette) was constructed using Simulink Simscape for validation of our FBG thermal sensor: the slot was modeled as a series of thermal resistances from 6-node positions of slot to the ambient environment (natural-air cooling in our application). Assuming the predominant thermal dissipation in the motorette is in the radial direction and no iron losses needed to be considered since only DC powers were applied to the windings in our thermal experiments. The positions of six thermal nodes are spatially matched with those of FBG sensors (Figure 5.4b), therefore, two temperature datasets from 1) FBG experimental measurements and 2) LPTN analytical model, can be compared for the statistical analysis of our FBG thermal sensor system.

All thermal resistances used in LPTN model construction have been quantified and divided into four categories (R_air, R_copper, R_steel, and R_liner) depending on the types of materials, physical dimensions of the experimental object, and different modes of heat transfer [177]. The equivalent thermal conductivity of the windings is computed assuming equivalent winding consists of three kinds of materials [178]: pure copper, wire insulation, and air. Copper loss of one phase winding has been divided into six equal parts and applied to six thermal nodes, respectively. The ambient is assumed as a natural-air cooling environment under a constant temperature of 23°C.

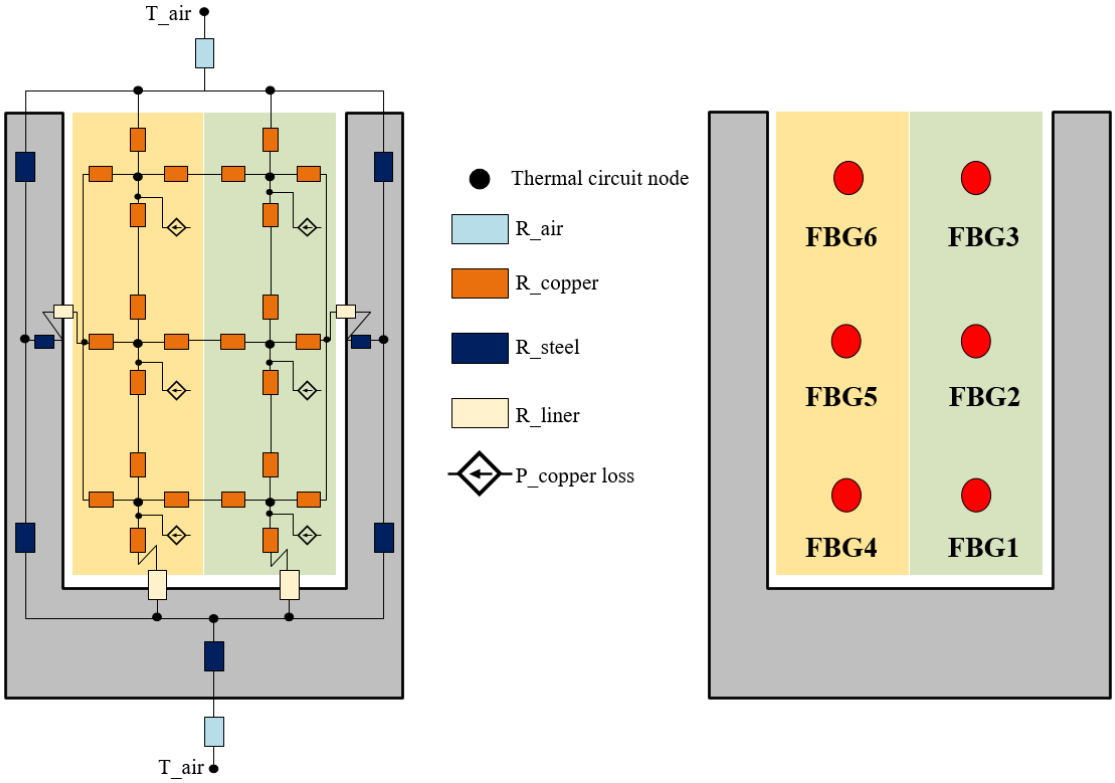

a) *b)*

Figure 5.4. a) Scheme of one-slot radial cross-section LPTN model. b) Scheme of one-slot radial cross-section FBG sensors implementation. It can be observed the positions of LPTN circuit nodes were matched with the FBG sensing points within the motorette.

The thermal simulation of motorette LPTN model will output the sequential temperature values at corresponding six nodes once the simulated load was applied, such load will be identical to the thermal experimental conditions for comparison.

5.1.3 Results & Discussion

Natural air cooling

For experimental thermal tests of EM windings with FBG sensors implemented: two international standard load duties (S3 & S9) were applied to EM copper windings by computing the output of the DC power supply. S3 mode used in this experiment was programmed as a constant 4A loading with duty factor 50%, two cycles applied with 1200 seconds for each cycle (Figure 5.5) while S9 mode consisted of a series of random loadings in the range of 0-5A (Figure 5.6). For the corresponding LPTN model, the same time-varying load patterns as S3 and S9 mentioned above were computed by calculating and applying equivalent copper losses to six thermal nodes. Temperature distribution within one slot was plotted and shown in Figure 5.5 and Figure 5.6, data obtained from both thermal experiments measured by FBG sensors and LPTN analytical model.

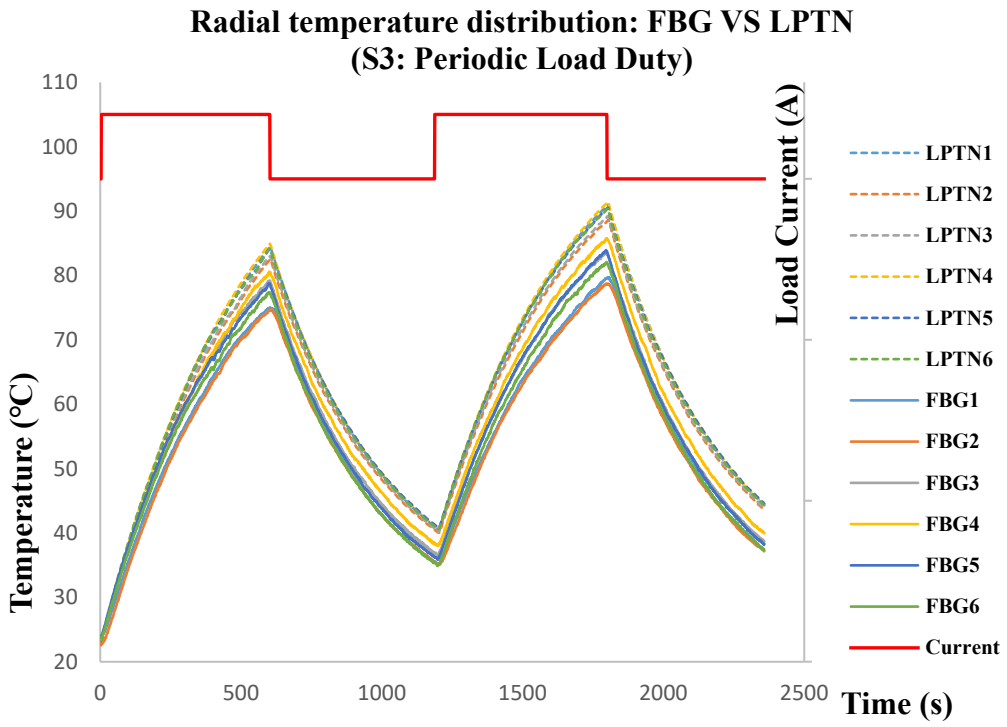

Figure 5.5. Temperatures at six positions of radial slot cross-section with periodic load (S3 mode) applied, data captured from experimental FBG sensors (solid line) and LPTN analytic model (dash line).

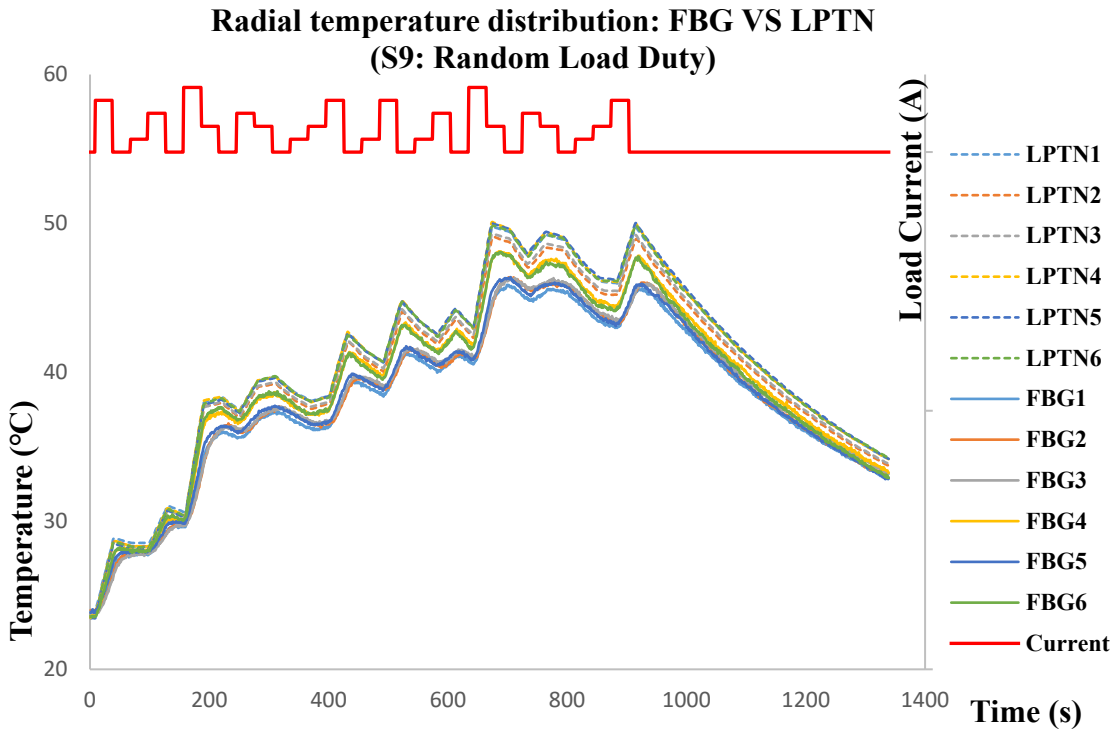

Figure 5.6. Temperatures at six positions of radial slot cross-section with random load (S9 mode) applied, data captured from experimental FBG sensors (solid line) and LPTN analytic model (dash line).

Figure 5.5 & Figure 5.6 compare the analytical LPTN model and experimental FBG sensor instrumented setup temperature results at six positions among radial cross-section of one slot of motorette. The experimental setup, as well as the LPTN model was conducted under a constant ambient temperature of 23 °C. As shown in the two figures, all temperatures at different positions are at the value of ambient, while their amplitudes varied gradually with time yet a strong correlation (Mean coefficient of determination $\overline{R^2} = 0.9419$) exists between FBG-measured and LPTN-simulated temperature curves. Such radial temperature difference at different positions indicated the hazard of the hot-spots occurrence within EM windings. In addition, the results of

LPTN model were slightly higher than those of the FBG experimental, which may be led by the value of equivalent thermal conductivity used in LPTN model: it is smaller than that of the instrumented experimental setup. However, the overall results of experimental FBG measured and those of LPTN model had a systematic difference within the manufacturing and experimental tolerances (i.e. 10℃) and the FBG sensing system can provide a spatial resolution of 8 mm, a fast wavelength sweeping frequency (up to 1 kHz), and stable linear temperature sensitivity of 0.091 ℃/pm. These performance parameters of the FBG temperature sensor system indicate the feasibility of using FBG sensor system for thermal monitoring of EM windings.

Forced- water cooling

The S3 and S9 (two different patterns of S9) duty modes were applied experimentally for the validation of FBG temperature sensors used for motorette. Both natural air cooling & forced water cooling methods were investigated in our thermal experiments.

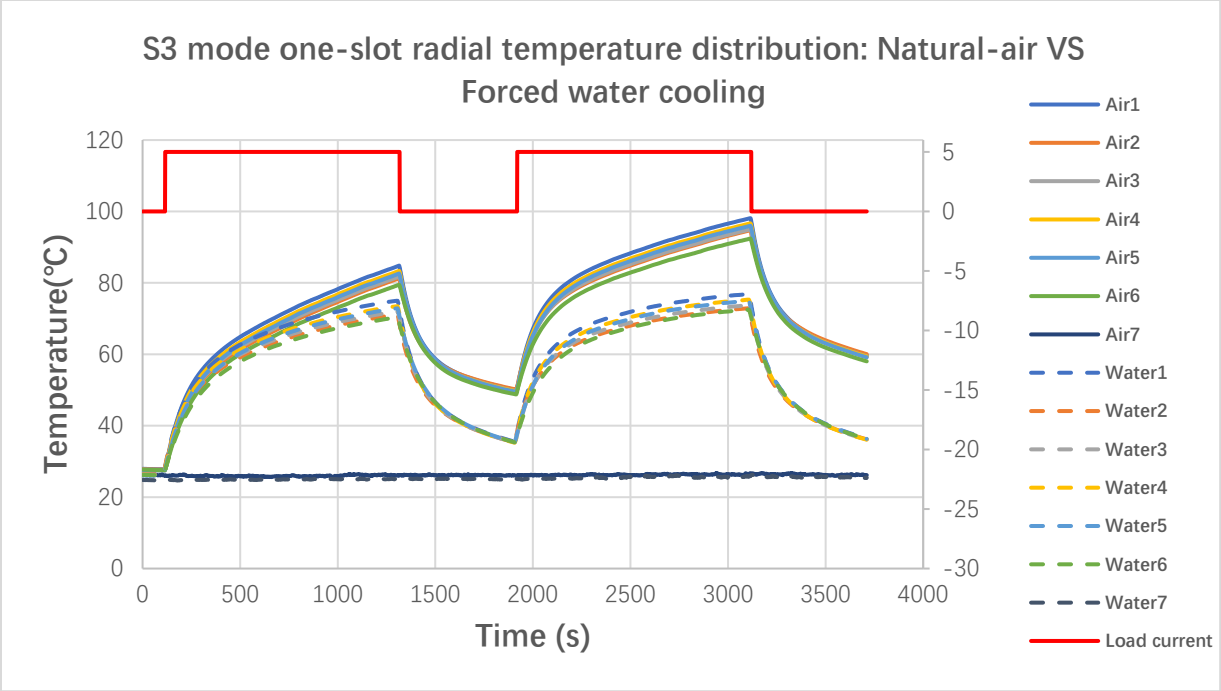

Figure 5.7. Temperatures at six positions of inner copper windings within motorette with S3 mode applied. S3 load current pattern is shown in the top line. Position_7 for both cooling methods are set for ambient temperature recording. It can be observed that the forced water cooling setup had a higher cooling rate than that of natural air cooling system.

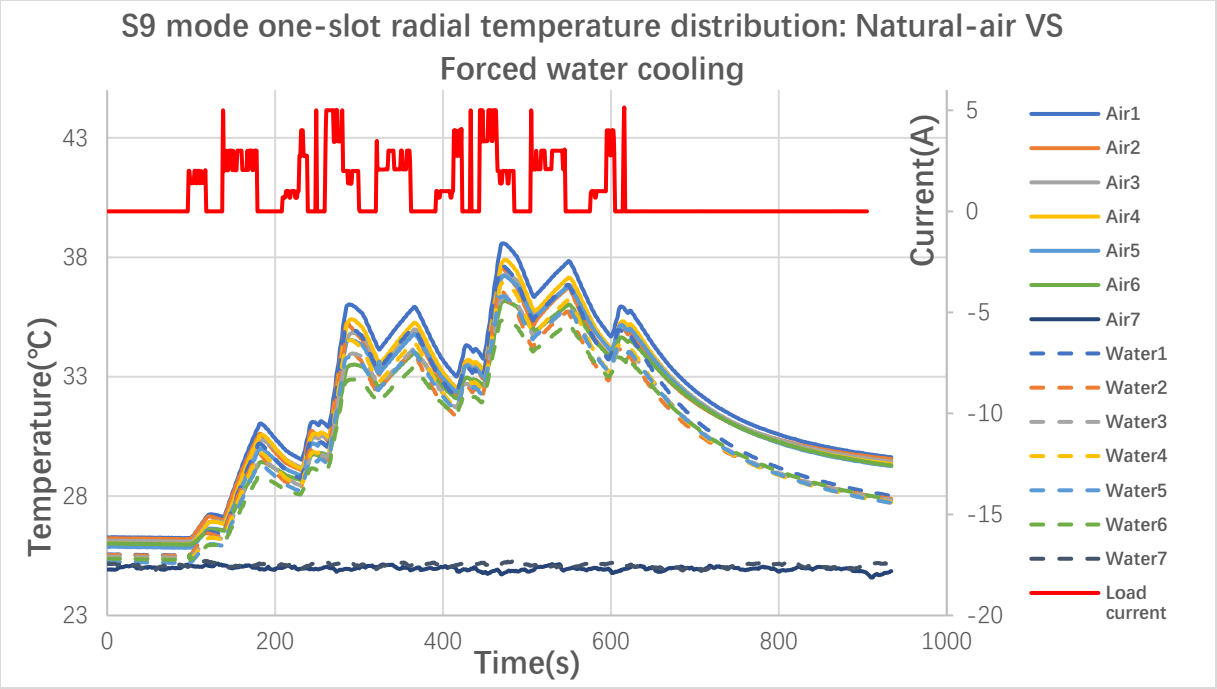

Figure 5.8. Temperatures at six positions of inner copper windings within motorette with S9 mode (pattern 1) applied. S9 load current pattern is shown in the top line. Position_7 for both cooling methods are set for ambient temperature recording. It can be observed that in S9 mode test, rather than periodic and long-term load, random and pulsed load current supplies were applied. Short-pulsed load current (1 second) were applied to the copper winding and the plot indicated temperature of copper winding was affected by the pulsed current. FBG sensors can capture those 'thermal ripple' with sufficient sensing response.

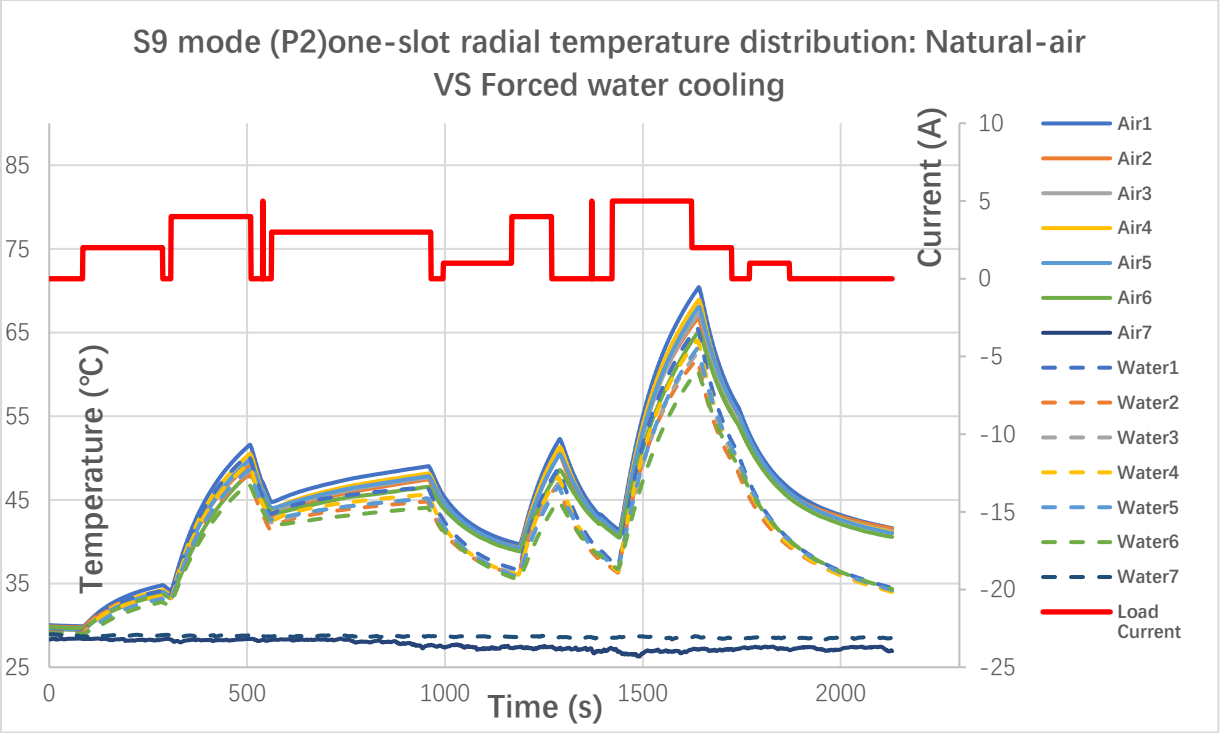

Figure 5.9. Temperatures at six positions of inner copper windings within motorette with S9 mode (pattern 2) applied. S9 load current pattern is shown in the top line. Position_7 for both cooling methods are set for ambient temperature recording.

From the thermal plots of motorette above (Figure 5.7, Figure 5.8, Figure 5.9), it can be observed that with forced water cooling system introduced, the corresponding inner temperatures at different positions within windings decreased dramatically. Additionally, such thermal decline occurred in thermal rate as well as the temperature amplitudes. This phenomenon was led by the good thermal conductivity of the aluminum jacket and the water flow through it. For the motorette experimental data collection, several sensors were employed: DC power supply was used for electric current and voltage data collection, FBG sensors for temperatures data collection, and water cooler can record the flow rate and temperature of cooling water flow.

The motorette thermal experiments above demonstrated that the FBG sensors can capture the temperature difference inside the copper windings led by various EM cooling methods. However, for practical using of FBG sensors, it is hard to implement optical fibres within each EM for thermal monitoring. In addition, such in-situ sensor installation approach has no good for sensor hardware maintenance and replacement. The failure of thermal sensors within EM copper windings may lead to failure of operating EMs. For the safe consideration, we need to seek a solution for EM temperature sensor optimization: both in sensor implementation positions and sensor numbers. As the continuation of ML temperature prediction model for copper windings shown in Chapter 4, a new ML model for motorette will be constructed.

5.2 ML models for motorette internal temperature prediction

5.2.1 ML model deployment

SVR algorithm based model will be constructed for internal winding temperatures estimation and prediction. The SVR model structure is shown in Figure 5.10. The input features were selected from the EM operating parameters that will contribute to temperature rise. These features were divided into three categories: sensor measurement variables, electrical variables, and environmental variables. Compared to the previous ML temperature estimation model that we built last year, two new environmental variables were added: coolant velocity and temperature. Since we found in previous “natural-air VS forced water” thermal experiments, the cooling method has a significant effect on the thermal distribution of motorette.

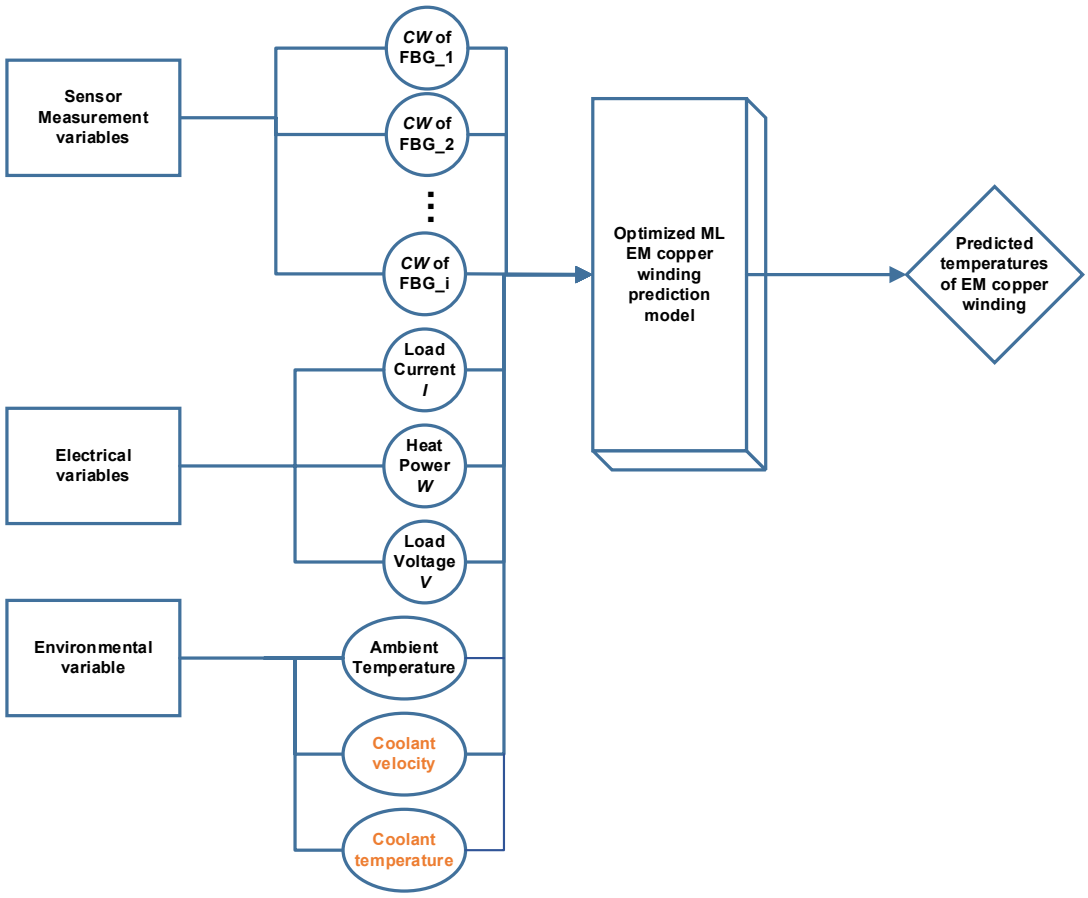

Figure 5.10. Structure of SVR model for motorette inner winding temperatures estimation. Compared with the ML temperature prediction structure shown in Figure 4.13, new input features of this version of ML model are shown in "orange" color. The coolant velocity and temperature were measured and recorded by the industrial water cooler (S&A CW-3000).

The SVR ML model will be trained, validated and tested for the motorette internal winding temperature prediction following the same process as shown in Figure 4.14 in last Chapter.

5.2.2 Results & Discussion

The dataset of S9 duty mode collected during motorette thermal experiments were processed and

sent to the SVR model for temperature estimation test. The ML model temperature outputs (Water_SVR) VS experimental temperature values (Water_EXP) were plotted as shown in Figure 5.11. Although there were some outlier values can be observed from the plots, values of four regression performance indices were still good: $e_{MAE} = 2.692, e_{MAPE} = 6.152\%, e_{RMSE} = 3.721, R^2 = 0.9619$. It illustrated that our SVR model presents a good regression performance for motorette temperature estimation in time series.

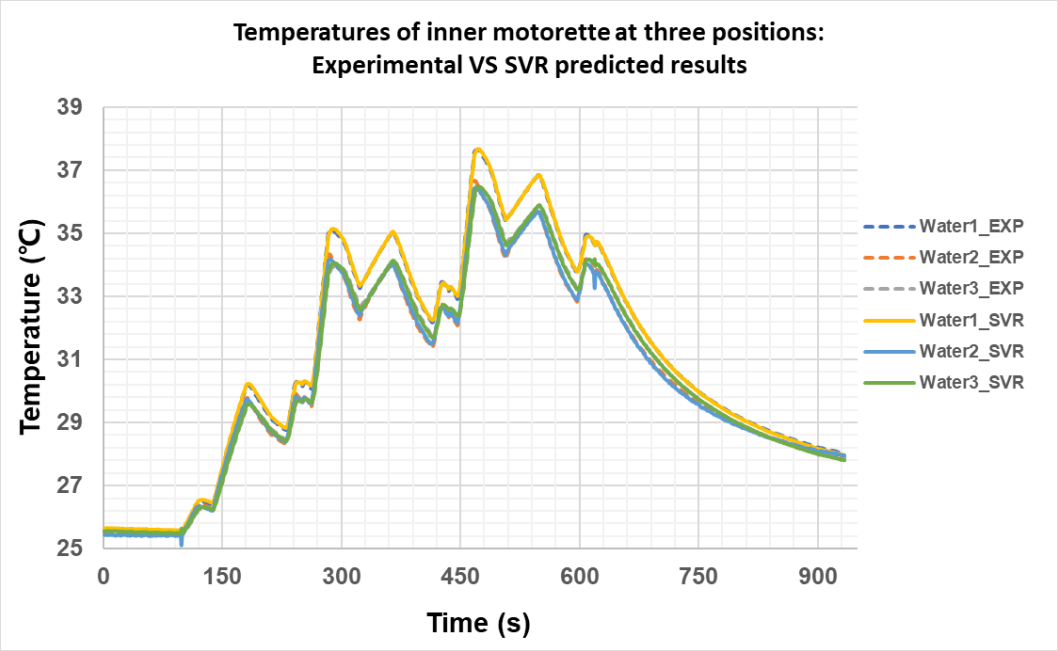

Figure 5.11. S9 mode inner winding temperatures plot comparison, the experimental measured temperature values (dash curves) VS SVR model output values (solid curves) at same corresponding positions inside motorette windings.

The multioutputs ML temperature prediction model for can be considered as a "proof-of-concept" ML model test for our application: it is feasible to use ML algorithms for partial EM physical model (motorette) thermal monitoring with acceptable accuracy rather than only for copper

windings shown in Chapter 4. Additionally, the sensor number can be reduced with no thermal resolution affected. Further investigation will be presented in next Chapter, where the thermal object has been finally updated to a real operating EM and more ML regression algorithms will be built for temperature prediction performance comparison.

5.3 FBG with Motorette: summary of the findings

To sum up, we designed, implemented and validated two different versions of FBG thermal sensor prototypes for motorette. Including natural-air cooling as well the forced water cooling motorette test rigs for comprehensive thermal monitoring using FBG sensors implemented within. Additionally, the thermal modelling of manufactured copper windings was conducted using LPTN modeling method by Simscape simulation environment. Compared to Siemens MagNet & ThermoNet software used in Chapter 4, the LPTN method is able to simulate the self-designed duty modes of motorette, the simulation results demonstrated a strong correlation with the FBG temperature measurement results, the difference of temperature values were discussed as well. Finally, an example of ML temperature prediction model for motorette was designed and constructed based on SVR algorithm. Compared to the SVR model in Chapter 4, the trained model in this chapter presented an accurate winding temperature prediction performance with multiple target temperature outputs at different positions within motorette. Such achievement is a big step for solving our research question: how to use optimal number of sensors for comprehensive thermal monitoring of EM. The next stage of our sensor prototype will be the final stage of this project: FBG-ML thermal monitoring prototype for a real operating EM.

6 Thermal Experiments: FBG with Electric Machines

In this chapter, the target objective under-test has been moved to the final stage: a real operating EM. To solve the inner winding temperatures blind problem with optimized number of temperature sensors employed, an FBG-ML combined winding temperature monitoring system is proposed and validated experimentally. Compared to the conventional thermal monitoring methods for EM winding temperature, our solution provides the advantages including: 1) Obtaining comprehensive temperature distribution of copper windings with optimized sensor number. 2) Employing FBG sensors that has intrinsic physical properties for EM winding thermal monitoring application. 3) Using our novel method of sensing data combined with trained machine learning models, some shortcomings that exist in conventional temperature monitoring methods can be fixed. For instance, defects for direct measurement method include: the location of the measurement point is difficult to determine, there are blind spots in temperature measurement, and it is impossible to arrange a large number of thermocouple sensors, etc. For FEA method: long modeling and simulation time consumption, requiring detailed electromagnetic, material, and dimensional parameters corresponding to the specific EM, unconscious of the actual temperature distribution in the practical EM operating scenarios.

6.1 Thermal monitoring study of EM

The overall system design of FBG-ML EM thermal monitoring system will be presented first. For ML modelling part, feature engineering, multiple ML algorithm architectures and data preprocessing methods will be presented. For the test-rig construction part, multi-sensors of EM

will be employed for data collection. Since the completion of proposed test bench, thermal experiments of EM under various operation duty-cycles will be applied for full dataset construction.

6.1.1 Feature engineering for EM winding thermal monitoring application

The basic temperature sensing principles of FBG have been introduced in the literature review chapter (Chapter 2) with formulas and optical spectrum demonstration (Figure 2.2), which will not be repeated here. Since our target object, EM windings, remains physically static in our thermal experiments, the wavelength shift is always induced by temperature changes, while strain-induced variation can be neglected. Additionally, the CWs of FBG will be employed as an input feature of ML model while the target outputs are internal winding temperatures, we may leave the strain effect compensation to the training and optimization process of ML models.

It is commonly known that the overheating within windings of EM are the fatal problem for the safe operations and long lifetime maintenance of EM. The undesired heat sources of EMs consist of three types of operating losses generally: Ohmic (copper) losses, Core (iron) losses (Equation 6.1, 6.2) and Mechanical losses [179]. As explained, the maximum temperature rise as well as the highest temperature points occur within EM windings, which was dominantly led by copper loss. For copper losses, it mainly consists of: 1) winding DC resistance losses $\boldsymbol{P_{Cu}}$. 2) High frequency additional winding losses $\boldsymbol{P_{Cuad}}$, which is led by flux leakage and skin-effect and the value of this type of additional loss is highly related to EM frequency $\boldsymbol{f}$.

$$\text{DC resistance winding loss: } P_{Cu} = \sum_{i=a}^{c} (I_i^2 R_i) \tag{6.1}$$

$$\text{High} - \text{frequency additonal winding loss: } P_{Cuad} = (k_F - 1)P_{Cu} \tag{6.2}$$

$$\text{electron penetration depth: } \delta_c = \sqrt{\frac{2}{\omega\gamma\mu}} = \sqrt{\frac{1}{\pi f \gamma_e \mu_e}} \tag{6.3}$$

Where $\boldsymbol{\gamma_e, \mu_e}$ are the electric and magnetic conductivity of conductor, respectively. $\boldsymbol{f}$ is the EM operating frequency while $\boldsymbol{\omega}$ is the angular velocity. $\boldsymbol{k_F}$ is the increasing factor of winding resistance with empirical value.

It can be observed in equation (6.3), for the electron penetration depth $\boldsymbol{\delta_c}$, the higher the EM operating frequency, the lower the electron penetration depth, the stronger the skin effect, and the larger the additional winding loss. This type of copper loss $\boldsymbol{P_{Cuad}}$ is hard to be expressed analytically and highly related to EM operating frequency. In terms of the iron loss of EM, it can be expressed in equation (6.4):

$$P_{Fe} = P_h + P_c + P_e = k_h f B_p^x + k_c f^2 B_p^2 + k_e f^{1.5} B_p^{1.5} \tag{6.4}$$

Where $\boldsymbol{P_h, P_c, P_e}$ are magnetic hysteresis loss, classical and exceptional eddy current losses, respectively. And $\boldsymbol{k_{h,c,e}}$ are corresponding coefficients of these above types of losses. $\boldsymbol{B_p}$ is magnetic flux density amplitude.

Mechanical losses within EM which are mainly friction and fluid losses (mainly windage resistance loss) can be measured by determining the input to the machine running at the proper rotating speed (as shown in Equation 6.5 and 6.6). Frequently they are lumped with core loss and determined at the same time during the loss analysis.

We may calculate the EM heat loss in another way: by determining the overall input electrical power P_{in} as well as the output mechanical power P_{out}, the difference between them can be considered as the overall EM heat dissipation P_{heat}, which can be derived as follow:

$$n_1 = \frac{60 \times f}{p} \tag{6.5}$$

$$r = n_2 = {60 \times P_{out}}/{2\pi\tau} = \frac{9.549 \times P_{out}}{\tau} \tag{6.6}$$

$$P_{heat} = P_{in} - P_{out} = UI - \frac{r\tau}{9.549} = 3k_{power}U_{phase}I_{phase} - \frac{r\tau}{9.549} \tag{6.7}$$

Where $\boldsymbol{n_1}$ is Synchronous speed, n_2 is rotor speed which equals to machine rotating speed $\boldsymbol{r}$. All speeds in the unit of RPM and torque in the unit of N·m. $\boldsymbol{k_{power}}$ is the power factor, $\boldsymbol{U, I, U_{phase}, I_{phase}}$ are operating bus voltage, bus current, phase voltage and phase current, respectively.

The above formula (Equation 6.7) for heat dissipation calculation is suitable for single 3-phase EM. Therefore, it can be found that the additional winding losses, iron losses and mechanical losses of EM have following common characteristics:

1) They are all hard to be calculated analytically with high accuracy, the relative FEA tools.

2) They are all strongly correlated with EM frequency, and the EM operating frequency $\boldsymbol{f}$ is proportional to EM rotating speed.

It can be observed from Equation 6.7 that the overall heat loss power of EM $\boldsymbol{P_{heat}}$ can be roughly expressed by four EM operating features[$\boldsymbol{U, I, r, \tau}$], so we choose $\boldsymbol{U, I}$ as electrical input features and $\boldsymbol{r, \tau}$ as mechanical input features for our ML temperature prediction model construction. They all have significant contributions to EM winding temperature rise.

For now, the related electrical & mechanical features were introduced above for the construction of our temperature prediction ML model construction. However, if we build our ML model based on only electrical and mechanical features, it is quite similar with the conventional analytical thermal simulation methods for EMs. Such features are not enough for dealing with the unexpected practical temperature distribution during EM operating scenarios. Therefore, real-time thermal sensing data are required as additional input features. Other two categories of thermal sensing features were involved for the compensation of unexpected conditions: simultaneous central wavelengths of FBG sensors [$\boldsymbol{CW_1, \ldots CW_N}$] and temperatures measured by in-situ thermocouples [$\boldsymbol{T_1, T_3 \ldots T_{2M-1}}$] inside EM windings. $\boldsymbol{N}$ and $\boldsymbol{M}$ are the count-related numbers for FBG sensing points and target positions of EM windings, respectively**.**

The final structure of a complete dataset $\boldsymbol{S}$ for ML model includes:

$$S = \{[X, Y]_i\}_{i=1}^{n}, [X, Y]_i \in R$$

Within the dataset S, multi-scale input features $\boldsymbol{X_i}$:

$$X_i = [CW_1, \ldots CW_N, I, V, \tau, \mathrm{r}, T_1, T_3 \ldots T_{2M-1}]_i$$

Target multiple temperature outputs $\boldsymbol{Y_i}$:

$$Y_i = [T_1, T_3 \dots T_{2M-1}]_i$$

where $\boldsymbol{i}$ represents the $\boldsymbol{i\_th}$ order sample array in time series containing the multi-dimensional input features and the target outputs of temperatures, $\boldsymbol{n}$ represents the total sample size, and $\boldsymbol{R}$ represents the real number set.

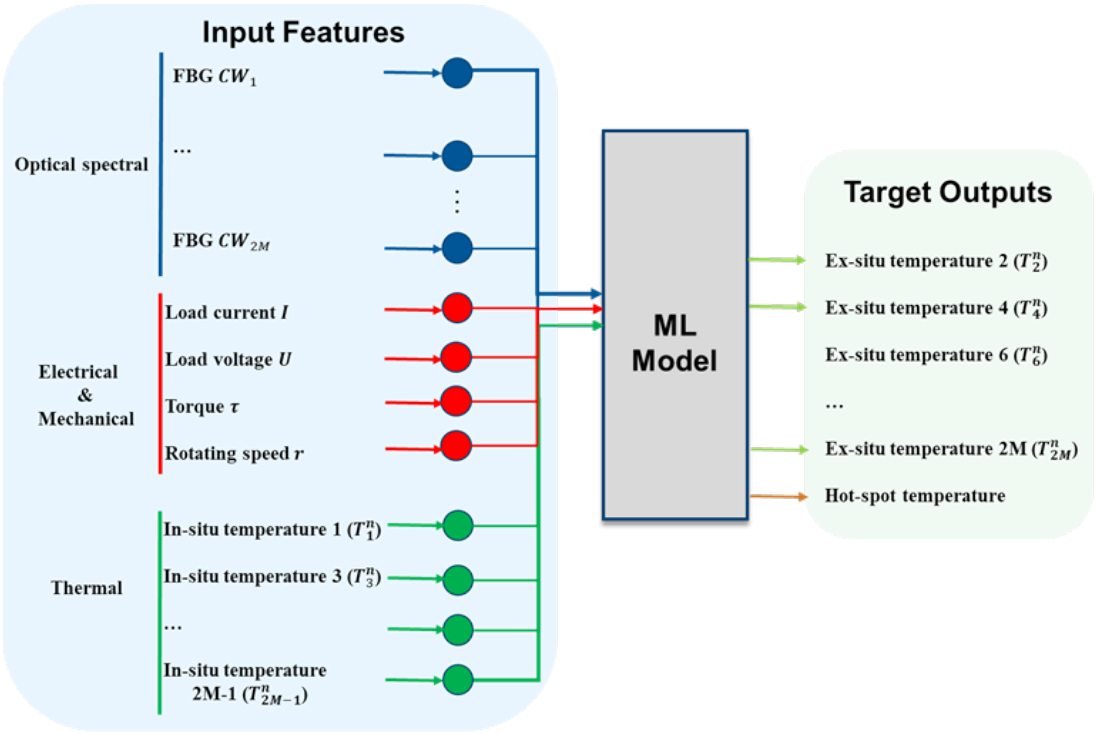

Figure 6.1. Overall ML regression model structure for internal EM winding temperature monitoring task. Including input features in three categories, "black-box" regression ML model, and target internal winding outputs at different positions inside winding.

The overall ML model structure was designed as shown in Figure 6.1. The detailed ML model structures for different ML algorithms will be presented in next section.

6.1.2 ML algorithm architecture

Support Vector Machine Regression (SVR)

The temperature distribution of different positions inside the EM copper winding exhibits nonlinear characteristics over time, so we map the input features from the low-dimensional space to the high-dimensional space $\mathbf{x} \rightarrow \boldsymbol{\phi}(\mathbf{x})$ through nonlinearity (Figure 6.2), to facilitate the realization of support vector regression (SVR) in the high-dimensional feature space operation, the hyperplane function f(x) of the nonlinear mapping can be expressed as:

$$f(x) = \omega^T \cdot \phi(x) + b \tag{6.8}$$

Among them, **ω, x, b** are weight coefficient, input features and intercept respectively. In order to solve the parameters of the hyperplane function, we introduce slack variables $\{\xi_i^-\}_{i=1}^n$ and $\{\xi_i^+\}_{i=1}^n$, which control the upper and lower bounds of the output. The goal becomes to find the hyperplane function f(x) that satisfies:

$$\begin{cases} \mathrm{f(x)} = \omega^T \cdot \phi(\mathrm{x}) + \mathrm{b} \\ \min R\,(\omega, b, \xi) = \dfrac{1}{2}\|\omega\|^2 + C\sum_i^n (\xi_i^- + \xi_i^+) \end{cases} \tag{6.9}$$

$$\text{s.t.} \begin{cases} y_i - f(x) \le \varepsilon + \xi_i^- \\ f(x) - y_i \le \varepsilon + \xi_i^+ \end{cases} \text{and} (\xi_i^-, \xi_i^+ \ge 0, \varepsilon > 0) \tag{6.10}$$

Where $\boldsymbol{\varepsilon}$ is the parameter of the epsilon-insensitive loss function combined with L2 regularization, and $\boldsymbol{C}$ is the penalty factor related to squared L2 penalty for epsilon – insensitive loss function. To find the optimal function solution for formula (6.9), we need to introduce the Lagrange multiplier $\boldsymbol{\alpha_i}, \boldsymbol{\alpha_i^*}$ and types of kernel functions to construct the Lagrange equations, then formula (6.9) can be

transformed into an equivalent quadratic programming dual problem shown in formula (6.11), expressed as follows:

$$\max R\left(\alpha_i, \alpha_i^*\right) = -\frac{1}{2}\sum_{i,j}^{n}\left[\left(\alpha_i^* - \alpha_i\right)\left(\alpha_j^* - \alpha_j\right)\phi(x_i)\phi\left(x_j\right)\right] + \sum_{i}^{n}\alpha_i^*(y_i - \varepsilon) - \sum_{i}^{n}\alpha_i(y_i + \varepsilon) \tag{6.11}$$

$$\text{s.t.}\begin{cases}\sum_{i}^{n}\left(\alpha_i - \alpha_i^*\right) = 0 \\ \alpha_i \geq 0, \alpha_i^* \leq C\end{cases} \tag{6.12}$$

After solving the minimum value of the Lagrange equations in formula (6.12), the support vector regression function including the non-linear mapping of the kernel function can be obtained, which is expressed as follows:

$$\text{f(x)} = \sum_{i,j}^{n}\left[\left(\alpha_i - \alpha_i^*\right)K\left(x_i, x_j\right) + b\right] \tag{6.13}$$

In formula (6.13), $K\left(x_i, x_j\right) = \phi(x_i)\phi\left(x_j\right)$, which is the kernel function of support vector regression model. x_i, x_j are the i_th and j_th input feature vectors.

In our winding internal temperature prediction task, the selected kernel functions include (formula 6.14-16): radial basis (RBF) kernel function $K_1(x_i, x_j)$, Sigmoid kernel function $K_2(x_i, x_j)$, polynomial kernel function $K_3(x_i, x_j)$, with their expressions are as follows:

$$K_1\left(x_i, x_j\right) = \exp\left(-\gamma\left\|x_i - x_j\right\|^2\right) \tag{6.14}$$

$$K_2(x_i, x_j) = \tanh(\gamma x_i^T x_j + b_0) \tag{6.15}$$

$$K_3(x_i, x_j) = (\gamma x_i^T x_j + b_0)^d \tag{6.16}$$

The math symbols mentioned in formula 6.14-6.16 are same as the hyperparameters symbols defined in sci-kit learn software library. The names and range of these SVR hyperparameters will be presented in *Table 6.3*.

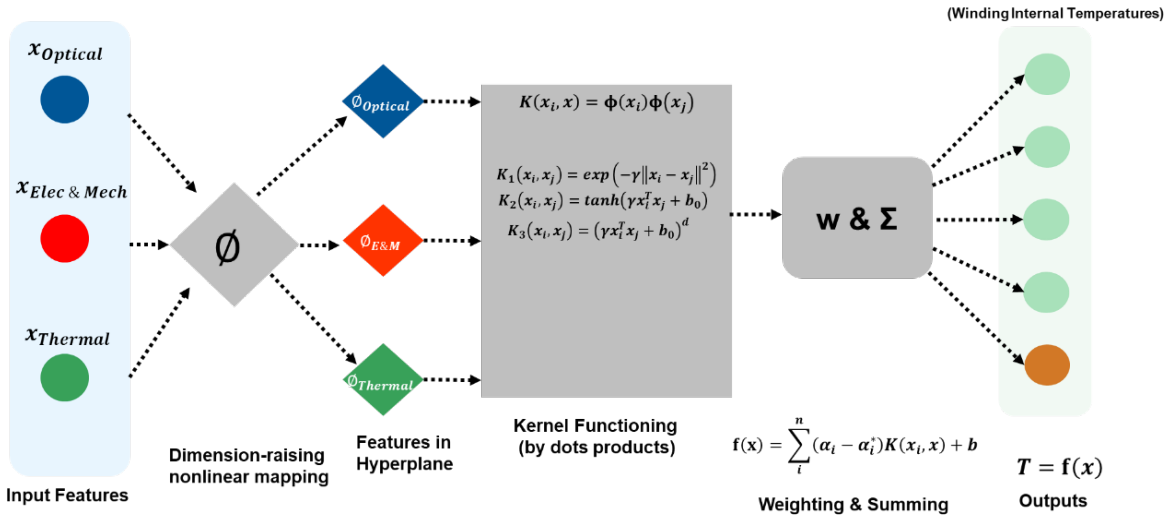

Figure 6.2. The structure of SVR model for EM internal winding temperature prediction. This structure presents the details inside the "grey box" of ML model shown in Figure 6.1 based on SVR algorithm. Kernel functioning is the core method for SVR model, and three types of kernel functions were employed and tested for optimal SVR model construction.

Multi-layer Perceptron Regression

Here we employed the vanilla form of artificial neuron network (ANN)-Multi-layer Perceptron Regression (MLPR) method (Figure 6.3) to build a model for our internal winding temperatures

estimation task. Both SVR and MLPR models were developed based on the single perceptron structure, while SVR employed kernel method and MLPR introduced "neurons" within multiple hidden layers, activation function for hidden layer outputs, and back-propagation (BP) methods to train the ANN model for solving the nonlinear regression problem. In our application, several types of solvers for weight optimization during BP process and activation functions were employed for seeking the optimal MLPR model structure. The solver/optimizer function types including L-BFGS [180] , stochastic gradient descent (SGD) [181] and adaptive moment estimation (Adam) [182]. The options of activation functions (formula 6.17-20) including identity function $A_1(x)$, logistic sigmoid function $A_2(x)$, hyperbolic sigmoid tan (tanh) function $A_3(x)$, and rectified linear unit (ReLU) function $A_4(x)$, with formulas shown:

$$A_1(x) = \mathrm{x} \tag{6.17}$$

$$A_2(x) = 1/[1 + \exp(-x)] \tag{6.18}$$

$$A_3(x) = \tanh(x) \tag{6.19}$$

$$A_4(x) = \max\ (0, x) \tag{6.20}$$

The MLPR model employed square error loss function with MLPR regularization parameter α (equation 6.21) to determine the structure of ANN regression model for internal winding temperature prediction task:

$$\alpha = 1/2C \tag{6.21}$$

where $\boldsymbol{C}$ is the same penalty factor introduced in SVR model part. MLPR regularization parameter α is introduced here since it is one of the hyperparameters of MLPR algorithm in sci-kit learn ML package, which will be employed for ML model training and optimization later. The names and range of these MLPR hyperparameters will be presented in *Table 6.3*.

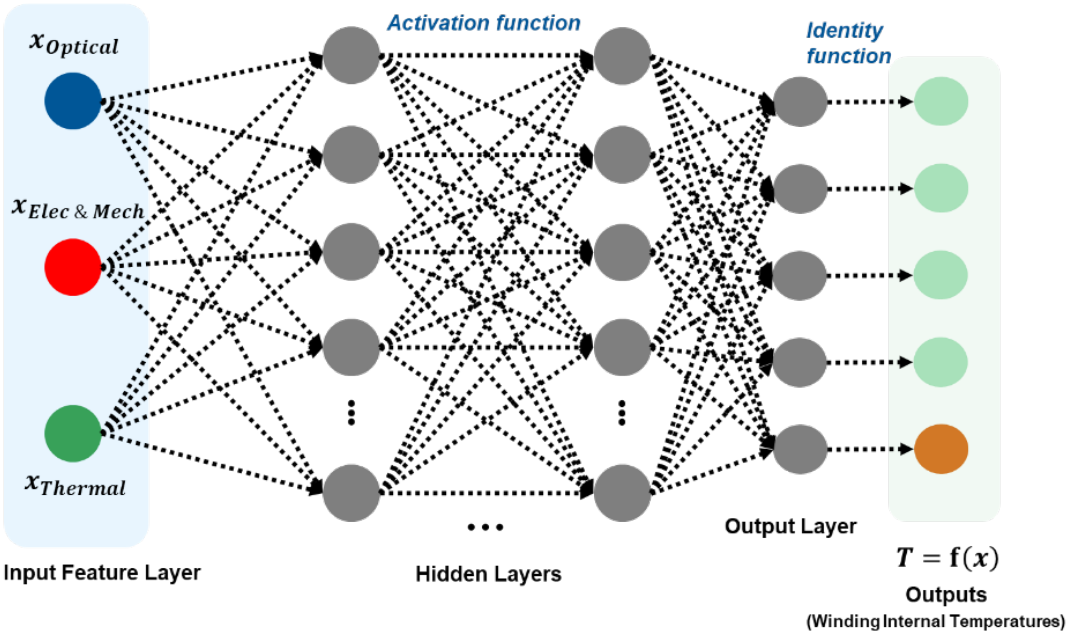

Figure 6.3. Structure of MLPR (ANN) model for EM internal winding temperature prediction. This structure presents the details inside the "grey box" of ML model shown in Figure 6.1 based on ANN algorithm. The size of neuron network (including number of layers and neurons within each layer) and types of activation functions need to be determined for the construction of our target temperature prediction ANN model.

Random Forest Regression

Random Forest Regression (RFR) is a type of Bagging ensemble machine learning algorithm [183], which mitigate the overfitting problem of conventional decision tree algorithm. Unlike the two

methods SVR and ANN above, the basic idea of RFR is training several single "weak" models and combining them together to perform as a "powerful" model for specific task with improved regression performance. Here the single model we employed was decision tree (CART) [184] , after training all the "trees" using bootstrap sampling algorithm , we summed the values of trees' outputs and took the mean value as the RFR model final output (Figure *6.4*). Therefore, for the construction of RFR model, two main parameters were required to be determined: the number of trees $\boldsymbol{k}$ within the forest and the maximum depth of each tree $\boldsymbol{dep_{max}}$. Additionally, statistical means (e.g. absolute error, square error, Poisson deviance) can be employed as the node impurity function for RFR model output evaluation.

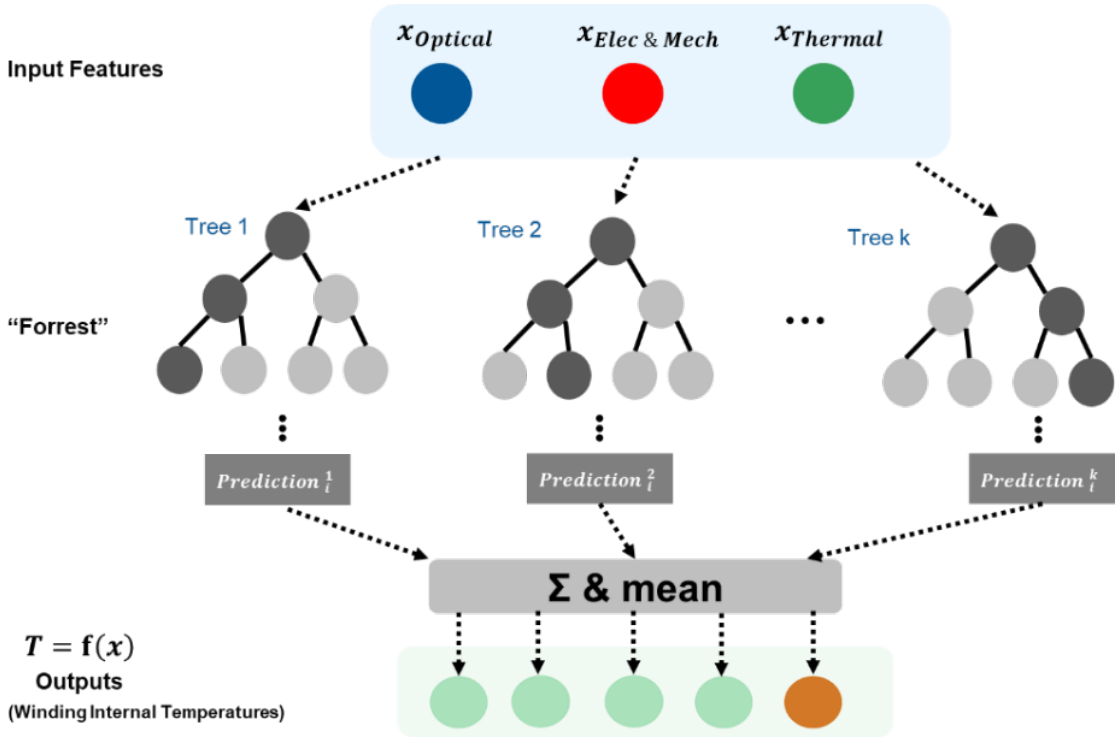

Figure 6.4. Structure of RFR model for EM internal winding temperature prediction. This structure presents the details inside the "grey box" of ML model shown in Figure 6.1 based on

RFR algorithm. The size of "forest" is scenario-dependent and needs to be determined for the EM thermal monitoring application.

Table 6.1. Scope of multiple ML regression algorithms chosen for EM winding Temperature Prediction Application. The content of this table was summarized and modified upon [185].

SVR	ANN (MLPR)	RFR
Good generalization ability for nonlinear regression problem	High regression accuracy can be achieved by tuning	Simple statistical principle and easy to be implemented
Suitable for small sample size & non-large feature dimensions problem	Strong nonlinearity fitting ability	High tolerance to noise & outliers
Shallowing learning structure: good interpretable & low calculation complexity	Relative high data fault tolerance (since the number of neurons is large)	Able to avoid overfitting somehow (since each tree randomly selected part of features)
Sensitive to the choice of kernel & the values of SVR hyperparameters	Time-cost and overfitting occur with the increase of neuron and layer number (i.e. large-scale deep network)	Complex hyperparameters to be tuned
Hard to be trained & constructed for the very large-scale data	No specific principle for parameter tuning (experience-dependent), poor interpretable	Training time costly as the number of tress increase
Poor regression performance for high dimension feature scenario	Trade-off between high regression accuracy and generalization ability	Cannot make predictions that go beyond the scope of the training set data

The literature analysis of three types of ML algorithms were described in Table 6.1. The trade-offs of ML algorithms were listed and the actual ML models based on these algorithms are required for the comparison of temperature prediction performances after the experimental test-rig construction.

6.1.3 FBG-ML combined EM multi-sensor system construction

In this section, the construction process of EM multi-sensor test-rig will be presented. The structure of customized multi-grating FBG string for winding thermal monitoring is demonstrated in Figure 6.5 with its optical intensity spectrum in static condition under general room temperature 25 ℃ (Figure 6.6). The TCs and FBG sensors layout and practical implementation is demonstrated in Figure 6.7. Additionally, the operating specifications of under-test Brushless Permanent Magnet Outer Rotor (BPMOR) EM for thermal experiments is shown in Table 6.2.

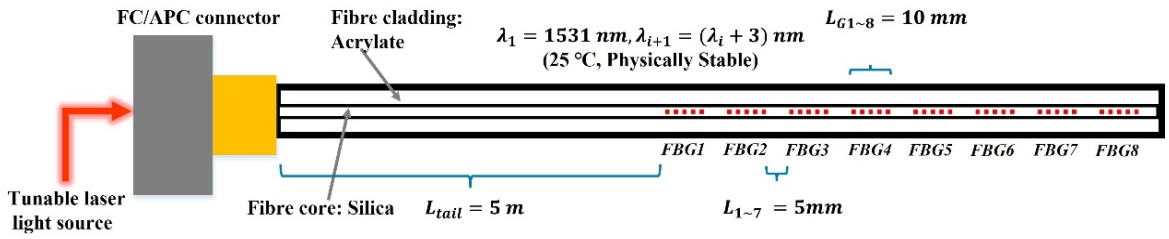

Figure 6.5. Structure of 8-point multi-grating FBG sensors with wavelength division multiplexing technique applied.

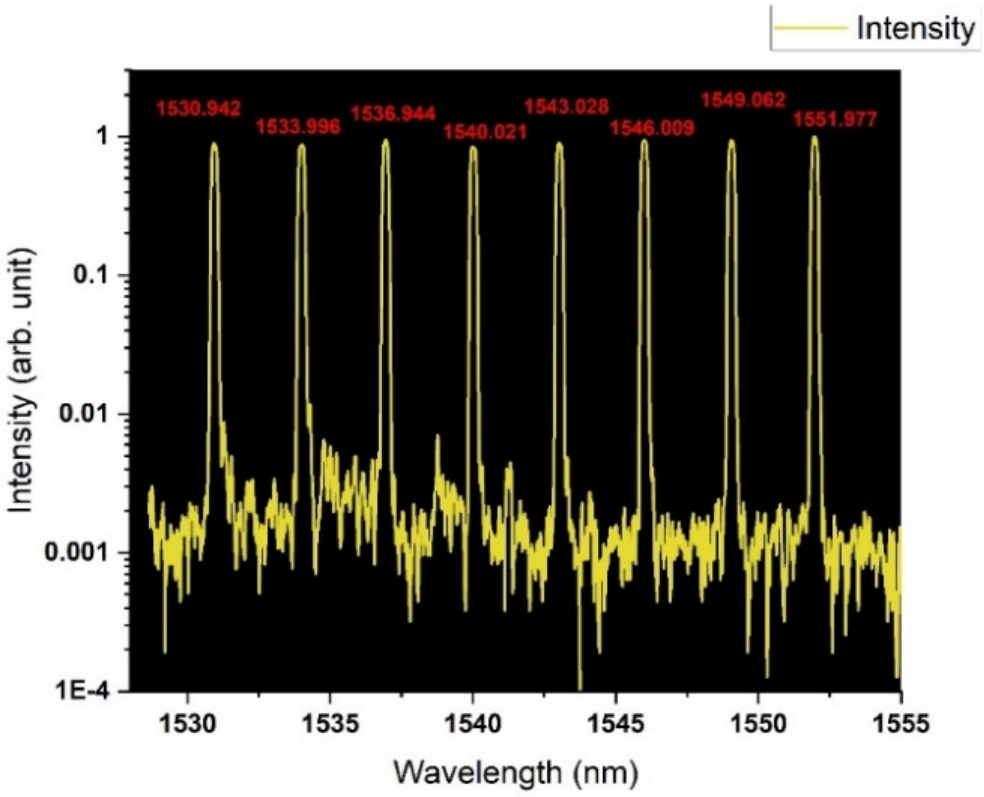

Figure 6.6. Optical spectrum of 8-point multi-gratings FBG (physically stable, 25℃). The initial central wavelengths of each grating were labelled on the top of spectral peaks.

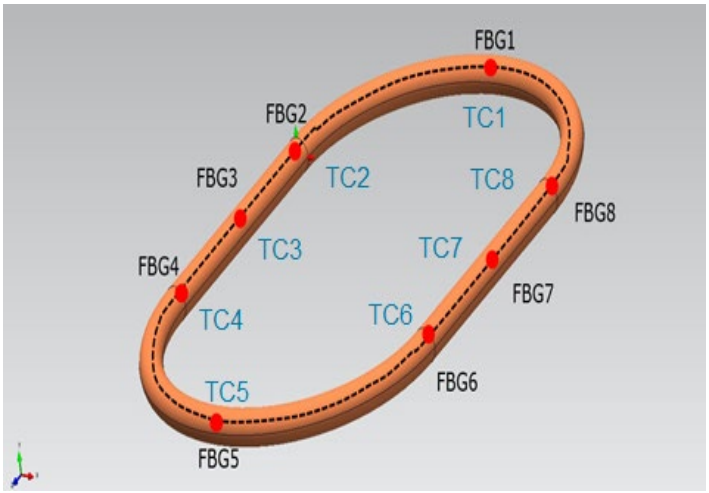

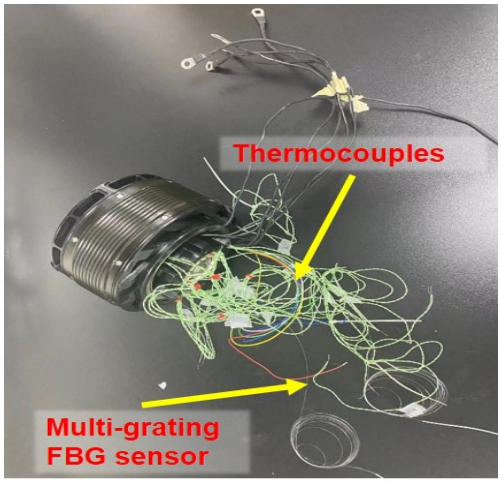

a) *b)*

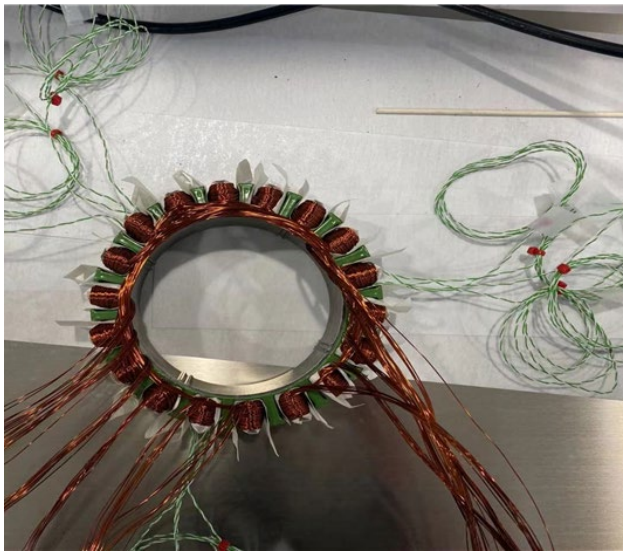

c)

Figure 6.7. Temperature sensors implementation a) scheme design, and b) demonstration photo of sensors implementation. Both TCs and FBG multi-grating string were implemented within EM copper winding for data acquisition and further ML model performance validation. c) Photo of EM copper winding manufacturing process with temperature sensors embedded.

Table 6.2. Specifications of Brushless Permanent Magnet Outer Rotor (BPMOR) EM used in our thermal experiment.

BPMOR Electric Motor specifications ***(Nominal condition: under 47-inch carbon fibre propeller loaded condition)***	
Rated Power (Nom. / Max.)	6 kW / 12 kW
Winding type	Double 3-phase
Rated Speed	2480 RPM
Rated Torque (Nom. / Max.)	20 Nm / 43Nm
DC Bus Voltage	270 V
Rated Current (Nom./Max.)	23 A / 45 A
Slot/Pole number	36/42
Single conductor/Copper diameter	0.5055/0.4547 mm
Copper Fill factor	0.6083
Duty-cycle modes (IEC Standard)	S1, S2, S3, S9, S10
Winding Configuration	Centralized
Armature Diameter	137.6 mm
Average length per turn	120 mm
Insulation class	F

After introducing the temperature sensor layout and BPMOR EM specifications used for thermal experiments, the overall multi-sensor test rig schematic design (Figure 6.8) and photos (Figure 6.9) are presented.

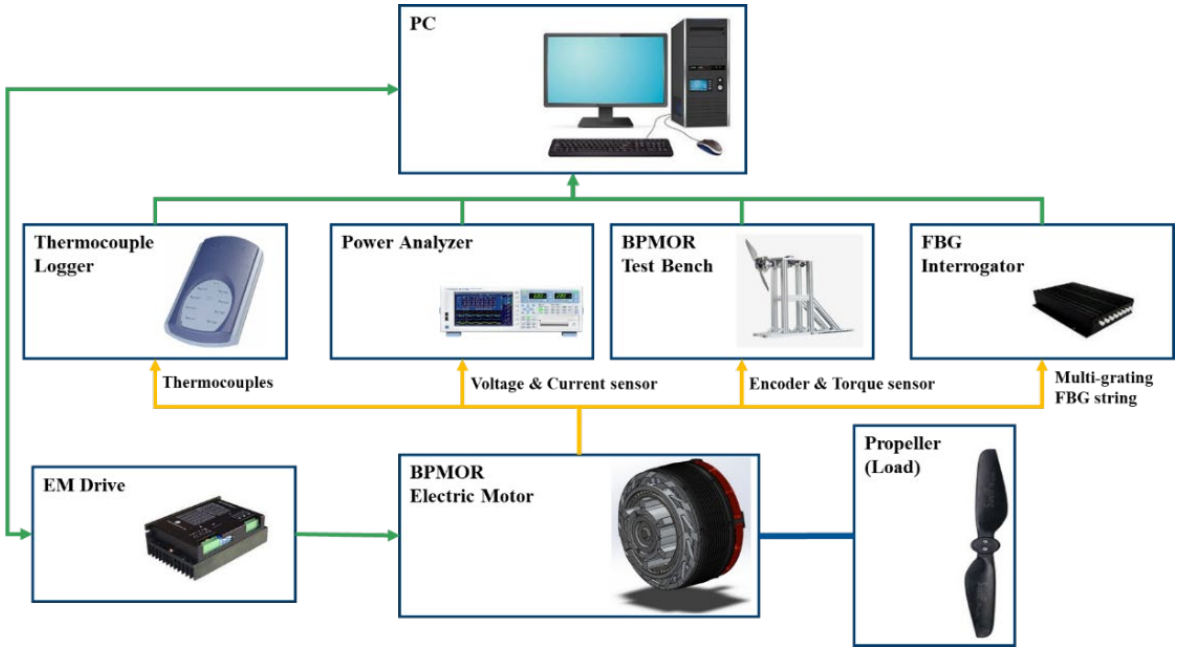

Figure 6.8. Schematic of overall multi-sensor test rig for EM thermal monitoring. The raw data of multiple EM physical parameters will be captured and transmitted to PC by multi-sensors for the full dataset collection for ML temperature prediction model construction.

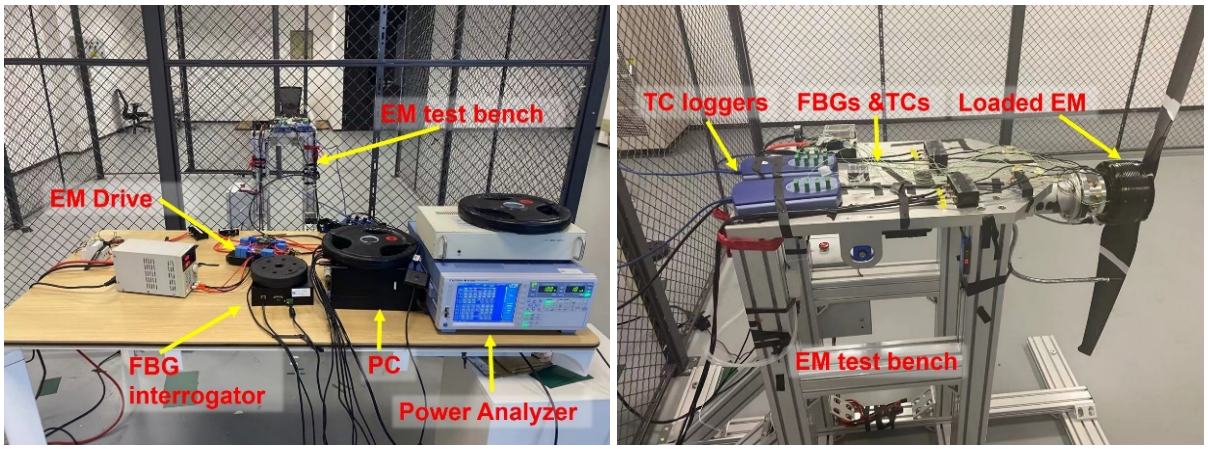

Figure 6.9. Photos of constructed EM multi-sensors test rig, including FBG & thermocouple sensor systems, EM controller, PC, power analyzer (Yokogawa WT1806E) & EM test bench (LYFH LY-70KGF) with torque and rotating speed sensors installed.

Now we may briefly conclude the overall process of how this EM winding thermal sensing system works shown in Figure 6.10: First of all, for the consideration for constructing full-size database, 8 TCs and 8-gratings FBG string were embedded within EM windings. FBG string was wound on the surface while the TCs were buried in the middle of centralized winding for comprehensive data collection (Figure 6.7). Then, during the multiple duty modes thermal experiments of EM, collected all the data including optical spectral, electrical, mechanical and thermal by the multi-sensor test rig. Based on the database above, applying data preprocess and dataset separation for ML models construction.

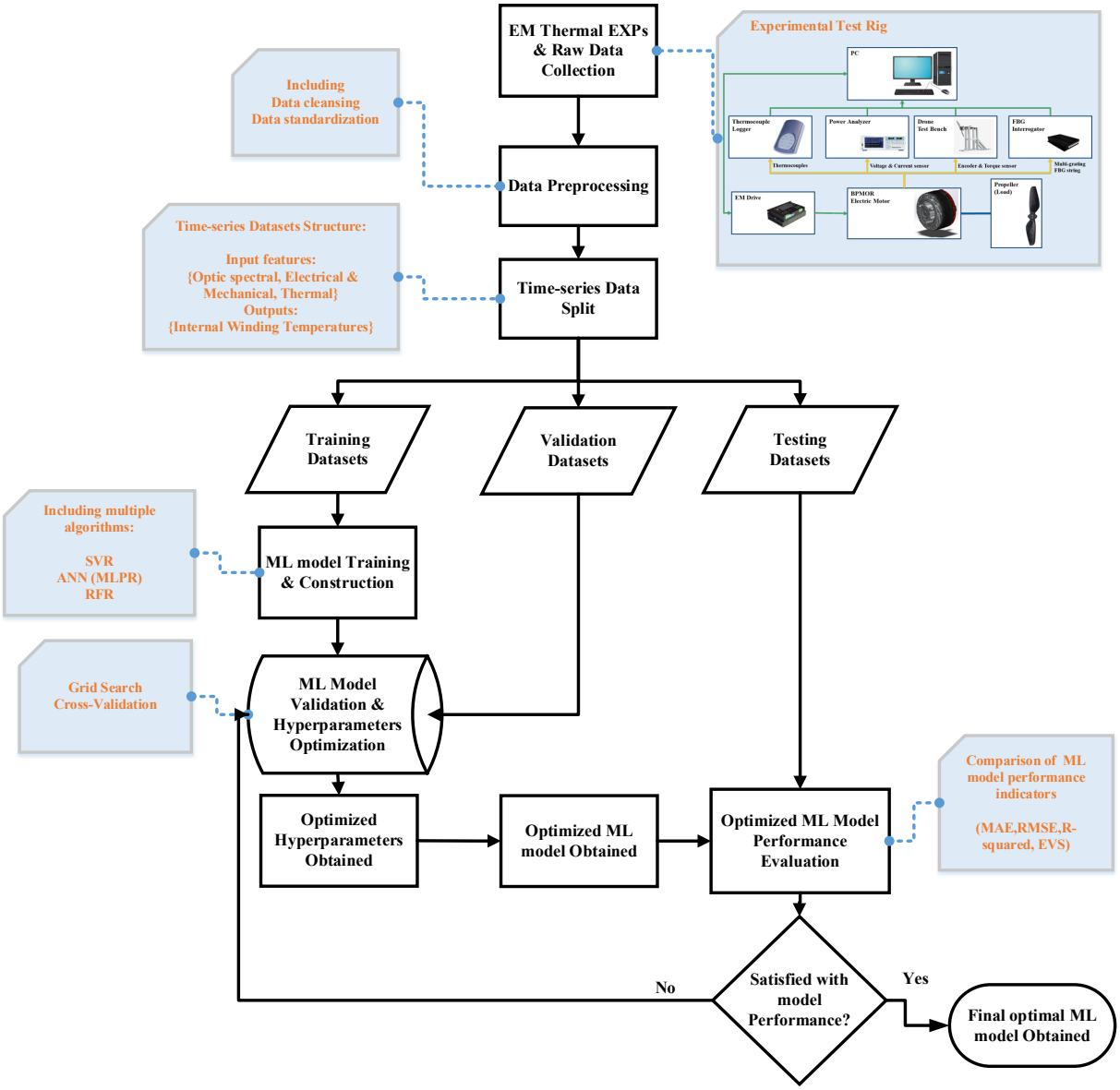

Figure 6.10. Overall optimized multi-source fusion sensor system for EM winding internal temperature monitoring. Specific methods or tools for each step were labelled in orange colour and details will be explained in the following sections.

Five typical duty modes (S1, S2, S3, S9, and S10) of rotating EM operations were chosen, and the corresponding thermal experiments were conducted for overall data collection as we planned in

previous section. The above five EM duty modes were chosen since they cover all the operation categories of EM [166]: continuous running duty (S1), short-time duty (S2), periodic duty (S3~S8), non-periodic duty (S9) and discrete constant loads duty (S10). As shown in Figure 6.10, the overall raw data obtained from multi-sensor system we constructed in advance were recorded with different types of EM duty cycle thermal experiments. The data pre-processing methods were applied to the sequential raw data for ML model datasets construction, including raw sensing data cleansing/smoothing, and feature data standardization. Then the 'clean data' was separated into training, validation and testing datasets using time series data split method for ML model construction. Three types of ML algorithms were employed for the performance comparison of our EM internal winding temperature prediction task. Finally, the overall prediction performance of ML models was analysed in terms of both ML algorithm types and EM operation duty modes. The detailed source code of ML models can be checked in *Appendix-2. Scikit learn code for multi-position inner winding temperature prediction.*

6.1.4 Data pre-processing

6.1.4.1 Data cleansing

In this application for EM winding temperature prediction, a method called exponential smoothing (ES) will be used for the first step of data cleansing, it was employed against the natural intrinsic noises introduced by our different types of raw data collection devices, including the FBG interrogator, torque/speed sensors of motor test bench, and power analyzer. Among the international duty cycles of rotating electric machines (S1-S10) [166], we chose S1, S2, S3, S9 and S10 as target EM operation modes to train and test our temperature prediction models with various regression algorithms.

The data cleansing tool we employed in our project is “tsmoothie”, a python library for time-series smoothing and outlier detection in a vectorized way [186]. All categories of input features (electrical, mechanical and FBG spectral) in time series will be fed into the “ExponentialSmoother” function of tsmoothie lib. This function will provide vectorization to all time-series data input at first, then operates convolutions of fixed dimensions on series using weighted window and computing in an exponential way. This data smoothing method is suitable for our sequential thermal prediction task with non-linear data existed both within input features and outputs. The sampling rate of all data types was set as 1Hz during our thermal experiments. The data cleansing results of different EM duty modes were shown below (Figure 6.15, Figure 6.16).

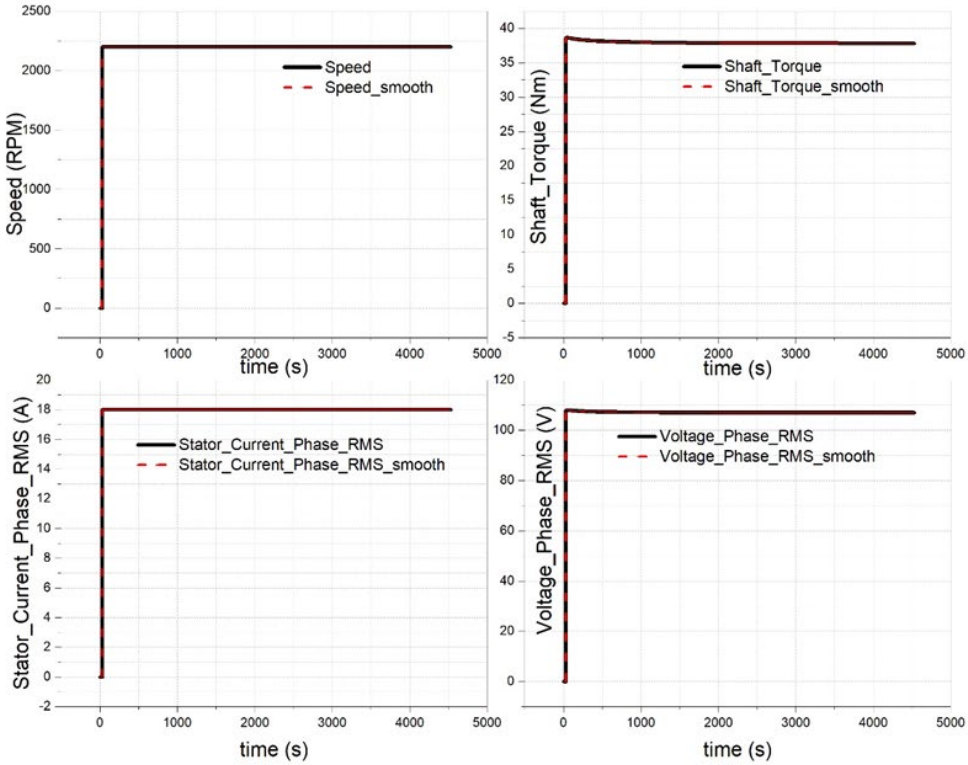

Figure 6.11. S1-Electrical (Current & voltage) and mechanical (rotating speed & torque) features time-series raw data cleansing using "tsmoothie ExponentialSmoother", the solid black curves represent the raw data collected from corresponding sensors while the dash red curves are the data after cleansing. The sampling rates are all 1Hz.

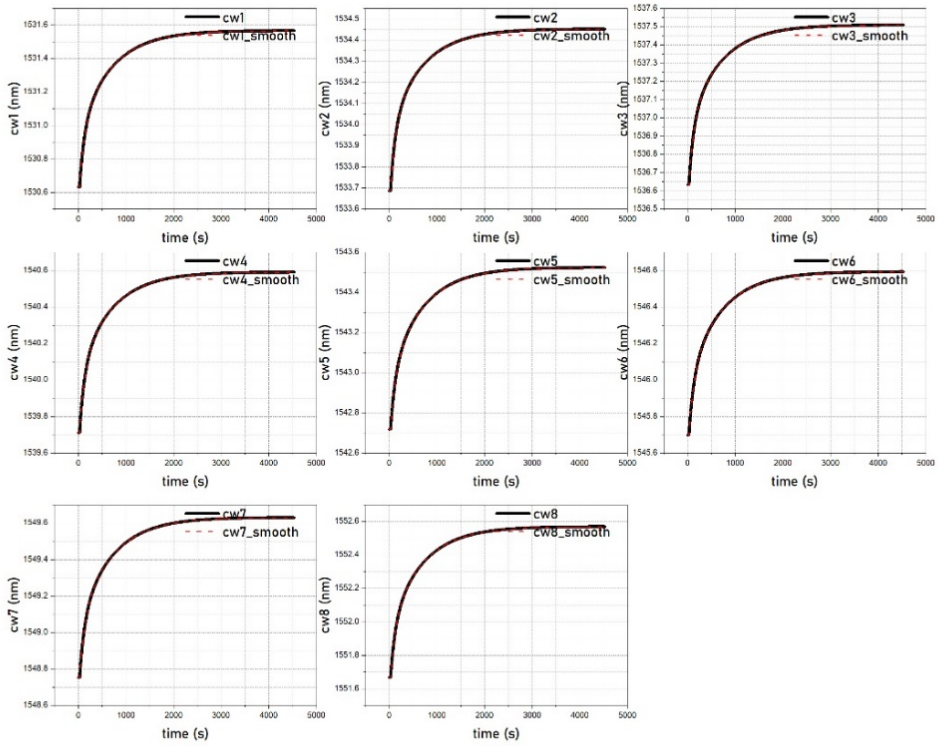

Figure 6.12. S1-FBG optical spectral features (FBG central wavelengths) time-series raw data cleansing using "tsmoothie ExponentialSmoother", the solid black curves represent the raw data collected from FBG interrogator while the dash red curves are the data after cleansing. The sampling rate is 1Hz.

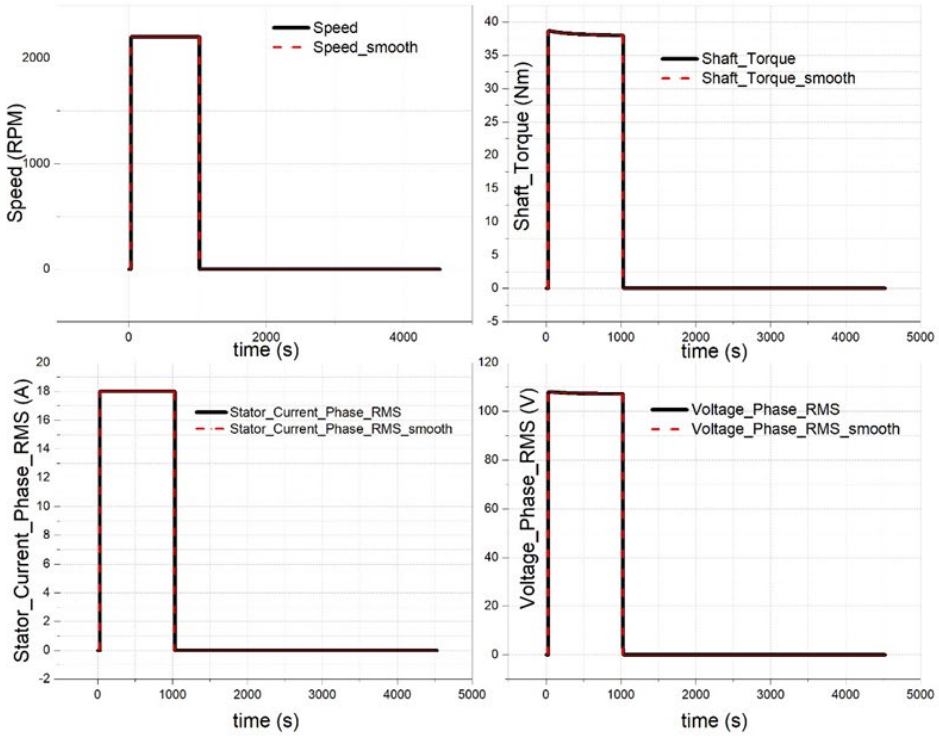

Figure 6.13. S2-Electrical (Current & voltage) and mechanical (rotating speed & torque) features time-series raw data cleansing using "tsmoothie ExponentialSmoother", the solid black curves represent the raw data collected from corresponding sensors while the dash red curves are the data after cleansing. The sampling rates are all 1Hz.

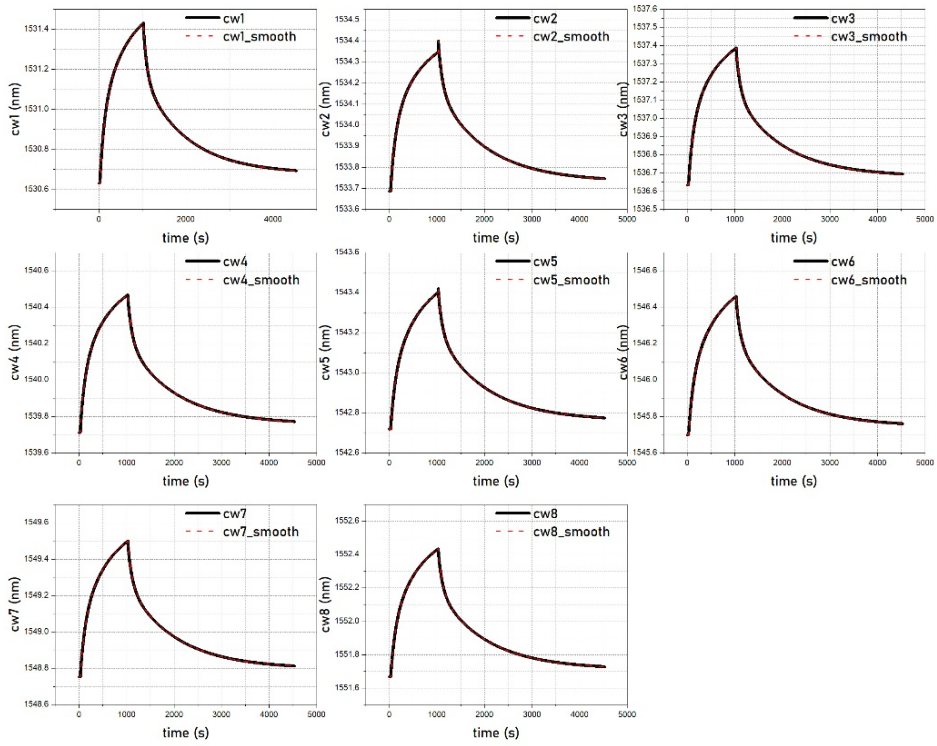

Figure 6.14. S2-FBG optical spectral features (FBG central wavelengths) time-series raw data cleansing using "tsmoothie ExponentialSmoother", the solid black curves represent the raw data collected from FBG interrogator while the dash red curves are the data after cleansing. The sampling rate is 1Hz.

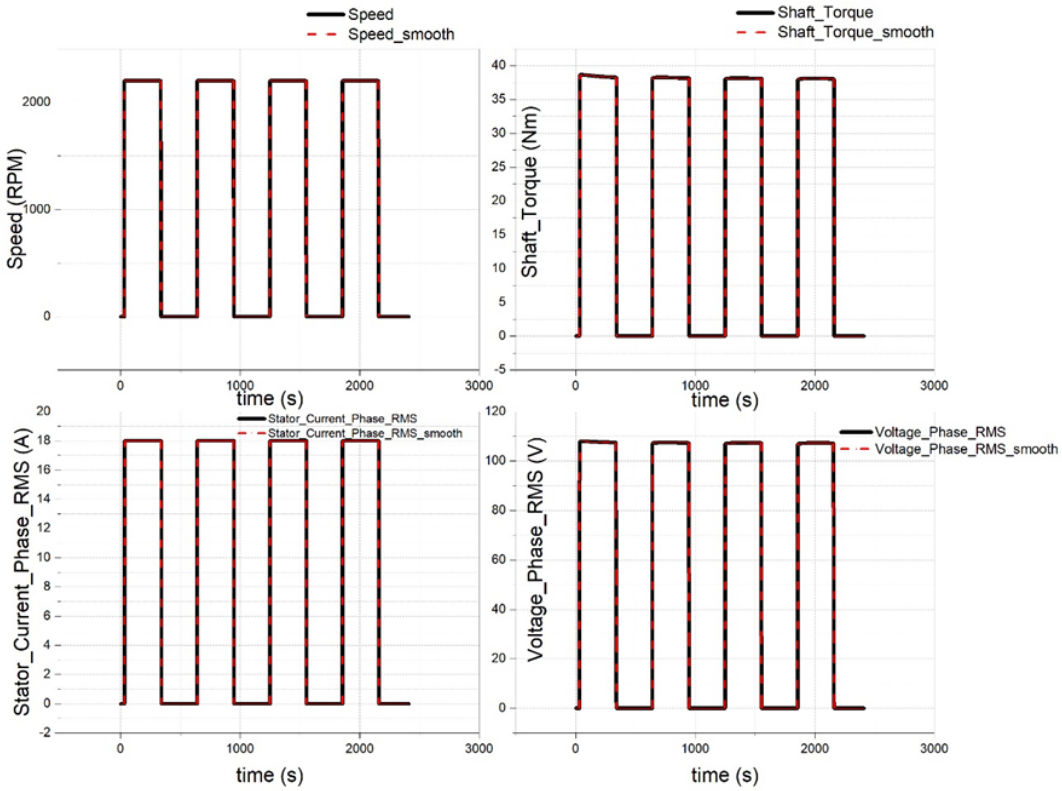

Figure 6.15. S3-Electrical (Current & voltage) and mechanical (rotating speed & torque) features time-series raw data cleansing using "tsmoothie ExponentialSmoother", the solid black curves represent the raw data collected from corresponding sensors while the dash red curves are the data after cleansing. The sampling rates are all 1Hz.

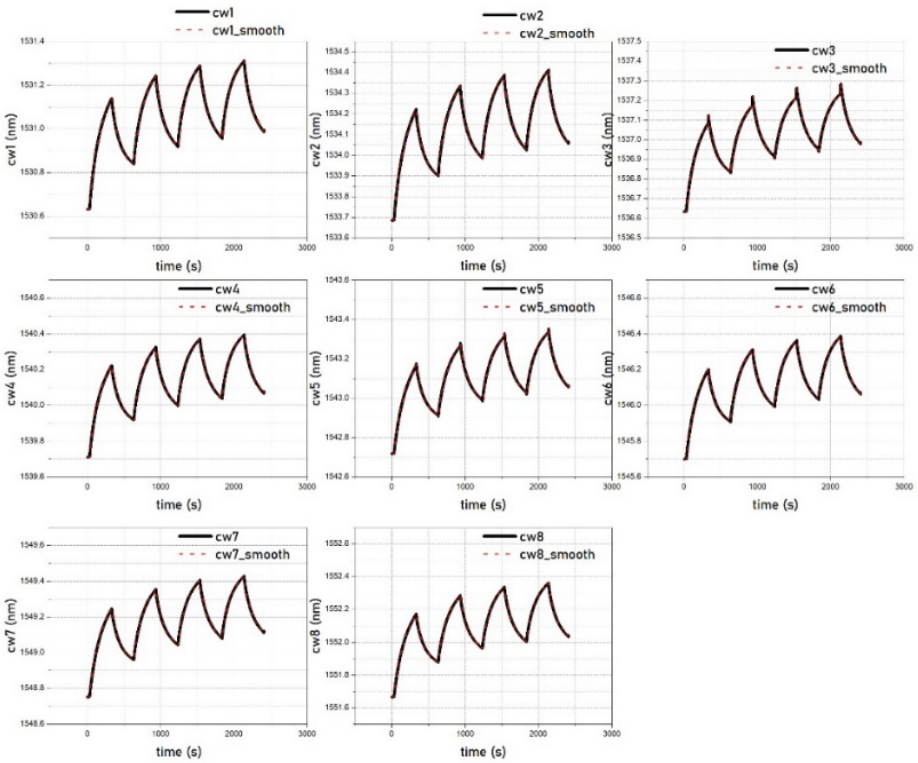

Figure 6.16. S3-FBG optical spectral features (FBG central wavelengths) time-series raw data cleansing using "tsmoothie ExponentialSmoother", the solid black curves represent the raw data collected from FBG interrogator while the dash red curves are the data after cleansing. The sampling rate is 1Hz.

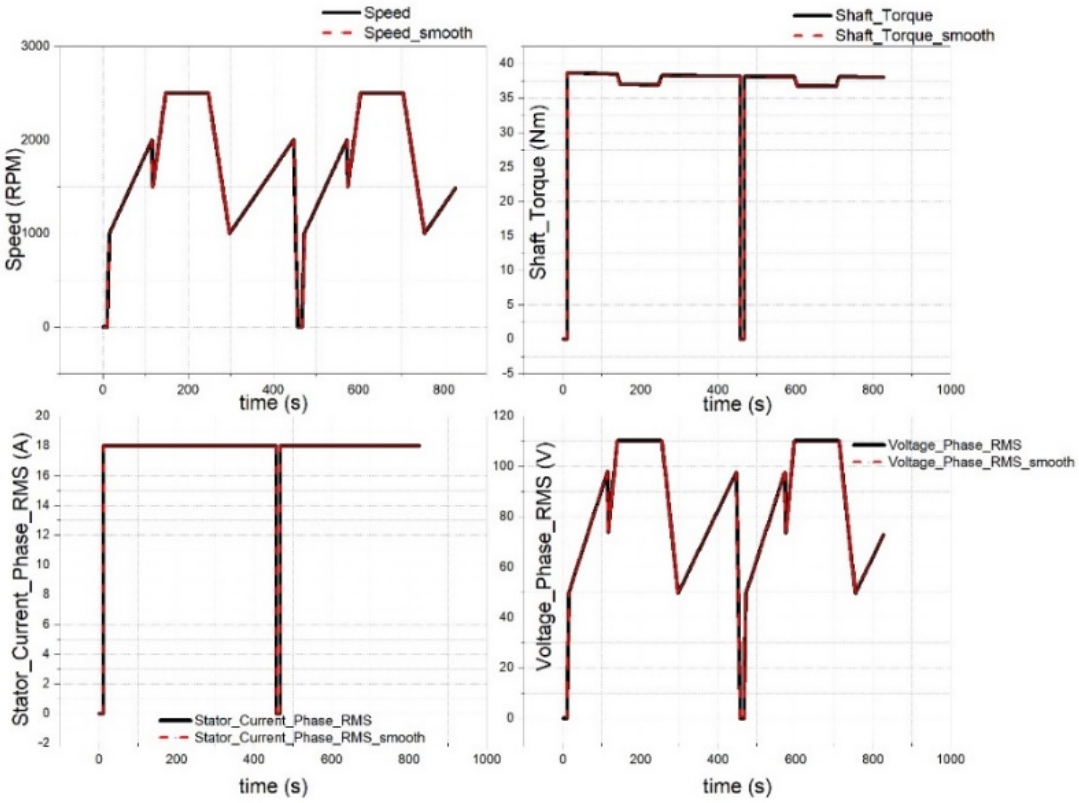

Figure 6.17. S9-Electrical (Current & voltage) and mechanical (rotating speed & torque) features time-series raw data cleansing using "tsmoothie ExponentialSmoother", the solid black curves represent the raw data collected from corresponding sensors while the dash red curves are the data after cleansing. The sampling rates are all 1Hz. Such non-periodic duty mode is self-designed.

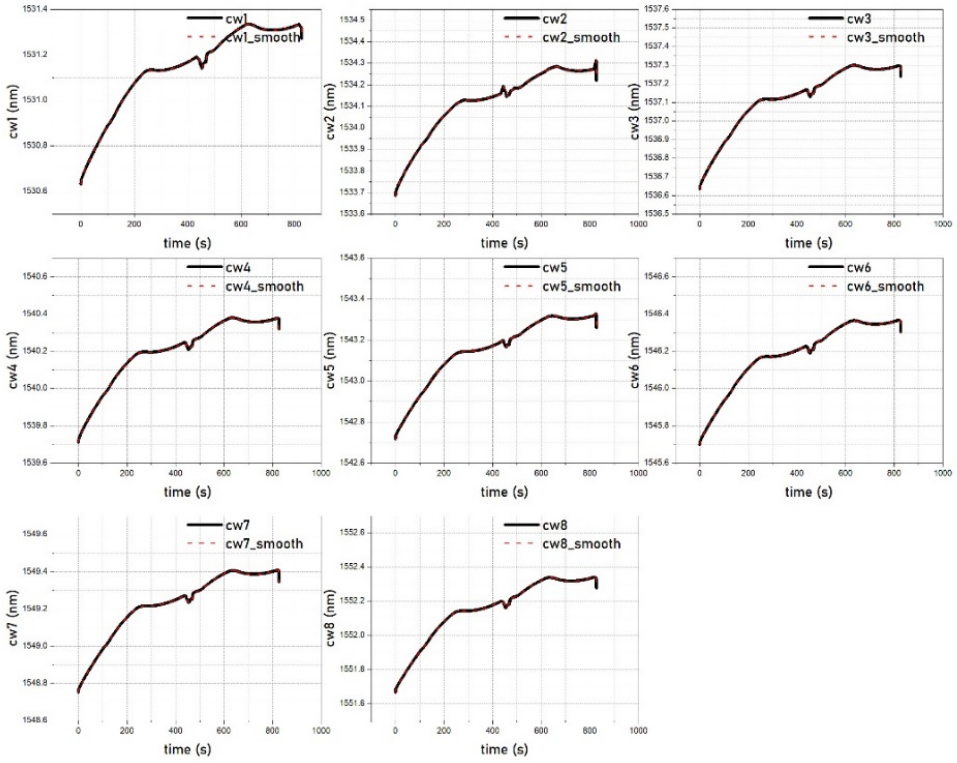

Figure 6.18. S9-FBG optical spectral features (FBG central wavelengths) time-series raw data cleansing using "tsmoothie ExponentialSmoother", the solid black curves represent the raw data collected from FBG interrogator while the dash red curves are the data after cleansing. The sampling rate is 1Hz.

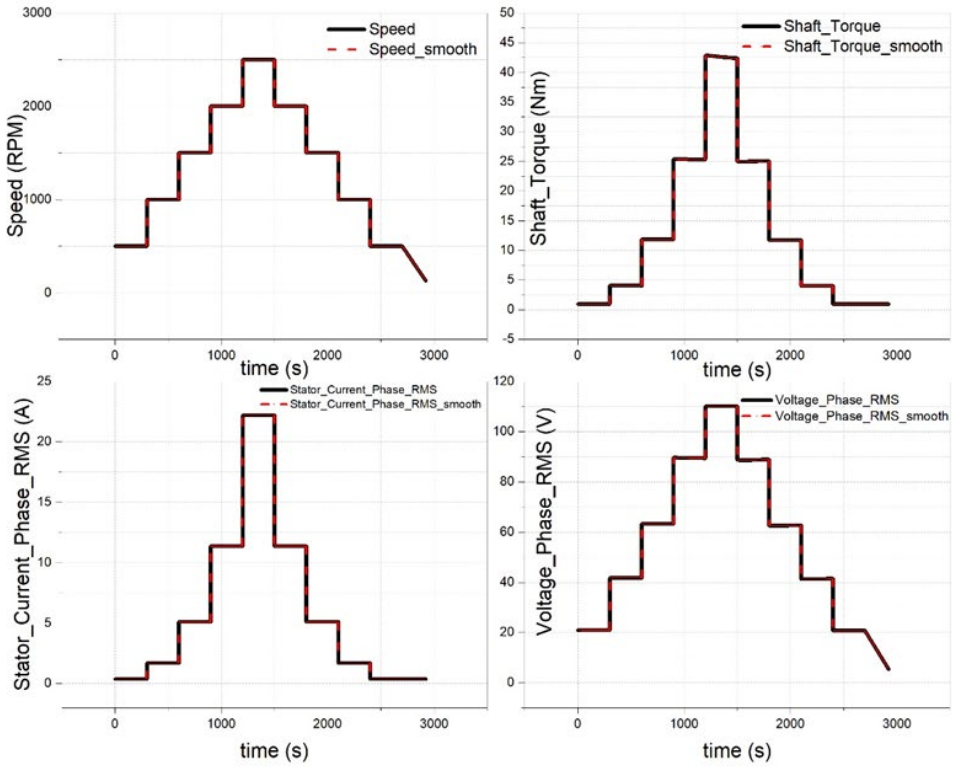

Figure 6.19. S10-Electrical (Current & voltage) and mechanical (rotating speed & torque) features time-series raw data cleansing using "tsmoothie ExponentialSmoother", the solid black curves represent the raw data collected from corresponding sensors while the dash red curves are the data after cleansing. The sampling rates are all 1Hz.

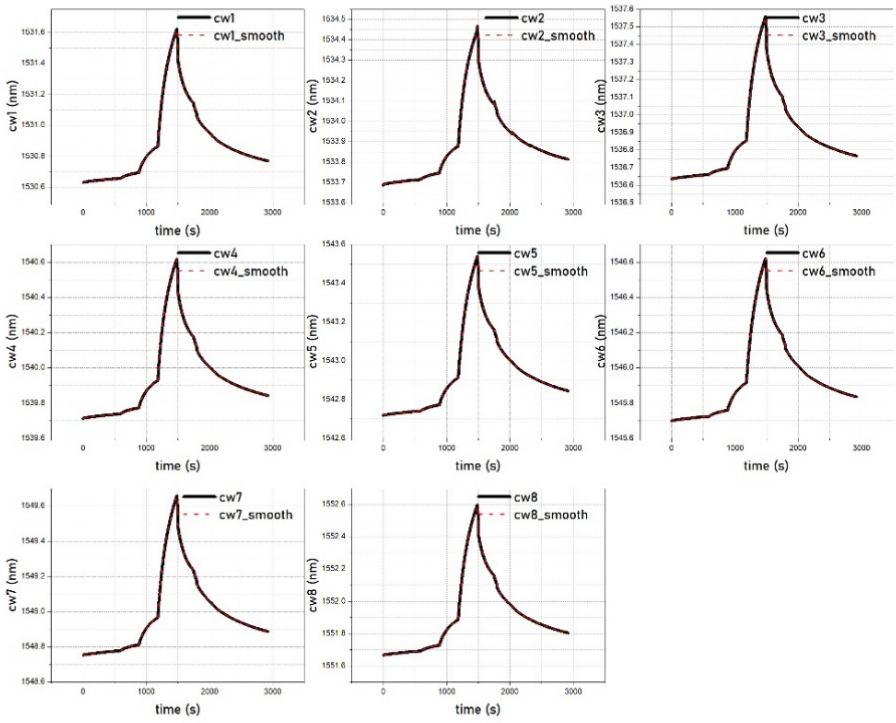

Figure 6.20. S10-FBG optical spectral features (FBG central wavelengths) time-series raw data cleansing using "tsmoothie ExponentialSmoother", the solid black curves represent the raw data collected from FBG interrogator while the dash red curves are the data after cleansing. The sampling rate is 1Hz.

It can be observed in plots from Figure 6.11 to Figure 6.20, the effects of data cleansing were not intuitively presented in figures. It can be explained from the plots of raw data: we found that the intrinsic noises in our experimental raw data were relatively low, which credited to the good quality of sensor hardware. However, for the robustness of overall design process of our FBG-ML combined intelligent thermal monitoring system, the data cleansing step must be considered in

advance so that we can deal with the conditions if noisy feature data occurs in future cases.

6.1.4.2 Data standardization

We have multi-dimensional input features in various scales for our EM winding temperature prediction task. The advanced data standardization step will be required. The aim of this step is to improve the 1) convergence rate and 2) prediction accuracy of our trained ML models. The mathematic formula for 'z-score' standardization method is shown in equation (6.22):

$$x_i^{std} = \frac{x_i - \bar{x}}{\sigma}, \qquad where\ \sigma = \sqrt{\frac{1}{n-1}\sum_{i=1}^{n}(x_i - \bar{x})^2} \tag{6.22}$$

Where $\boldsymbol{x_i}$ is the original feature data, $\overline{\boldsymbol{x}}$ is the mean value of corresponding feature data, and $\boldsymbol{\sigma}$ is the standard deviation corresponding feature data.

The formula above will be applied to all types of sequential input features shown in Figure *6.1*. After comparing the ML model training speed of using 1) original feature data in multi-scales $\boldsymbol{x_i}$, and 2) standardized feature data$\boldsymbol{x_i^{std}}$, we found that such standardization method would also dramatically improve the training speed of ML model construction (i.e. reduce the ML model construction time consumption). Therefore, the feature data standardization is considered as the compulsory data preprocessing method in our EM temperature prediction application.

6.1.4.3 Training data set separation method: Time series dataset split

Since the clean and standardized data were obtained, data split for three categories datasets preparation (training, validation and testing datasets) need to be considered for ML model

construction. For time series datasets within this EM winding temperature prediction scenario, the datasets separation cannot be achieved by random train-test split as carried out in general regression ML tasks. Common cross validation methods, including K-Fold or Shuffle cannot be applied due to the time sequence problems, which may cause the problems of time-series features crossover. For instance, the future feature/output combination may be used to predict past data. Such cross-validation results shall make no sense for our target industrial temperature prediction scenario and can easily cause overfitting/underfitting problems of ML models. In order to solve the prediction problem of time series datasets, time series cross validation method (Figure 6.21) was employed in this research.

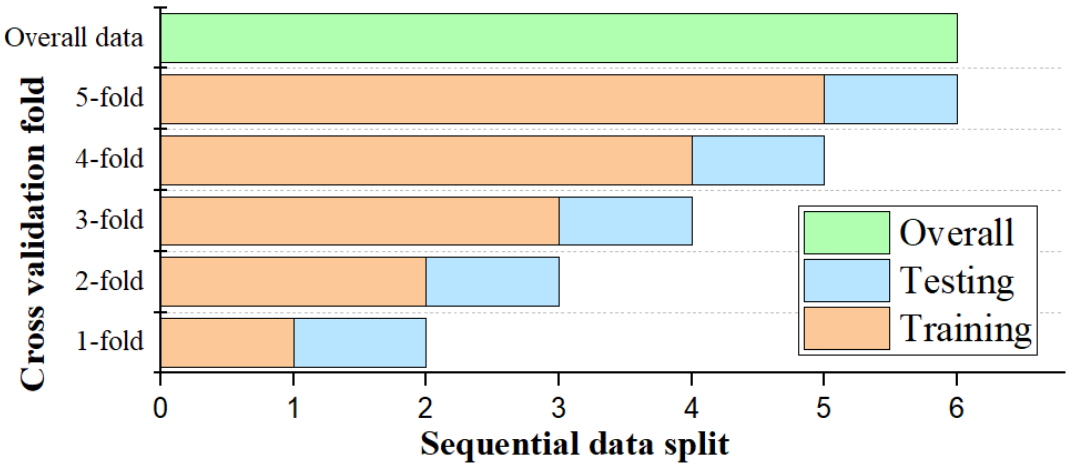

Figure 6.21. Demonstration of time series dataset split method for time-series regression problem [187]*, it adopts the strategy of forward chaining, i.e. divide each folding dataset in chronological order for ML model training and testing.*

In our case, the S3 duty mode datasets were employed for ML training and validation since the periodic operating mode is considered as the most common duty modes among electrical industry,

also the S3 data covers the thermal characteristics of EM including both "running" and "resting" conditions, which is suitable for ML model to learn how thermal field will distribute within EM windings. The overall data aggregated around 10 hours were recorded with sampling rate at 1 Hz. Therefore, there will be around 30 thousands samples in total, with twenty components each sample. These components include sixteen input features and four target temperature outputs as shown in *Figure 6.1*.

6.2 Multiple duty cycles results

The sequential temperature prediction results of EM under multiple duty-cycle conditions will be presented in this section. The evaluation of ML temperature prediction performance will be presented and compared among different types of ML algorithms (SVR, ANN and RFR).

6.2.1 ML modelling

To find the optimal ML regression model with most satisfied performance, the optimal hyperparameter combination needs to be found for any given specific application. An exhaustive search method over assigned parameter values was employed in this application called grid search cross validation. The range of hyperparameters to be validated exhaustively and the optimized values in this winding thermal monitoring application are shown in Table 6.3. The construction of our ML models was based on "Scikit-Learn" open access Python machine leaning development environment [173]. The range of all hyperparameters for three types of ML models were chosen manually for grid-search ML model optimization and model converge. The range of hyperparameters were given based on the characteristics of our EM thermal monitoring application. (i.e. small sample size, non-large input feature dimension, time-series prediction scenario). $\boldsymbol{R^2}$

(Coefficient of determination) was employed as regression score function for best hyperparameter combination selection.

ML optimized model regression performance evaluation

Several regression performance indices (formula 6.23-26) were employed to evaluate the overall performance of winding internal temperatures predictions, with the formulas shown below, where $\boldsymbol{T^i_{measured}}$ were the internal winding temperatures measured by thermocouples during multiple duty cycle thermal experiments and $\boldsymbol{T^i_{predict}}$ were the predicted target temperature values estimated by ML models.

Mean absolute error (MAE):

$$e_{MAE} = \frac{1}{N}\sum_{i=1}^{N}\left|T^i_{measured} - T^i_{predict}\right| \tag{6.23}$$

Root mean squared error (RMSE):

$$e_{RMSE} = \sqrt{\frac{1}{N}\sum_{i=1}^{N}\left(T^i_{measured} - T^i_{predict}\right)^2} \tag{6.24}$$

Coefficient of determination ($\boldsymbol{R^2}$):

$$R^2 = 1 - \frac{\sum_{i=1}^{N}\left(T^i_{measured} - T^i_{predict}\right)^2}{\sum_{i=1}^{N}\left(T^i_{measured} - \bar{T}^i_{measured}\right)^2} \tag{6.25}$$

Explained variance score (EVS):

$$Score_{ev} = 1 - \frac{Variance\left\{T^i_{measured} - T^i_{predict}\right\}}{Variance\left\{T^i_{measured}\right\}} \tag{6.26}$$

$$where\ Variance\{T^i_{measured} - T^i_{predict}\}$$

$$= Variance\{T^i_{measured}\} + Variance\{T^i_{predict}\} - 2\mathrm{Cov}(T^i_{measured}, T^i_{predict})$$

In our EM winding temperature prediction application, the Coefficient of determination ($\boldsymbol{R^2}$) was employed as the prime regression score function for optimal hyperparameter combination selection during the ML model optimization process of our three types of ML algorithms (SVR, ANN, and RFR). Other regression performance indices will also be analysed to give a comprehensive and robust regression performance evaluation of our ML models.

Table 6.3. Hyperparameter range for grid search & optimized values for multiple algorithms in this EM winding temperature monitoring application. To be noticed, the optimal hyperparameter combination would vary with the EM specifications. The values shown in this table was based on the EM specifications shown in Table 6.2.

ML regression algorithms	Hyperparameters	Range	Optimized value
SVR	Kernel functions	RBF, Sigmoid, Polynomial	Sigmoid
	Penalty factor 'C'	[0.1, 0.5, 0.9, 1, 5, 7, 9, 10]	5
	Kernel coefficient 'γ'	[0.001, 0.01, 0.1, 1]	0.01
	Epsilon-insensitive loss coefficient 'ε'	[0.01,0.05.0.1,0.2,0.5]	0.2
	Degree 'd'	[1,2,3,4,5]	3
	Constant term of kernel function 'b_0'	[0,0.5,1, 2, 4, 5]	0
ANN (MLPR)	Number of layers	[1,2,3 … 10]	2
	Number of neurons each layer	[3,4,5 … 30]	7
	Activation functions	identity, logistic, tanh, "ReLU"]	ReLU
	Optimization solvers	L-BFGS, SGD, Adam	Adam
	L2 regularization parameter 'α'	[0.0000005, 0.000005,0.00005,0.0005,0.005,0.05]	0.0005
RFR	Number of trees 'k'	[5, 10, 15 … 200]	10
	Limited max depth of each tree 'dep_max'	[5, 6, 7… 50]	30
	Minimum samples of each leaf	[1, 2, 3 … 20]	6
	Minimum samples for split	[2, 3, 4 … 20]	11

It can be observed from the ML model construction & optimization results shown in Table 6.3, the EM winding temperature prediction task will be completed with a relative shallow ML model structure: SVR is a shallow machine learning algorithm naturally, and deep ANN with more layers and neurons did not present a better temperature prediction, neither for the larger RFR model.

The following sections will present the testing results using the optimised ML models we obtained shown in Table 6.3. The internal winding temperature prediction results will be presented in time series at planned 'even' ex-situ sensor positions in all four different EM testing duty modes (S1, S2, S9 and S10).

6.2.2 ML models performances on multiple EM duty-cycles

ML models for EM internal winding temperature prediction: Continuous running duty S1

In this section, the ML model testing results of S1 (continuous running duty) EM duty mode will be presented by time-series plots. In addition, the regression performance comparison based on the types of ML algorithms will be analysed using four statistical regression performance indicators.

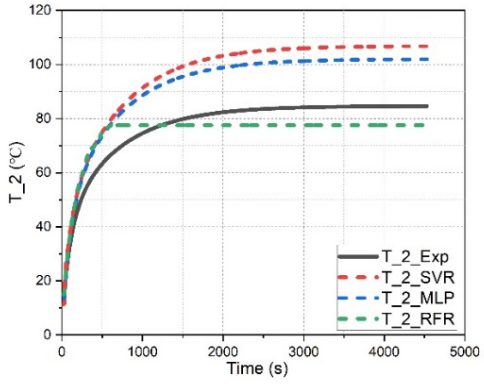

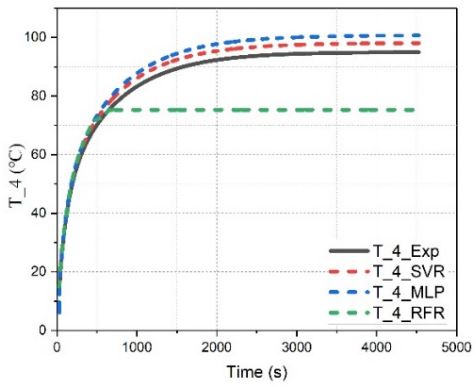

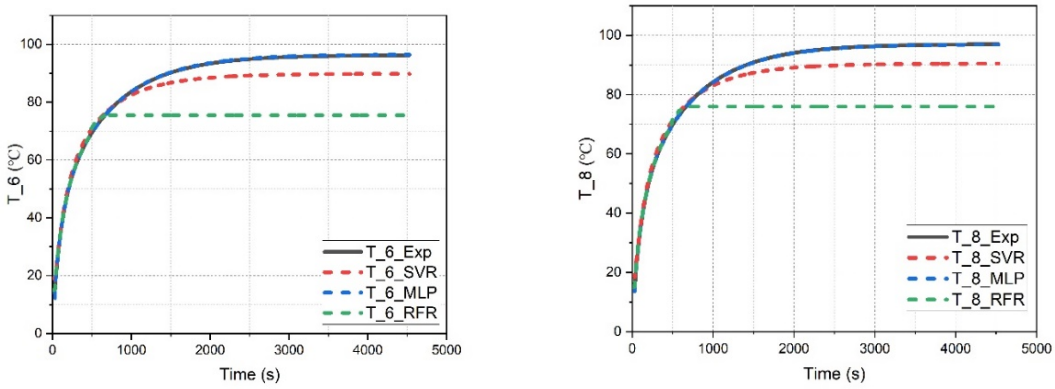

Figure 6.22. EM winding internal temperatures at "even" positions-ML models testing results of S1 duty mode: temperature outputs of ML models are shown in curves T_2, T_4, T_6, and T_8 with different ML algorithm type labelled, while the experimental results measured by implemented thermocouples inside EM windings are shown in T_Exp with corresponding positions labelled.

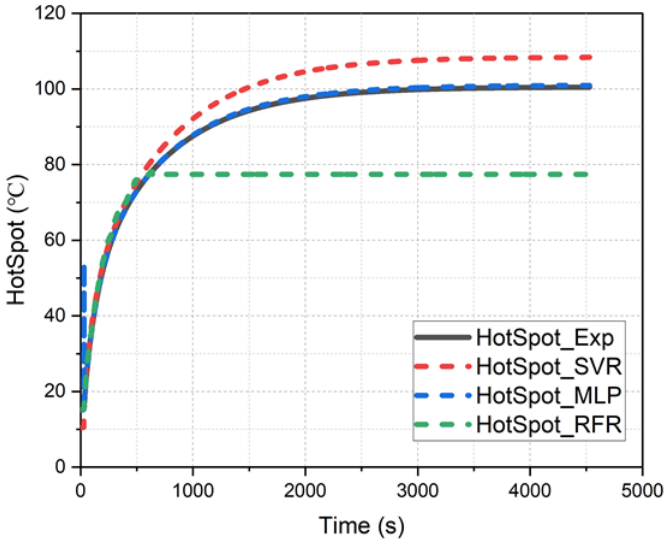

Figure 6.23. EM winding internal Hot-spot temperature-ML models testing results of S1 duty mode: temperature outputs of ML models are shown in curves HotSpot with different ML algorithm type

labelled, while the experimental results measured by implemented thermocouples inside EM windings are shown in HotSpot_Exp, which was obtained by applying a simple maximum value filtering within all 8 thermocouples measurements results.

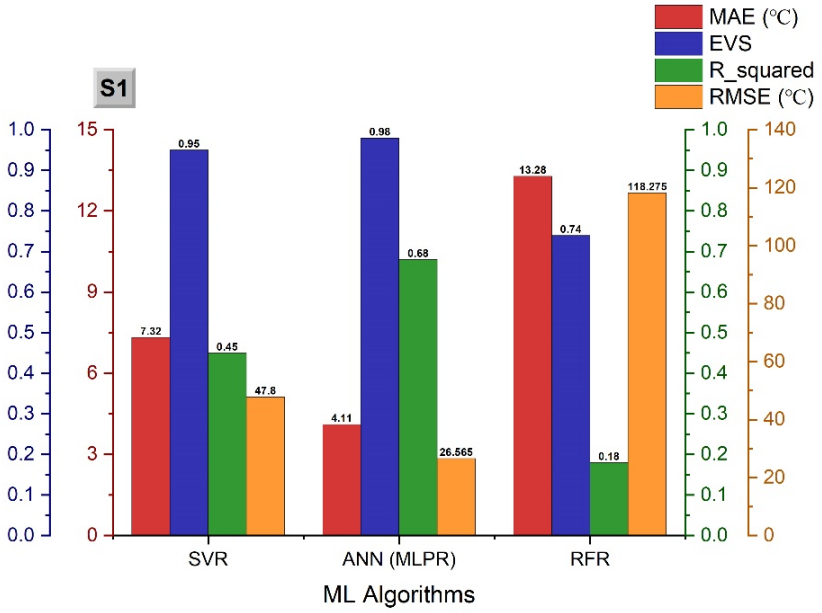

Figure 6.24. ML models regression performance (for S1) comparison based on the algorithm types.

By comparing the time-series temperature plots as well as the regression performance indices, we found that ANN presented the best temperature prediction performance with high scores and low errors. SVR and RFR models had poor estimation of final, stable temperature estimation compared to the ANN model. However, ANN model had outlier temperature outputs in both T_4 and HotSpot curves while the EM continuous running operation started at the very beginning stage. Such wrong predictions were avoid by SVR and RFR models, which indicated they were relatively robust to the dramatic variation of input features. Even considering the strong outlier effects to the MAE and RMSE indicators, ANN still presented the best regression performance for EM S1 duty mode.

ML models for EM internal winding temperature prediction: Short-time duty S2

In this section, the ML model testing results of S2 (Short-time duty) EM duty mode will be presented by time-series plots. In addition, the regression performance comparison based on the types of ML algorithms will be analysed using four statistical regression performance indicators.

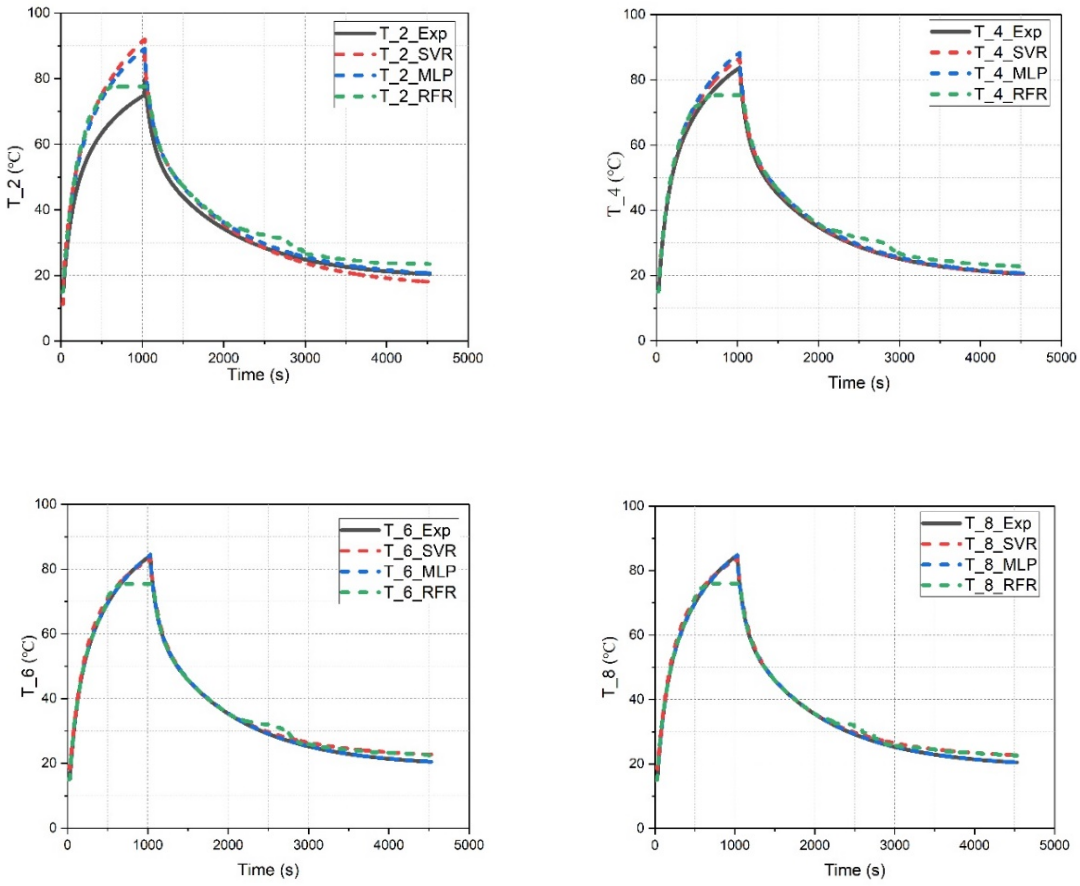

Figure 6.25. EM winding internal temperatures at "even" positions-ML models testing results of S2 duty mode: temperature outputs of ML models are shown in curves T_2, T_4, T_6, and T_8 with different ML algorithm type labelled, while the experimental results measured by implemented thermocouples inside EM windings are shown in T_Exp with corresponding positions labelled.

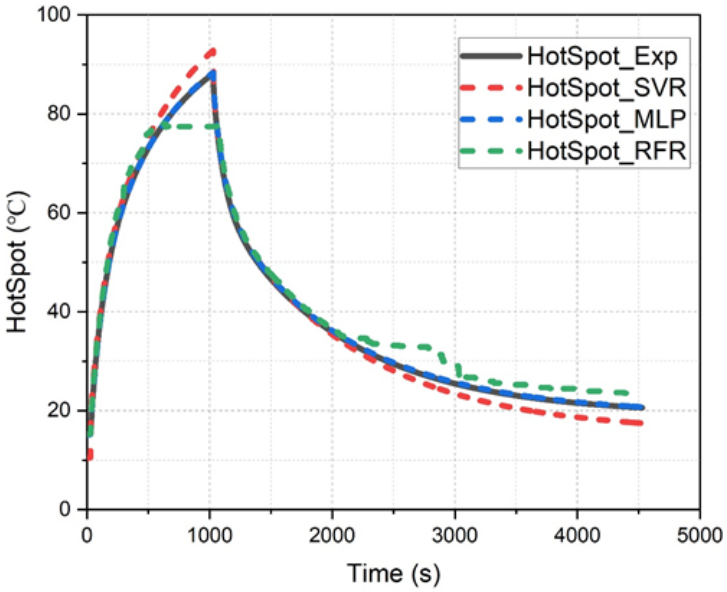

Figure 6.26. EM winding internal Hot-spot temperature-ML models testing results of S2 duty mode: temperature outputs of ML models are shown in curves HotSpot with different ML algorithm type labelled, while the experimental results measured by implemented thermocouples inside EM windings are shown in HotSpot_Exp, which was obtained by all thermocouples measurements maximum value filtering.

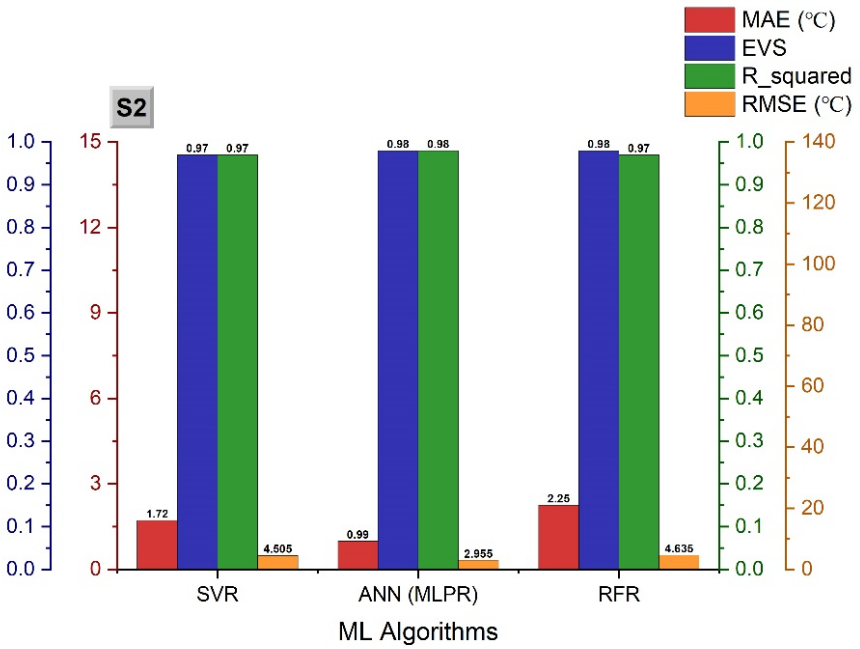

Figure 6.27. ML models regression performance (for S2) comparison based on the algorithm types.

We found that similar temperature prediction results of S1 has been presented in S2 mode. Since no outlier values occur within the ML model prediction results, the errors of all types of algorithms were smaller than those of S1 results. Both SVR and ANN models showed good performance for S2 duty mode, while RFR model still had the wrong estimation of peak temperature values.

ML models for EM internal winding temperature prediction: Non-periodic duty S9

In this section, the ML model testing results of S9 (Non-periodic duty) EM duty mode will be presented by time-series plots. In addition, the regression performance comparison based on the types of ML algorithms will be analysed using four statistical regression performance indicators.

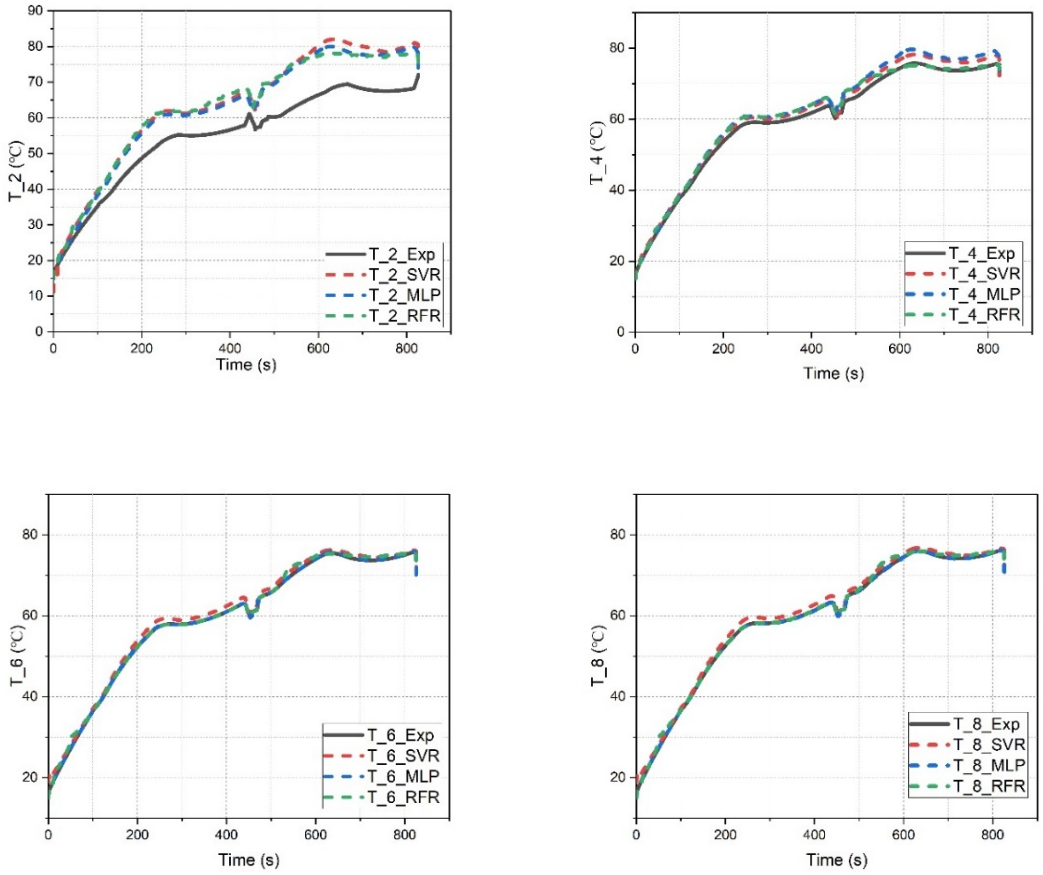

Figure 6.28. EM winding internal temperatures at "even" positions-ML models testing results of S9 duty mode: temperature outputs of ML models are shown in curves T_2, T_4, T_6, and T_8 with different ML algorithm type labelled, while the experimental results measured by implemented thermocouples inside EM windings are shown in T_Exp with corresponding positions labelled.

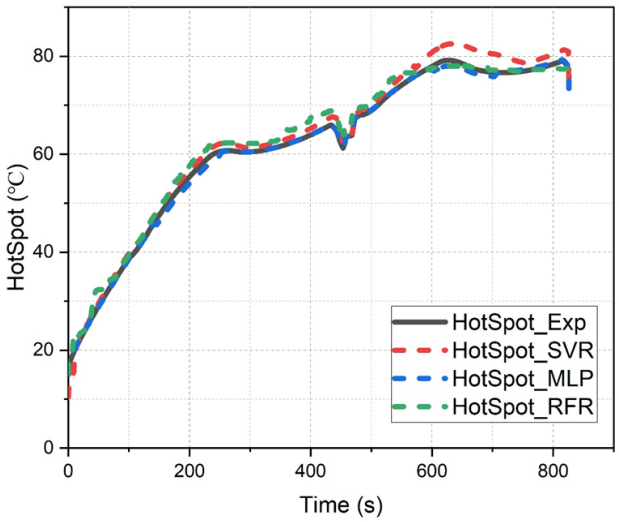

Figure 6.29. EM winding internal Hot-spot temperature-ML models testing results of S9 duty mode: temperature outputs of ML models are shown in curves HotSpot with different ML algorithm type labelled, while the experimental results measured by implemented thermocouples inside EM windings are shown in HotSpot_Exp, which was obtained by all thermocouples measurements maximum value filtering.

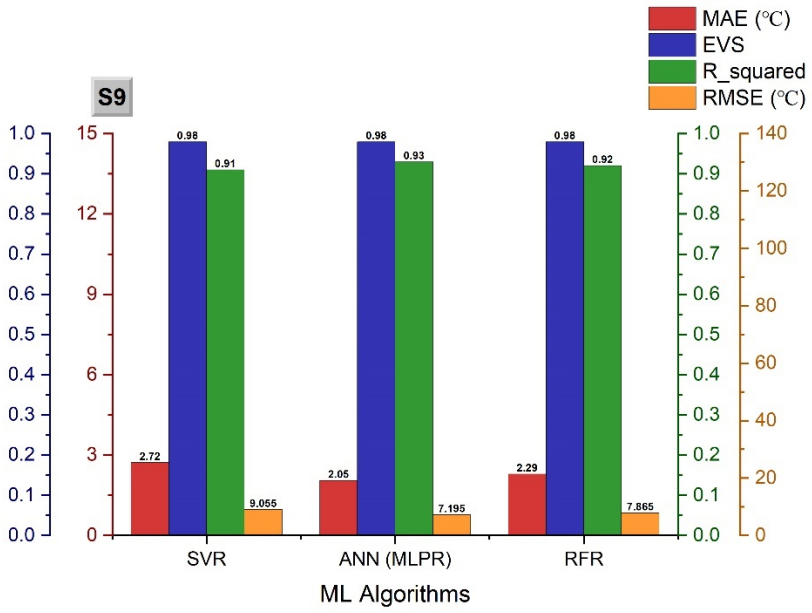

Figure 6.30. ML models regression performance (for S9) comparison based on the algorithm types.

All types of ML algorithms presented acceptable temperature distribution results in the non-periodic duty mode S9. This a very important break point, which proved the good generalization ability of our ML models. ANN presented the best performance among the three algorithms. Additionally, an interesting phenomenon was plotted in the curve of T_2, which represents the temperature record of position 2 within winding. All three ML models give the opposite temperature trend compared to the experimental results. If we checked temperature trends in position 4, 6, and 8, we found that they all presented the same trend as the ML models predicted at position 2. In practice, the temperature variation trend of different positions on same winding will be same, even if temperature difference existed. Therefore, according to the majority principle, we just assumed that the ML models presented the right temperature trend at position 2 of winding. Such result indicated that our ML models were able to understand the effects of input features on thermal distribution and made right temperature predictions as the compensation for random

sensor failure.

ML models for EM internal winding temperature prediction: Discrete Constant Loads duty S10

In this section, the ML model testing results of S10 (Discrete Constant Loads duty) EM duty mode will be presented by time-series plots. In addition, the regression performance comparison based on the types of ML algorithms will be analysed using four statistical regression performance indicators.

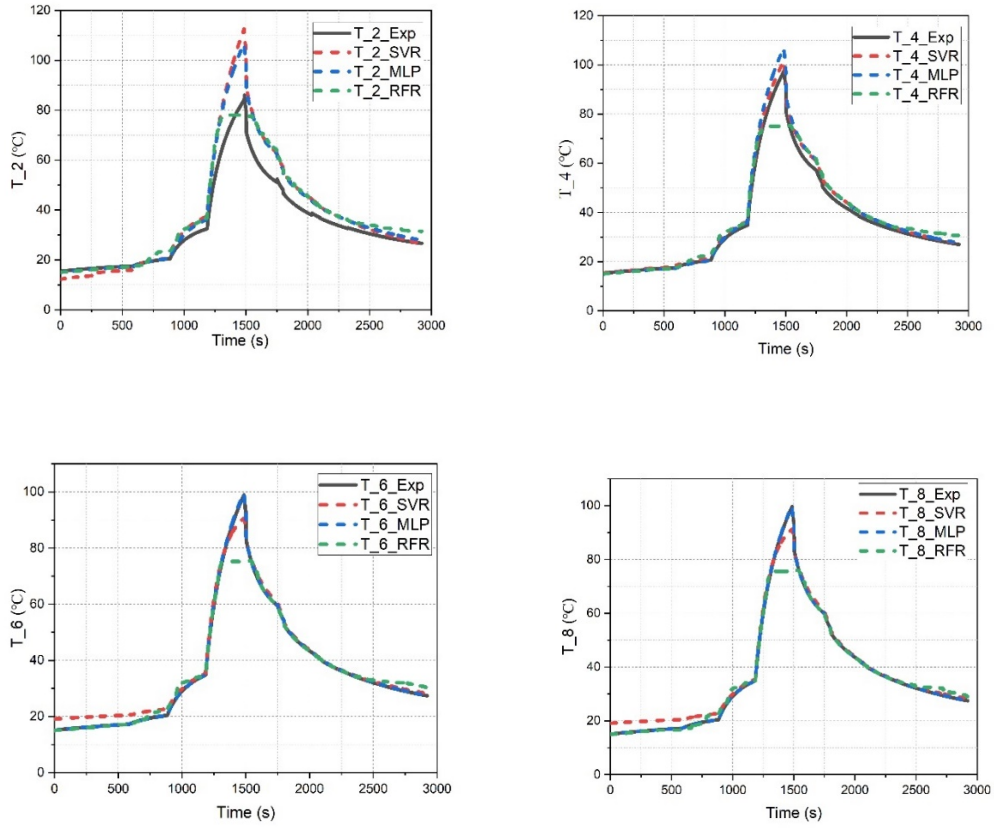

Figure 6.31. EM winding internal temperatures at "even" positions-ML models testing results of

S10 duty mode: temperature outputs of ML models are shown in curves T_2, T_4, T_6, and T_8 with different ML algorithm type labelled, while the experimental results measured by implemented thermocouples inside EM windings are shown in T_Exp with corresponding positions labelled.

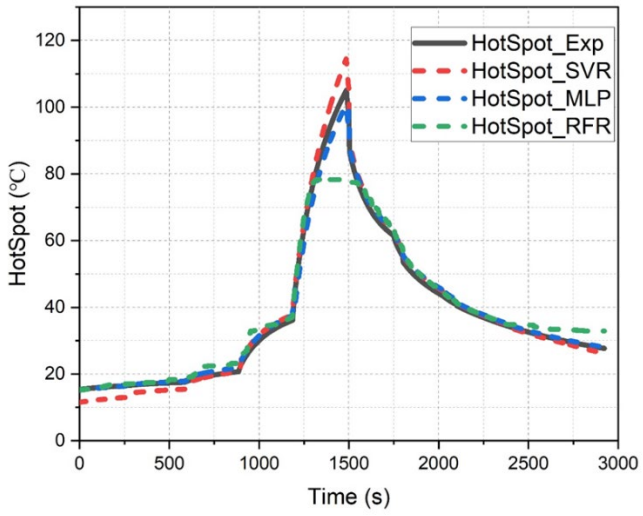

Figure 6.32. EM winding internal Hot-spot temperature-ML models testing results of S10 duty mode: temperature outputs of ML models are shown in curves HotSpot with different ML algorithm type labelled, while the experimental results measured by implemented thermocouples inside EM windings are shown in HotSpot_Exp, which was obtained by all thermocouples measurements maximum value filtering.

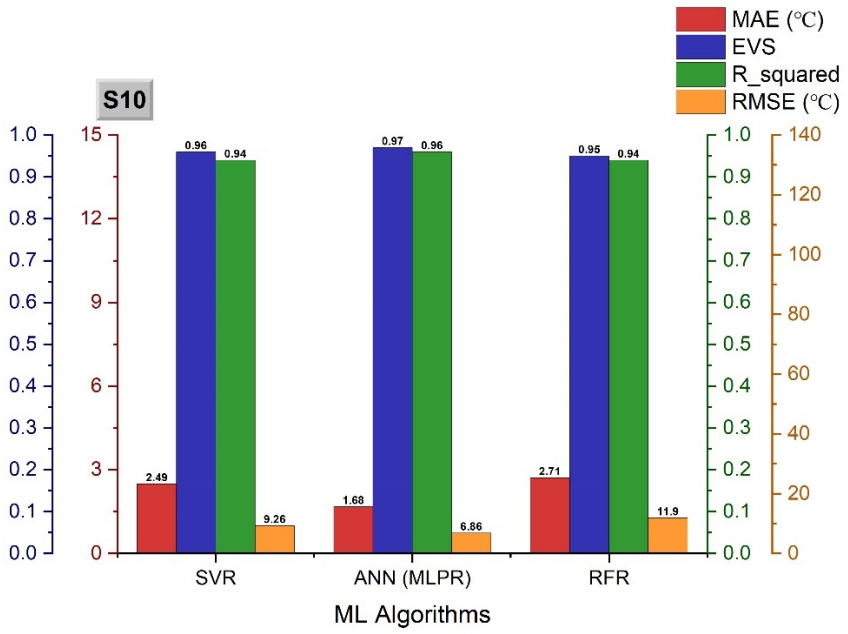

Figure 6.33. ML models regression performance (for S10) comparison based on the algorithm types.

In S10 duty mode, we found that both SVR and ANN models presented acceptable temperature prediction results over the target positions within EM windings. RFR still presented unsatisfied temperature estimation on the peak temperature values.

6.2.3 Discussions & Performance comparisons

It can be observed from the analysis and discussion of ML model prediction performances:

1) There are temperature differences among different positions inside EM windings. Therefore, the failure potential of overheating has been proven and the comprehensive thermal monitoring is necessary for the safety of EM operation.
2) Both SVR and ANN algorithm-based models presented good temperature prediction accuracy

and good generalization ability under various EM duty modes. Even when statistical errors existed, they still delivered the "overestimation" in temperature values rather than "underestimation". For the prevention of overheating task, such miscalculation would introduce no thermal safety regime ignorance problem, which is acceptable. Inversely, the misestimating of peak temperature values by RFR model is not acceptable for practice, the users may lose the information of hotspot or "potential" hotspot on time and lead to overheating of EMs. All three types of ML algorithms presented their characteristics in the temperature estimation task, both advantages and defects. Therefore, we may employ them for EM thermal monitoring task after full considerations of those trade-offs.

3) The design goals of our FBG+ ML thermal sensor system: checking the feasibility of FBG sensors combined with ML algorithms for comprehensive EM winding thermal monitoring, has been achieved: in our thermal experiments, we employed the temperature readings of "odd" positions, EM electrical and mechanical data, and FBG spectral as input features, and temperatures at "even" positions (i.e. T_2, 4, 6, 8) as outputs, S3 mode datasets for ML model training. Then, the optimized SVR and ANN ML models were capable of conducting our temperature prediction task. Now, in our temporal ML models, the number of ratio between input TC measured temperatures (i.e. T_1, 3, 5, 7) and output ML predicted temperatures (i.e. T_2, 4, 6, 8) is 1:1. Such "thermal input-output ratio" of temperature values can be increased further by adjusting the structure of ML model at the design stage, until optimal sensor number obtained.
4) Here we employed S3 duty mode datasets for ML models training and validation, other IEC standard defined duty modes (S1, S2, S9 and S10) for testing. In practice EM applications, the duty modes may be more complicated than S1-S10, it will be customised and scenario-

dependent [188]. We must be aware of the fact that there is no common well-functioned ML models for different application scenarios within different EMs, but the construction process of this novel FBG+ ML thermal monitoring system is universal.

To sum up, there are two (SVR & ANN) of these algorithms that presented acceptable temperature monitoring functions with inner-winding monitoring with ex-situ optimised sensor number of required temperature sensors, in terms of both prediction accuracy and generalization ability. However, still there are opportunities to improve the ML model performance in this application, such as optimising the content of training datasets, introducing more comprehensive hyperparameter list for grid search method. The temporal research has successfully proved the feasibility of using FBG + ML algorithms for internal, ex-situ EM winding temperature prediction under various duty modes. The output temperature data of EM winding can be used for further prognostic and health management of electric machines or other electrical device [181, 182].

Additionally, there are some limitations & rough edges which existed within our EM thermal sensing system prototype: 1) The further generalization ability of our ML model still need to be proven when the inter-machine situations occur, although it has presented a good generalization ability for the intra-machine various duty modes conditions. 2) Lack of negative condition samples (e.g. actual hot-spots or overheating temperature data) within database, neither for training nor testing datasets. This is limited by the EM thermal experiments that we have conducted, no actual overheating failure occurred within our experimental EM. The database should be enriched in future during the thermal experiments for EM of target type.

6.3 FBG with Electric Machines: summary of the findings

In this chapter, we presented the design & implementation process of a novel FBG-ML temperature monitoring system for comprehensive thermal monitoring of EM windings. A test rig and FBG-ML sensing system of EM were constructed for multiple EM duty cycles thermal experiments conduction and data collection. The multiple EM duty-cycle experimental data were employed for the construction and optimization of internal EM winding temperature prediction ML models construction. Three types of ML algorithms were chosen for temperature prediction performance comparison, and we found that the ANN (MLPR) model presented best performance in this EM winding temperature monitoring application compared to SVR and RFR, in terms of both accuracy and generalization ability for cross-duty cycle temperature prediction.

Our novel sensing system has achieved the following improvements:

1) Sensor number reduction without thermal monitoring resolution loss.

2) “hot-spot” temperature value prediction.

3) As the protocol stated in paper, once we completed the data collection with embedded temperature sensors in tested EM, no further large-scale winding-embedded sensors are required for same-type of EM for online temperature monitoring, only FBGs on windings surface, and small number of internal winding sensors are required for a comprehensive, internal temperature monitoring of EM windings. Such FBG + ML thermal monitoring system is suitable for EMs employed in high safety & robustness required scenarios, such as aerospace applications.

4) This FBG-ML combined sensing system partially cancelled the cross-sensitive effects of FBG CW drift, since we set the CWs of FBG sensors as one category of ML input features while the

internal winding temperatures as outputs. The conventional FBG central wavelengths demodulation method is not required any more, we just left this calculation to trained ML models, and the intrinsic cross-sensitive effects of FBG sensors lead by mechanical disturbs can be compensated in this EM winding thermal monitoring application.

The academic contribution of this chapter includes 1) Presenting a novel ML and FBG combined sensing system for comprehensive EM winding temperature monitoring, provide and complete an engineering solution by conducting various EM duty modes thermal experiments with FBG sensor implemented only on the surface of tested EM windings. 2) Applying various types of ML algorithms for temperature prediction, evaluate their performances, and conclude the optimal ML model (ANN) for our target tasks. 3) Presenting a complete design protocol of FBG-ML monitoring system construction, and scientifically verified that the optimal ML model is able to conduct the functions of a) multi-position inner winding temperatures prediction, and b) “hot-spot” temperature prediction. Till now, the experimental validation of FBG-ML thermal monitoring sensing system for EM has been completed as we planned.

7 Conclusion & Future work

7.1 Conclusion & Outlook of this research

In this PhD project, we have reviewed the monitoring systems using multiple FOS techniques for all reliability parameters of EM. Within different types of FOS principles, Fibre Bragg Grating (FBG) sensor was chosen for the thermal monitoring of EMs due to its outstanding advantages for EM thermal monitoring application as discussed in Chapter 2. We have designed and implemented an intelligent sensing method for EM thermal monitoring using FBG sensors with various types of ML algorithms successfully. To achieve the final task of EM comprehensive thermal monitoring, we designed the validation thermal experiments progressively: The thermal experiments have been conducted and validated on 1) ceramic power resistors, 2) enameled copper windings, 3) motorette and 4) operating electric machine. The lab version prototypes for each thermal objects above have been built and validated in the forms of both simulations and experiments shown in Chapter 3-6.

However, it has been proved that there are some other EM reliability parameters that can be measured by FBG sensors , for instance, vibrations, torque, and power as we mentioned in the literature review chapter. One of the outlooks of this project is to extend the target EM physical parameter from one thermal indicator (temperature) to both mechanical and thermal multi-parameters. The presented FBG monitoring prototypes in this project provide a clear and feasible design procedure template of intelligent sensor system construction for temperature monitoring. The monitoring system constructions for other EM parameters may just follow the progress shown in this project.

Another outlook is to construct the proposed closed loop FBG monitoring system for prognostics and health management (PHM) of EMs. In our project, we completed the most vital part of this PHM system: achieve EM comprehensive thermal monitoring with optimal sensor number using FBG sensors with ML algorithms. Adequate thermal distribution data can be provided by the verified outputs of ML models. The data enables EM control side to evaluate the health conditions of EM and respond appropriate control strategies for operating EM maintenance.

7.2 Translational potential of this research

We have applied three Chinese invention patents based on this PhD research project and they were all officially accepted by China National Intellectual Property Administration (CNIPA). Such achievement indicated the strong commercialization potentials of this project. We hypothesized and validated an FBG sensor prototype for electric machine thermal monitoring successfully in this PhD project, using the combination of FBG sensor and machine learning algorithms. In practice, we may employ such advanced sensing method for real-time multi-parameter monitoring under different industrial scenarios. For instance, we applied our first invention patent with name "A system and method for measuring internal temperature of electrical machine windings using fibre-optic sensors and machine learning", which is exactly the content of this PhD research. However, the latter two invention patents were built for condition monitoring and health state evaluations of power electronics devices ("An optic-fiber temperature and reliability measurement system for power electronics components") and wind power systems ("An intelligent optic- fibre based monitoring and control system for optimized operations of wind power systems"), respectively. Such technique application transfer indicated the big translational potential of our research in more industrial infrastructures or circumstances that require condition monitoring.

Bibliography

[1] T. R. Brinner, R. H. McCoy, and T. Kopecky, "Induction versus permanent-magnet motors for electric submersible pump field and laboratory comparisons," *IEEE Trans. Ind. Appl.*, vol. 50, no. 1, pp. 174–181, 2014, doi: 10.1109/TIA.2013.2288203.

[2] D. Gerada, A. Mebarki, N. L. Brown, C. Gerada, A. Cavagnino, and A. Boglietti, "High-speed electrical machines: Technologies, trends, and developments," *IEEE Trans. Ind. Electron.*, vol. 61, no. 6, pp. 2946–2959, 2014, doi: 10.1109/TIE.2013.2286777.

[3] R. Saidur, "A review on electrical motors energy use and energy savings," *Renew. Sustain. Energy Rev.*, vol. 14, no. 3, pp. 877–898, 2010, doi: 10.1016/j.rser.2009.10.018.

[4] M. Vehicles, A. Pacific, and L. America, "Electric Motors : Market Research Report Electric Motors : Market Research Report".

[5] J. Pyrhonen, V. Hrabovcova, and R. S. Semken, *Electrical machine drives control: An introduction*. John Wiley & Sons, 2016.

[6] T. Javied, T. Rackow, R. Stankalla, C. Sterk, and J. Franke, "A study on electric energy consumption of manufacturing companies in the German industry with the focus on electric drives," *Procedia CIRP*, vol. 41, pp. 318–322, 2016.

[7] M. Galea, P. Giangrande, and V. Madonna, "Reliability-Oriented Design of Electrical Machines: The Design Process for Machines' Insulation Systems MUST Evolve," no. March, pp. 20–28, 2020.

[8] A. J. Bazurto, E. C. Quispe, and R. C. Mendoza, "Causes and failures classification of industrial electric motor," *Proc. 2016 IEEE ANDESCON ANDESCON 2016*, 2017, doi: 10.1109/ANDESCON.2016.7836190.

[9] F. He, G. Xie, and J. Luo, "Electrical bearing failures in electric vehicles," *Friction*, vol. 8, no. 1, pp. 4–28, 2020, doi: 10.1007/s40544-019-0356-5.

[10] V. Madonna, P. Giangrande, L. Lusuardi, A. Cavallini, C. Gerada, and M. Galea, "Thermal Overload and Insulation Aging of Short Duty Cycle, Aerospace Motors," *IEEE Trans. Ind. Electron.*, vol. 67, no. 4, pp. 2618–2629, 2020, doi: 10.1109/TIE.2019.2914630.

[11] H. Lasi, P. Fettke, H.-G. Kemper, T. Feld, and M. Hoffmann, "Industry 4.0," *Bus. Inf. Syst. Eng.*, vol. 6, no. 4, pp. 239–242, Aug. 2014, doi: 10.1007/s12599-014-0334-4.

[12] D. O. M. Sanchez, "Sustainable Development Challenges and Risks of Industry 4.0: A literature review," in *2019 Global IoT Summit (GIoTS)*, Jun. 2019, pp. 1–6. doi: 10.1109/GIOTS.2019.8766414.

[13] “Global Electric Motor Market to Grow at Nearly 7% in Coming Years.” https://www.blueweaveconsulting.com/press-release/global-electric-motor-market-to-grow-at-nearly-7-in-coming-years (accessed Jun. 15, 2022).

[14] K. Shang, Y. Zhang, M. Galea, V. Brusic, and S. Korposh, “Fibre optic sensors for the monitoring of rotating electric machines : a review,” *Opt. Quantum Electron.*, vol. 53, no. 2, p. 75, 2021, doi: 10.1007/s11082-020-02712-y.

[15] M. Galea, C. Gerada, T. Raminosoa, and P. Wheeler, “A Thermal Improvement Technique for the Phase Windings of Electrical Machines,” *IEEE Trans. Ind. Appl.*, vol. 48, no. 1, pp. 79–87, Jan. 2012, doi: 10.1109/TIA.2011.2175470.

[16] V. Madonna, A. Walker, P. Giangrande, G. Serra, C. Gerada, and M. Galea, “Improved Thermal Management and Analysis for Stator End-Windings of Electrical Machines,” *IEEE Trans. Ind. Electron.*, vol. 66, no. 7, pp. 5057–5069, Jul. 2019, doi: 10.1109/TIE.2018.2868288.

[17] NEMA, “MG 1-2016 Motors and Generators,” NEMA, 2018.

[18] Y. Yang *et al.*, “Thermal management of electric machines,” *IET Electr. Syst. Transp.*, vol. 7, no. 2, pp. 104–116, 2017, doi: 10.1049/iet-est.2015.0050.

[19] P. Gnacinski, “Windings Temperature and Loss of Life of an Induction Machine Under Voltage Unbalance Combined With Over- or Undervoltages,” *IEEE Trans. Energy Convers.*, vol. 23, no. 2, pp. 363–371, Jun. 2008, doi: 10.1109/TEC.2008.918596.

[20] M. T. Isha and Z. Wang, “Transformer hotspot temperature calculation using IEEE loading guide,” in *2008 International Conference on Condition Monitoring and Diagnosis*, Apr. 2008, pp. 1017–1020. doi: 10.1109/CMD.2008.4580455.

[21] D.-J. Kim, J.-W. Jung, S.-O. Kwon, and J.-P. Hong, “Thermal analysis using equivalent thermal network in IPMSM,” in *2008 International Conference on Electrical Machines and Systems*, 2008, pp. 3162–3165.

[22] A. Boglietti, A. Cavagnino, D. Staton, M. Shanel, M. Mueller, and C. Mejuto, “Evolution and Modern Approaches for Thermal Analysis of Electrical Machines,” *IEEE Trans. Ind. Electron.*, vol. 56, no. 3, pp. 871–882, Mar. 2009, doi: 10.1109/TIE.2008.2011622.

[23] Y. Zhang, J. Ruan, T. Huang, X. Yang, H. Zhu, and G. Yang, “Calculation of Temperature Rise in Air-cooled Induction Motors Through 3-D Coupled Electromagnetic Fluid-Dynamical and Thermal Finite-Element Analysis,” *IEEE Trans. Magn.*, vol. 48, no. 2, pp. 1047–1050, 2012, doi: 10.1109/TMAG.2011.2174433.

[24] K. Kudelina, T. Vaimann, B. Asad, A. Rassõlkin, A. Kallaste, and G. Demidova, “Trends and Challenges in Intelligent Condition Monitoring of Electrical Machines Using Machine Learning,” *Appl. Sci.*, vol. 11, no. 6, Art. no. 6, Jan. 2021, doi: 10.3390/app11062761.

[25] W. Kirchgassner, O. Wallscheid, and J. Böcker, “Data-Driven Permanent Magnet Temperature Estimation in Synchronous Motors with Supervised Machine Learning: A Benchmark,” *IEEE Trans. Energy Convers.*, 2021.

[26] D. Czerwinski, J. Gęca, and K. Kolano, “Machine Learning for Sensorless Temperature Estimation of a BLDC Motor,” *Sensors*, vol. 21, no. 14, p. 4655, Jul. 2021, doi: 10.3390/s21144655.

[27] G. Feng, C. Lai, J. Tjong, and N. C. Kar, “Noninvasive Kalman Filter Based Permanent Magnet Temperature Estimation for Permanent Magnet Synchronous Machines,” *IEEE Trans. Power Electron.*, vol. 33, no. 12, pp. 10673–10682, Dec. 2018, doi: 10.1109/TPEL.2018.2808323.

[28] L. Cheng and T. Yu, “A new generation of AI: A review and perspective on machine learning technologies applied to smart energy and electric power systems,” *Int. J. Energy Res.*, vol. 43, no. 6, pp. 1928–1973, May 2019, doi: 10.1002/er.4333.

[29] M. Fabian, D. M. Hind, C. Gerada, T. Sun, and K. T. V. Grattan, “Comprehensive Monitoring of Electrical Machine Parameters Using an Integrated Fiber Bragg Grating-Based Sensor System,” *J. Light. Technol.*, vol. 36, no. 4, pp. 1046–1051, 2018, doi: 10.1109/JLT.2017.2771143.

[30] E. Udd, “The Emergence of Fiber Optic Sensor Technology,” in *Fiber Optic Sensors: An Introduction for Engineers and Scientists*, Hoboken, NJ, USA: John Wiley & Sons, Inc., 2011, p. 512. doi: 10.1002/9781118014103.ch1.

[31] K. T. V. Grattan and T. Sun, “Fiber optic sensor technology: an overview,” *Sens. Actuators Phys.*, vol. 82, no. 1, pp. 40–61, May 2000, doi: 10.1016/S0924-4247(99)00368-4.

[32] K. Shang, M. Galea, V. Brusic, S. Korposh, and Y. Zhang, “Polyimide-coated fibre bragg grating (FBG) sensors for thermal mapping of electric machine windings,” in *2020 22nd International Conference on Transparent Optical Networks (ICTON)*, 2020, pp. 1–4.

[33] kun shang, michael galea, vladimir brusic, weiduo zhao, and yaping zhang, “Fibre Bragg grating (FBG) thermal monitoring system for copper windings of electric machines under different duty modes,” in *International Conference on Sensors and Instruments (ICSI 2021)*, Qingdao, China, Jul. 2021, p. 2. doi: 10.1117/12.2602885.

[34] A. Mohammed and S. Djurović, “Stator Winding Internal Thermal Monitoring and Analysis Using In Situ FBG Sensing Technology,” *IEEE Trans. Energy Convers.*, vol. 33, no. 3, pp. 1508–1518, Sep. 2018, doi: 10.1109/TEC.2018.2826229.

[35] E. Udd and W. B. Spillman, *FIBER OPTIC SENSORS FIBER OPTIC SENSORS An Introduction for Engineers and Scientists*. 2011.

[36] K. Shang, Y. Zhang, M. Galea, V. Brusic, and S. Korposh, “Fibre optic sensors for the monitoring of rotating electric machines: a review,” *Opt. Quantum Electron.*, vol. 53, no. 2, p. 75, Jan. 2021, doi: 10.1007/s11082-020-02712-y.

[37] P. J. Tavner, “Review of condition monitoring of rotating electrical machines. Electric Power Applications,” *IET ElectrPower Appl*, vol. 2, no. 4, pp. 215–247, 2008, doi: 10.1049/iet-epa.

[38] W. R. Finley, M. M. Hodowanec, and W. G. Holter, “an Analytical Approach To Solving,” *IEEE PCIC*, no. Paper No PCIC-99-20, pp. 217–232, 1999.

[39] EMSA, “Life Cycle Cost Analyses,” 2019. https://www.motorsystems.org/task-b/life-cycle-cost (accessed Jul. 29, 2019).

[40] A. T. de Almeida, J. Fong, H. Falkner, and P. Bertoldi, “Policy options to promote energy efficient electric motors and drives in the EU,” *Renew. Sustain. Energy Rev.*, vol. 74, no. January, pp. 1275–1286, 2017, doi: 10.1016/j.rser.2017.01.112.

[41] J. Meyer, A. Nedjalkov, A. Doering, M. Angelmahr, and W. Schade, “Fiber optical sensors for enhanced battery safety,” May 2015, vol. 9480, p. 94800Z. doi: 10.1117/12.2183325.

[42] J. Habel, T. Boilard, J. S. Frenière, F. Trépanier, and M. Bernier, “Femtosecond FBG written through the coating for sensing applications,” *Sens. Switz.*, vol. 17, no. 11, pp. 1–11, 2017, doi: 10.3390/s17112519.

[43] TECHNICA.Ltd, “T20 / Polyimide Coated FBG sensor Datasheet,” 2018.

[44] FIBRECORE.Ltd, “Pure Silica Core SM Fiber Product specification,” 2018.

[45] V. Giurgiutiu, *Chapter 7 - Fiber-Optic Sensors*. 2016. doi: https://doi.org/10.1016/B978-0-12-409605-9.00007-6.

[46] C. Wang, Q. Lu, and L. Cheng, “Novel type of temperature self-compensating acceleration transducer based on ofbg,” *IEEE Sens. J.*, vol. 13, no. 8, pp. 3012–3013, 2013, doi: 10.1109/JSEN.2013.2253604.

[47] N. Basumallick, I. Chatterjee, P. Biswas, K. Dasgupta, and S. Bandyopadhyay, “Fiber Bragg grating accelerometer with enhanced sensitivity,” *Sens. Actuators Phys.*, vol. 173, no. 1, pp. 108–115, 2012, doi: 10.1016/j.sna.2011.10.026.

[48] L. Liu, H. Zhang, Q. Zhao, Y. Liu, and F. Li, “Temperature-independent FBG pressure sensor with high sensitivity,” *Opt. Fiber Technol.*, vol. 13, no. 1, pp. 78–80, 2007, doi: 10.1016/j.yofte.2006.09.001.

[49] C. sub Park, K. Il Joo, S. W. Kang, and H. R. Kim, “A PDMS-coated optical fiber Bragg grating sensor for enhancing temperature sensitivity,” *J. Opt. Soc. Korea*, vol. 15, no. 4, pp. 329–334, 2011, doi: 10.3807/JOSK.2011.15.4.329.

[50] A. Ukil, H. Braendle, and P. Krippner, “Distributed temperature sensing: Review of technology and applications,” *IEEE Sens. J.*, vol. 12, no. 5, pp. 885–892, 2012, doi: 10.1109/JSEN.2011.2162060.

[51] G. Bolognini and A. Hartog, “Raman-based fibre sensors: Trends and applications,” *Opt. Fiber Technol.*, vol. 19, no. 6, pp. 678–688, Dec. 2013, doi: 10.1016/j.yofte.2013.08.003.

[52] J. P. Dakin, D. J. Pratt, G. W. Bibby, and J. N. Ross, “Distributed optical fibre Raman temperature sensor using a semiconductor light source and detector,” *Electron. Lett.*, vol. 21, no. 13, pp. 569–570, 1985, doi: 10.1049/el:19850402.

[53] A. D. Kersey, “Distributed and Multiplexed Fiber Optic Sensors,” *Fiber Opt. Sens. Introd. Eng. Sci. Second Ed.*, pp. 277–314, 2011, doi: 10.1002/9781118014103.ch11.

[54] V. Budinski and D. Donlagic, “Fiber-optic sensors for measurements of torsion, twist and rotation: A review,” *Sens. Switz.*, vol. 17, no. 3, pp. 1–29, 2017, doi: 10.3390/s17030443.

[55] L. Kruger, P. L. Swart, A. A. Chtcherbakov, and A. J. van Wyk, “Non-contact torsion sensor using fibre Bragg gratings,” *Meas. Sci. Technol.*, vol. 15, no. 8, pp. 1448–1452, 2004, doi: 10.1088/0957-0233/15/8/002.

[56] R. L. Mott and J. A. Untener, *Applied strength of materials*. 2017.

[57] L. H. Shyu, Y. C. Wang, C. P. Chang, H. T. Shih, and E. Manske, “A signal interpolation method for Fabry-Perot interferometer utilized in mechanical vibration measurement,” *Meas. J. Int. Meas. Confed.*, vol. 92, pp. 83–88, 2016, doi: 10.1016/j.measurement.2016.05.072.

[58] T. K. Gangopadhyay, “Prospects for Fibre Bragg gratings and Fabry-Perot interferometers in fibre-optic vibration sensing,” *Sens. Actuators Phys.*, vol. 113, no. 1, pp. 20–38, 2004, doi: 10.1016/j.sna.2004.01.043.

[59] J. H. Galeti, C. Kitano, and M. J. Connelly, “Improved synthetic-heterodyne Michelson interferometer vibrometer using phase and gain control feedback,” *Appl. Opt.*, vol. 54, no. 35, p. 10418, 2015, doi: 10.1364/ao.54.010418.

[60] H. He *et al.*, “Multiple vibrations measurement using phase-sensitive OTDR merged with Mach-Zehnder interferometer based on frequency division multiplexing,” *Opt. Express*, vol. 24, no. 5, p. 4842, 2016, doi: 10.1364/oe.24.004842.

[61] A. Cusano, A. Cutolo, J. Nasser, M. Giordano, and A. Calabrò, "Dynamic strain measurements by fibre Bragg grating sensor," *Sens. Actuators Phys.*, vol. 110, no. 1–3, pp. 276–281, 2004, doi: 10.1016/j.sna.2003.10.031.

[62] S. R. K. Morikawa, A. S. Ribeiro, R. D. Regazzi, L. C. G. Valente, and A. M. B. Braga, "Triaxial Bragg grating accelerometer," *2002 15th Opt. Fiber Sens. Conf. Tech. Dig. 2002*, pp. 95–98, 2002, doi: 10.1109/OFS.2002.1000510.

[63] R. P. Linessio, K. De Morais Sousa, T. Da Silva, C. A. Bavastri, P. F. Da Costa Antunes, and J. C. C. Da Silva, "Induction Motors Vibration Monitoring Using a Biaxial Optical Fiber Accelerometer," *IEEE Sens. J.*, vol. 16, no. 22, pp. 8075–8082, 2016, doi: 10.1109/JSEN.2016.2604850.

[64] T. A. Berkoff and A. D. Kersey, "Experimental demonstration of a fiber bragg grating accelerometer," *IEEE Photonics Technol. Lett.*, vol. 8, no. 12, pp. 1677–1679, 1996, doi: 10.1109/68.544716.

[65] Y. Chen, X. Zhang, P. Zhang, and C. Liu, "Lubricant film thickness measurement using fiber-optic Michelson Interferometer and fiber-optic displacement sensor," *2009 IEEE Int. Conf. Inf. Autom. ICIA 2009*, pp. 951–956, 2009, doi: 10.1109/ICINFA.2009.5205055.

[66] X. Zhang, X. Wu, and W. Diao, "An approach for the dynamic compensation of the batch balance in the process control," *Proc. - 2004 Int. Conf. Intell. Mechatron. Autom.*, no. August, pp. 789–792, 2004, doi: 10.1109/icima.2004.1384305.

[67] G. Perrone and A. Vallan, "A Low-Cost Optical Sensor for Noncontact Vibration Measurements," vol. 58, no. 5, pp. 1650–1656, 2009.

[68] E. Udd, "Fiber Optic Sensors Based on the sagnac interferometer and passive ring resonator," in *Fiber Optic Sensors: An Introduction for Engineers and Scientists*, 2011, pp. 199–230.

[69] V. Vali and R. W. Shorthill, "Fiber ring interferometer," *Appl. Opt.*, vol. 15, no. 5, p. 1099, 1976, doi: 10.1364/ao.15.001099.

[70] W. K. Burns, *Optical Fiber Rotation Sensing*. Academic Press, 1994. doi: 10.1016/c2009-0-22412-3.

[71] K. T. A. Ghatak, "Optical Fiber Sensors 14.1," in *Fiber Optic Essentials*, 1st ed., John Wiley & Sons, Inc., 2007, pp. 221–235. doi: 10.1002/9780470152560.

[72] H. C. Lefèvre, "The fiber-optic gyroscope, a century after Sagnac's experiment: The ultimate rotation-sensing technology?," *Comptes Rendus Phys.*, vol. 15, no. 10, pp. 851–858, 2014, doi: 10.1016/j.crhy.2014.10.007.

[73] H. Y. Chang, C. Y. Huang, W. F. Liu, J. G. Li, C. Y. Kuo, and M. Y. Fu, "Rotational speed sensors based on a fiber Bragg grating," *2017 Opto-Electron. Commun. Conf. OECC 2017 Photonics Glob. Conf. PGC 2017*, vol. 2017-Novem, pp. 1–3, 2017, doi: 10.1109/OECC.2017.8114863.

[74] L. Wei, Z. Zhou, Y. Tan, L. Yuan, and T. Hu, "Fiber bragg grating based rotating speed measurement system," *2011 Int. Conf. Electr. Inf. Control Eng. ICEICE 2011 - Proc.*, pp. 1387–1390, 2011, doi: 10.1109/ICEICE.2011.5777520.

[75] A. Patel and M. Ferdowsi, "Current sensing for automotive electronics - A survey," *IEEE Trans. Veh. Technol.*, vol. 58, no. 8, pp. 4108–4119, 2009, doi: 10.1109/TVT.2009.2022081.

[76] D. Xu, B. Wang, G. Zhang, G. Wang, and Y. Yu, "A review of sensorless control methods for AC motor drives," *Trans. Electr. Mach. Syst.*, vol. 2, no. 1, pp. 104–115, 2019, doi: 10.23919/TEMS.2018.8326456.

[77] P. Mihailovic, S. Petricevic, Z. Stojkovic, and J. B. Radunovic, "Development of a portable fiber-optic current sensor for power systems monitoring," *IEEE Trans. Instrum. Meas.*, vol. 53, no. 1, pp. 24–30, 2004, doi: 10.1109/TIM.2003.821500.

[78] J. N. Blake and A. H. Rose, "Fiber-Optic Current Transducer Optimized for Power Metering Applications," *Proc. IEEE Power Eng. Soc. Transm. Distrib. Conf.*, vol. 1, pp. 405–408, 2003, doi: 10.1109/tdc.2003.1335257.

[79] C. K. Kirkendall and A. Dandridge, "Overview of high performance fibre-optic sensing," *J. Phys. Appl. Phys.*, vol. 37, no. 18, 2004, doi: 10.1088/0022-3727/37/18/R01.

[80] K. Cui, W. Peng, Z. Ren, J. Qian, and R. Zhu, "FPGA-based interrogation controller with optimized pipeline architecture for very large-scale fiber-optic interferometric sensor arrays," *Opt. Lasers Eng.*, vol. 121, no. May, pp. 389–396, 2019, doi: 10.1016/j.optlaseng.2019.04.026.

[81] W. Eickhoff and R. Ulrich, "Optical frequency domain reflectometry in single-mode fiber," *Appl. Phys. Lett.*, vol. 39, no. 9, pp. 693–695, 1981, doi: 10.1063/1.92872.

[82] D. Uttam and B. Culshaw, "Precision Time Domain Reflectometry in Optical Fiber Systems Using a Frequency Modulated Continuous Wave Ranging Technique," *J. Light. Technol.*, vol. 3, no. 5, pp. 971–977, 1985, doi: 10.1109/JLT.1985.1074315.

[83] Y. Lu, T. Zhu, L. Chen, and X. Bao, "Distributed vibration sensor based on coherent detection of phase-OTDR," *J. Light. Technol.*, vol. 28, no. 22, pp. 3243–3249, 2010, doi: 10.1109/JLT.2010.2078798.

[84] A. J. Rogers, "Polarization-optical time domain reflectometry: a technique for the measurement of field distributions," *Appl. Opt.*, vol. 20, no. 6, p. 1060, 1981, doi: 10.1364/ao.20.001060.

[85] Z. Gao, T. G. Habetler, R. G. Harley, and R. S. Colby, “A sensorless rotor temperature estimator for induction machines based on current harmonic spectral estimation scheme,” *EPE-PEMC 2006 12th Int. Power Electron. Motion Control Conf. Proc.*, vol. 55, no. 1, pp. 431–437, 2007, doi: 10.1109/EPEPEMC.2006.283200.

[86] C. M. Riley, B. K. Lin, T. G. Habetler, and G. B. Kliman, “Stator current harmonics and their causal vibrations: a preliminary investigation of sensorless vibration monitoring applications,” *IEEE Trans. Ind. Appl.*, vol. 35, no. 1, pp. 94–99, 1999, doi: 10.1109/28.740850.

[87] T. a Jankowski *et al.*, “Development and Validation of a Thermal Model for Electric Induction Motors,” *IEEE Trans. Ind. Electron.*, vol. 57, no. 12, pp. 4043–4054, 2010, doi: 10.1109/TIE.2010.2043044.

[88] C. Hudon, M. Levesque, L. Zou, and J. Picard, “Determination of stator temperature profile using distributed sensing,” *2013 IEEE Electr. Insul. Conf. EIC 2013*, no. June, pp. 191–195, 2013, doi: 10.1109/EIC.2013.6554231.

[89] D. Lopez-Perez and J. Antonino-Daviu, “Application of Infrared Thermography to Failure Detection in Industrial Induction Motors: Case Stories,” *IEEE Trans. Ind. Appl.*, vol. 53, no. 3, pp. 1901–1908, 2017, doi: 10.1109/TIA.2017.2655008.

[90] M. Sunar and B. O. Al-Bedoor, “Vibration measurement of rotating blades using a root embedded PZT sensor,” *Shock Vib.*, vol. 15, no. 5, pp. 517–541, 2008, doi: 10.1155/2008/494639.

[91] W. Chen, J. Jiang, J. Liu, S. Bai, and W. Chen, “A passive eddy current damper for vibration suppression of a force sensor,” *J. Phys. Appl. Phys.*, vol. 46, no. 8, 2013, doi: 10.1088/0022-3727/46/7/075001.

[92] K. Ágoston, “Vibration Detection of the Electrical Motors using Strain Gauges,” in *Procedia Technology*, 2016, vol. 22, pp. 767–772. doi: 10.1016/j.protcy.2016.01.037.

[93] X. Li and E. C. Kan, “A wireless low-range pressure sensor based on P(VDF-TrFE) piezoelectric resonance,” *Sens. Actuators Phys.*, vol. 163, no. 2, pp. 457–463, 2010, doi: 10.1016/j.sna.2010.08.022.

[94] B. Beihoff, “Survey of torque transduction methodologies for industrial applications,” *IEEE Conf. Rec. Annu. Pulp Pap. Ind. Tech. Conf.*, pp. 220–229, 1996, doi: 10.1109/papcon.1996.536001.

[95] Machine Design, “Basics of Rotary Encoders: Overview and New Technologies | Sensors content from Machine Design,” 2014.

[96] A. Murray, B. Hare, and A. Hirao, “Resolver Position Sensing System With Integrated Fault Detection for Automotive Applications,” *Proc. IEEE Sens.*, vol. 1, no. 2, pp. 864–869, 2002, doi: 10.1109/icsens.2002.1037221.

[97] C. M. Burt, X. Piao, F. Gaudi, B. Busch, and N. N. Taufik, “Electric motor efficiency under variable frequencies and loads,” *J. Irrig. Drain. Eng.*, vol. 134, no. 2, pp. 129–136, 2008, doi: 10.1061/(ASCE)0733-9437(2008)134:2(129).

[98] H. A. Toliyat and G. B. Kliman, *Handbook of electric motors*, vol. 120. CRC press, 2018.

[99] J. Huang *et al.*, “Real-time measurement of temperature field in heavy-duty machine tools using fiber Bragg grating sensors and analysis of thermal shift errors,” *Mechatronics*, vol. 31, pp. 16–21, 2015, doi: 10.1016/j.mechatronics.2015.04.004.

[100] A. Hughes and B. Drury, *Electric motors and drives : fundamentals, types and applications*. Newnes, 2013.

[101] A. Emadi and F. Berthold, *Advanced electric drive vehicles*. CRC Press, 2017.

[102] Y. Yang *et al.*, “Design and Comparison of Interior Permanent Magnet Motor Topologies for Traction Applications,” *IEEE Trans. Transp. Electrification*, vol. 3, no. 1, pp. 86–97, 2017, doi: 10.1109/TTE.2016.2614972.

[103] G. Munteanu, A. Binder, and T. Schneider, “Loss measurement of a 40 kW high-speed bearingless PM synchronous motor,” *IEEE Energy Convers. Congr. Expo. Energy Convers. Innov. Clean Energy Future ECCE 2011 Proc.*, no. 6, pp. 722–729, 2011, doi: 10.1109/ECCE.2011.6063841.

[104] A. Mohammed and S. Djurović, “Stator Winding Internal Thermal Monitoring and Analysis Using In Situ FBG Sensing Technology,” *IEEE Trans. Energy Convers.*, vol. 33, no. 3, pp. 1508–1518, 2018, doi: 10.1109/TEC.2018.2826229.

[105] A. Mohammed and S. Djurović, “A study of distributed embedded thermal monitoring in electric coils based on FBG sensor multiplexing,” *Microprocess. Microsyst.*, vol. 62, pp. 102–109, 2018, doi: 10.1016/j.micpro.2018.07.006.

[106] K. Tshiloz, A. C. Smith, A. Mohammed, S. Djurovic, and T. Feehally, “Real-time insulation lifetime monitoring for motor windings,” *Proc. - 2016 22nd Int. Conf. Electr. Mach. ICEM 2016*, pp. 2335–2340, 2016, doi: 10.1109/ICELMACH.2016.7732847.

[107] K. Shang, M. Galea, V. Brusic, S. Korposh, and Y. Zhang, “Polyimide-Coated Fibre Bragg Grating (FBG) Sensors for Thermal Mapping of Electric Machine Windings,” in *22nd International Conference on Transparent Optical Networks (ICTON 2020)*, 2020, pp. 4–7.

[108] N. Haramoni, A. S. Paterno, A. Goedtel, G. R. Soares, J. C. C. Silva, and H. J. Kalinowski, “Hybrid wavelength-time-domain interrogation system for multiplexed fiber Bragg sensors using a strain-tuned erbium-doped fiber laser,” *IEEE Sens. J.*, vol. 8, no. 7, pp. 1061–1066, 2008, doi: 10.1109/JSEN.2008.926175.

[109] C. Hudon, C. Guddemi, S. Gingras, R. C. Leite, and L. Mydlarski, “Rotor temperature monitoring using fiber Bragg gratings,” in *2016 IEEE Electrical Insulation Conference (EIC)*, Jun. 2016, pp. 456–459. doi: 10.1109/EIC.2016.7548636.

[110] R. C. Leite *et al.*, “Analysis of thermo-mechanical stress in fiber bragg grating used for hydro-generator rotor temperature monitoring,” *J. Microw. Optoelectron. Electromagn. Appl.*, vol. 16, no. 2, pp. 445–459, 2017, doi: 10.1590/2179-10742017v16i2818.

[111] K. De Morais Sousa, A. A. Hafner, H. José Kalinowski, and J. C. C. Da Silva, “Determination of temperature dynamics and mechanical and stator losses relationships in a three-phase induction motor using fiber bragg grating sensors,” *IEEE Sens. J.*, vol. 12, no. 10, pp. 3054–3061, 2012, doi: 10.1109/JSEN.2012.2210203.

[112] K. De Morais Sousa, A. A. Hafner, E. G. Carati, H. J. Kalinowski, and J. C. C. Da Silva, “Validation of thermal and electrical model for induction motors using fiber Bragg gratings,” *Meas. J. Int. Meas. Confed.*, vol. 46, no. 6, pp. 1781–1790, 2013, doi: 10.1016/j.measurement.2013.02.008.

[113] R. G. Duncan, B. A. Childers, and V. Rajendran, “High-spatial-resolution temperature monitoring of an industrial motor using a distributed fiber optic sensing technique,” *Smart Struct. Mater. 2004 Smart Sens. Technol. Meas. Syst.*, vol. 5384, p. 258, 2004, doi: 10.1117/12.540130.

[114] V. P. Rajendran, M. Deblock, T. Wetzel, M. Lusted, C. Kaminski, and B. A. Childers, “Use of fiber optic-based distributed temperature measurement system for electrical machines,” *Opt. Diagn. Fluids Solids Combust. II*, vol. 5191, no. November 2003, p. 214, 2004, doi: 10.1117/12.504249.

[115] C. Hudon, C. Guddemi, S. Gingras, R. C. Leite, and L. Mydlarski, “Rotor temperature monitoring using fiber Bragg gratings,” *34th Electr. Insul. Conf. EIC 2016*, no. June, pp. 456–459, 2016, doi: 10.1109/EIC.2016.7548636.

[116] A. A. Boiarski, G. Pilate, T. Fink, and N. Nilsson, “Temperature Measurements in Power Plant Equipment Using Distributed Fiber Optic Sensing,” *IEEE Trans. Power Deliv.*, vol. 10, no. 4, pp. 1771–1778, 1995, doi: 10.1109/61.473381.

[117] A. Mohammed, S. Djurovic, A. C. Smith, and K. Tshiloz, “FBG sensing for hot spot thermal monitoring in electric machinery random wound components,” *Proc. - 2016 22nd Int. Conf. Electr. Mach. ICEM 2016*, pp. 2266–2272, 2016, doi: 10.1109/ICELMACH.2016.7732837.

[118] Zheng Ping, Pan Shiyong, and Li Yong, “The research on the network optical fiber sensor of the surface temperature measurement for a large rotor based on IEEE1451.2,” in *2005 International Conference on Electrical Machines and Systems*, 2005, pp. 2434-2436 Vol. 3. doi: 10.1109/ICEMS.2005.203010.

[119] U. J. Dreyer *et al.*, "Quasi-Distributed Optical Fiber Transducer for Simultaneous Temperature and Vibration Sensing in High-Power Generators," *IEEE Sens. J.*, vol. 18, no. 4, pp. 1547–1554, 2018, doi: 10.1109/JSEN.2017.2787681.

[120] P. Wang, J. Liu, F. Song, and H. Zhao, "Quasi-distributed temperature measurement for stator bars in large generator via use of Fiber Bragg Gratings," *Proc. 6th Int. Forum Strateg. Technol. IFOST 2011*, vol. 2, pp. 810–813, 2011, doi: 10.1109/IFOST.2011.6021144.

[121] K. de Morais Sousa, W. Probst, F. Bortolotti, C. Martelli, and J. C. C. da Silva, "Fiber bragg grating temperature sensors in a 6.5-MW generator exciter bridge and the development and simulation of its thermal model," *Sens. Switz.*, vol. 14, no. 9, pp. 16651–16663, 2014, doi: 10.3390/s140916651.

[122] NEMA, "NEMA MG 1-2016 Motors and Generators," 2018.

[123] IEC, "IEC 60034:2019 SER," 2019.

[124] The Association of Electrical Equipment and Medical Imaging Manufacturers - NEMA, "Ansi/Nema Mg 1-2016," p. 775, 2016, doi: Document ID: 100228.

[125] W. Finley, M. Loutfi, and B. J. Sauer, "Motor vibration problems Understanding and identifying," *IEEE Cem. Ind. Tech. Conf. Pap.*, pp. 1–20, 2013, doi: 10.1109/CITCON.2013.6525282.

[126] B. E. Hashish, K. Miller, W. Finley, and S. Kreitzer, "Vibration Diagnostic Challenges," no. August, 2017.

[127] H. Z. Yang, X. G. Qiao, D. Luo, K. S. Lim, W. Chong, and S. W. Harun, "A review of recent developed and applications of plastic fiber optic displacement sensors," *Meas. J. Int. Meas. Confed.*, vol. 48, no. 1, pp. 333–345, 2014, doi: 10.1016/j.measurement.2013.11.007.

[128] F. J. Arregui, I. R. Matias, J. M. Corres, and J. Bravo, "Unbalance and harmonics detection in induction motors using an optical fiber sensor," *IEEE Sens. J.*, vol. 6, no. 3, pp. 605–612, 2006, doi: 10.1109/JSEN.2006.874441.

[129] J. M. Corres, J. Bravo, F. J. Arregui, and I. R. Matias, "Vibration monitoring in electrical engines using an in-line fiber etalon," *Sens. Actuators Phys.*, vol. 132, no. 2, pp. 506–515, 2006, doi: 10.1016/j.sna.2006.02.026.

[130] P. G. Jia, D. H. Wang, G. Yuan, and X. Y. Jiang, "An active temperature compensated fiber-optic fabry-perot accelerometer system for simultaneous measurement of vibration and temperature," *IEEE Sens. J.*, vol. 13, no. 6, pp. 2334–2340, 2013, doi: 10.1109/JSEN.2013.2251879.

[131] S. Binu, V. P. Mahadevan Pillai, and N. Chandrasekaran, “Fibre optic displacement sensor for the measurement of amplitude and frequency of vibration,” *Opt. Laser Technol.*, vol. 39, no. 8, pp. 1537–1543, 2007, doi: 10.1016/j.optlastec.2006.12.008.

[132] J. M. López-Higuera, M. A. Morante, and A. Cobo, “Simple low-frequency optical fiber accelerometer with large rotating machine monitoring applications,” *J. Light. Technol.*, vol. 15, no. 7, pp. 1120–1129, 1997, doi: 10.1109/50.596957.

[133] G. Conforti, M. Brenci, A. Mencaglia, and A. G. Mignani, “Fiber optic vibration sensor for remote monitoring in high power electric machines,” *Appl. Opt.*, vol. 28, no. 23, p. 5158, 1989, doi: 10.1364/ao.28.005158.

[134] J. M. Lopez-Higuera *et al.*, “New low-cost fiber optic accelerometer system for stator winding monitoring of hydroelectric generating machines,” in *Proceedings of SPIE - The International Society for Optical Engineering*, 1996, vol. 2868, pp. 510–515. doi: 10.1117/12.248675.

[135] K. d. M. Sousa, U. J. Dreyer, C. Martelli, and J. C. Cardozo da Silva, “Thermal and vibration dynamic analysis of an induction motor using optical fiber Bragg gratings,” *24th Int. Conf. Opt. Fibre Sens.*, vol. 9634, no. September 2015, p. 963443, 2015, doi: 10.1117/12.2195034.

[136] T. Li, C. Shi, Y. Tan, and Z. Zhou, “Fiber Bragg Grating Sensing-Based Online Torque Detection on Coupled Bending and Torsional Vibration of Rotating Shaft,” *IEEE Sens. J.*, vol. 17, no. 7, pp. 1199–2007, 2017, doi: 10.1109/JSEN.2017.2669528.

[137] H. L. Rivera, J. A. García-Souto, and J. Sanz, “Measurements of mechanical vibrations at magnetic cores of power transformers with fiber-optic interferometric intrinsic sensor,” *IEEE J. Sel. Top. Quantum Electron.*, vol. 6, no. 5, pp. 788–797, 2000, doi: 10.1109/2944.892619.

[138] L. Hubner *et al.*, “Monitoring of winding overhang vibrations on large synchronous motors,” *11th Pet. Chem. Ind. Conf. Eur. Electr. Instrum. Appl. PCIC 2014*, 2014, doi: 10.1109/PCICEurope.2014.6900061.

[139] M. Sasic, H. Jiang, and G. C. Stone, “Requirements for fiber optic sensors for stator endwinding vibration monitoring,” *Proc. 2012 IEEE Int. Conf. Cond. Monit. Diagn. CMD 2012*, no. September, pp. 118–121, 2012, doi: 10.1109/CMD.2012.6416365.

[140] “FOA ™-Series Fiber Optic Accelerometers User’s Manual,” 2015.

[141] Y. Wang, L. Liang, Y. Yuan, G. Xu, and F. Liu, “A two fiber Bragg gratings sensing system to monitor the torque of rotating shaft,” *Sens. Switz.*, vol. 16, no. 1, pp. 1–8, 2016, doi: 10.3390/s16010138.

[142] J. M. Lee and Y. Hwang, “A novel online rotor condition monitoring system using fiber Bragg grating (FBG) sensors and a rotary optical coupler,” *Meas. Sci. Technol.*, vol. 19, no. 6, 2008, doi: 10.1088/0957-0233/19/6/065303.

[143] Z. H. Kafafi *et al.*, “The role of photonics in energy,” *J. Photonics Energy*, vol. 5, no. 1, 2015, doi: 10.1117/1.JPE.5.050997.

[144] Y. Liu, H. Jiang, and L. Yuan, “Multi-ring compound fiber optic rotation measuring approach based on the Rayleigh backscattering,” *Proc. 2012 Int. Conf. Meas. Inf. Control MIC 2012*, vol. 1, no. Mic, pp. 107–112, 2012, doi: 10.1109/MIC.2012.6273310.

[145] J. T. Newmaster, M. R. Brininstool, T. Hofler, and S. L. Garrett, “Remote Fiber Optic Sensors For Angular Orientation,” *Fiber Opt. Laser Sens. V*, vol. 0838, no. March 1988, p. 28, 2012, doi: 10.1117/12.942486.

[146] B. Culshaw, “The optical fibre Sagnac interferometer: An overview of its principles and applications,” *Meas. Sci. Technol.*, vol. 17, no. 1, 2006, doi: 10.1088/0957-0233/17/1/R01.

[147] F. Marignetti *et al.*, “Fiber Bragg Grating Sensor for Electric Field Measurement in the End Windings of High-Voltage Electric Machines,” *IEEE Trans. Ind. Electron.*, vol. 63, no. 5, pp. 2796–2802, 2016, doi: 10.1109/TIE.2016.2516500.

[148] G. Fusiek, P. Niewczas, and J. R. McDonald, “Feasibility study of the application of optical voltage and current sensors and an arrayed waveguide grating for aero-electrical systems,” *Sens. Actuators Phys.*, vol. 147, no. 1, pp. 177–182, 2008, doi: 10.1016/j.sna.2008.05.006.

[149] K. Barczak, T. Pustelny, Z. Zycki, and T. Blazejczyk, “Optical fibre magnetic field sensors for monitoring of the state of work of electric motors,” *Acta Phys. Pol. A*, vol. 116, no. 3, pp. 250–253, 2009, doi: 10.12693/APhysPolA.116.250.

[150] J. I. Melecio, A. Mohammed, and S. Djurovic, “Characterisation of FBG based Magnetic Field Sensor Response Sensitivity to Excitation Orientation for Rotating Electric Machine Applications,” *2019 8th Mediterr. Conf. Embed. Comput. MECO 2019 - Proc.*, no. June, pp. 10–14, 2019, doi: 10.1109/MECO.2019.8760181.

[151] J. B. Rosolem, C. Floridia, and J. P. M. Sanz, “Field and laboratory demonstration of a fiber-optic/RF partial discharges monitoring system for hydrogenerators applications,” *IEEE Trans. Energy Convers.*, vol. 25, no. 3, pp. 884–890, 2010, doi: 10.1109/TEC.2010.2044507.

[152] Y. Wang, X. Li, Y. Gao, H. Zhang, D. Wang, and B. Jin, “Partial discharge ultrasound detection using the Sagnac interferometer system,” *Sens. Switz.*, vol. 18, no. 5, pp. 1–18, 2018, doi: 10.3390/s18051425.

[153] K. M. Sousa, U. J. Dreyer, C. Martelli, and J. C. Cardozo Da Silva, “Dynamic Eccentricity Induced in Induction Motor Detected by Optical Fiber Bragg Grating Strain Sensors,” *IEEE Sens. J.*, vol. 16, no. 12, pp. 4786–4792, 2016, doi: 10.1109/JSEN.2016.2554885.

[154] A. Mohammed, J. I. Melecio, and S. Durovic, “Electrical Machine Permanent Magnets Health Monitoring and Diagnosis Using an Air-Gap Magnetic Sensor,” *IEEE Sens. J.*, vol. 20, no. 10, pp. 5251–5259, 2020, doi: 10.1109/JSEN.2020.2969362.

[155] I. García, J. Zubia, G. Durana, G. Aldabaldetreku, M. A. Illarramendi, and J. Villatoro, “Optical fiber sensors for aircraft structural health monitoring,” *Sens. Switz.*, vol. 15, no. 7, pp. 15494–15519, 2015, doi: 10.3390/s150715494.

[156] T. J. Barnish, M. R. Muller, and D. J. Kasten, “MOTOR MAINTENANCE: A SURVEY OF TECHNIQUES AND RESULTS,” 1997, pp. 287–297.

[157] IEEE Industry Applications Society, “IEEE Standard 841,” 2009.

[158] A. Leal-Junior, A. Frizera, C. Díaz, C. Marques, M. Ribeiro, and M. J. Pontes, “Material features based compensation technique for the temperature effects in a polymer diaphragm-based FBG pressure sensor,” *Opt. Express*, vol. 26, no. 16, p. 20590, 2018, doi: 10.1364/oe.26.020590.

[159] A. Mohammed and S. Djurović, “Feasibility study of embedded FBG thermal sensing use for monitoring electrical fault-induced thermal excitation in random wound coils,” *J. Eng.*, vol. 2019, no. 17, pp. 4147–4151, 2019, doi: 10.1049/joe.2018.8108.

[160] D. Hu, Z. Wang, Q. Yuan, T. Xie, and D. Jia, “Synchronous interrogation of multiple FBG sensors using multi-wavelength parallel swept light source,” in *Advanced Sensor Systems and Applications VIII*, Oct. 2018, p. 44. doi: 10.1117/12.2327121.

[161] “Machine learning methods for wind turbine condition monitoring: A review”, doi: 10.1016/j.renene.2018.10.047.

[162] S. B. Lee *et al.*, “Condition Monitoring of Industrial Electric Machines: State of the Art and Future Challenges,” *IEEE Ind. Electron. Mag.*, vol. 14, no. 4, pp. 158–167, 2020, doi: 10.1109/MIE.2020.3016138.

[163] S. Schwendemann, Z. Amjad, and A. Sikora, “A survey of machine-learning techniques for condition monitoring and predictive maintenance of bearings in grinding machines,” *Comput. Ind.*, vol. 125, p. 103380, Feb. 2021, doi: 10.1016/j.compind.2020.103380.

[164] S. Lu, H. Chai, A. Sahoo, and B. T. Phung, “Condition Monitoring Based on Partial Discharge Diagnostics Using Machine Learning Methods: A Comprehensive State-of-the-Art Review,” *IEEE Trans. Dielectr. Electr. Insul.*, vol. 27, no. 6, pp. 1861–1888, Dec. 2020, doi: 10.1109/TDEI.2020.009070.

[165] "IEEE Standard Test Procedure for Thermal Evaluation of Systems of Insulating Materials for Random-Wound AC Electric Machinery," *IEEE Std 117-2015 Revis. IEEE Std 117-1974*, pp. 1–34, 2016, doi: 10.1109/IEEESTD.2016.7466454.

[166] International Electrotechnical Commission, "IEC 60034-1:2017 Rotating electrical machines - Part 1: Rating and performance," IEC. [Online]. Available: https://webstore.iec.ch/publication/28145

[167] T. Electronics, "High Power Resistors-Type SQ series," 2018.

[168] Arcadia optronix.Inc, "A novel FBG demodulation module based on semiconductor tunable laser," CN 205156936 U, 2016

[169] Arcopt.Inc, "FBG Interrogator Datasheet," 2019.

[170] Y. Lei, B. Yang, X. Jiang, F. Jia, N. Li, and A. K. Nandi, "Applications of machine learning to machine fault diagnosis: A review and roadmap," *Mech. Syst. Signal Process.*, vol. 138, p. 106587, 2020, doi: 10.1016/j.ymssp.2019.106587.

[171] R. Liao, H. Zheng, S. Grzybowski, and L. Yang, "Particle swarm optimization-least squares support vector regression based forecasting model on dissolved gases in oil-filled power transformers," *Electr. Power Syst. Res.*, vol. 81, no. 12, pp. 2074–2080, 2011, doi: 10.1016/j.epsr.2011.07.020.

[172] V. Vapnik, S. E. Golowich, and A. Smola, "Support vector method for function approximation, regression estimation, and signal processing," *Adv. Neural Inf. Process. Syst.*, pp. 281–287, 1997.

[173] "scikit-learn: machine learning in Python — scikit-learn 1.0.2 documentation." https://scikit-learn.org/stable/index.html (accessed May 05, 2022).

[174] P. Daogang, C. Yuewei, and Q. Yuliang, "Transformer winding temperature soft measurement model based on particle swarm optimization-support vector regression," *Trans. China Electrotech. Soc.*, vol. 33, no. 8, pp. 1742–1749, 2018.

[175] W. Chen, X. Su, X. Chen, Q. Zhou, and H. Xiao, "Combination of support vector regression with particle swarm optimization for hot-spot temperature prediction of oil-immersed power transformer," *Przeglad Elektrotechniczny*, vol. 88, no. 8, pp. 172–176, 2012.

[176] V. N. Vapnik, *The Nature of Statistical Learning Theory*. Springer New York, 2000. doi: 10.1007/978-1-4757-3264-1.

[177] M. Galea, C. Gerada, T. Raminosoa, and P. Wheeler, "A thermal improvement technique for the phase windings of electrical machines," *IEEE Trans. Ind. Appl.*, vol. 48, no. 1, pp. 79–87, 2011.

[178] N. Simpson, R. Wrobel, and P. H. Mellor, “Estimation of Equivalent Thermal Parameters of Impregnated Electrical Windings,” *IEEE Trans. Ind. Appl.*, vol. 49, no. 6, pp. 2505–2515, Nov. 2013, doi: 10.1109/TIA.2013.2263271.

[179] A. E. Fitzgerald, C. Kingsley, and S. D. Umans, *Electric machinery*, 6th ed. Boston, Mass: McGraw-Hill, 2003.

[180] D. C. Liu and J. Nocedal, “On the limited memory BFGS method for large scale optimization,” *Math. Program.*, vol. 45, no. 1, pp. 503–528, Aug. 1989, doi: 10.1007/BF01589116.

[181] L. Bottou, “Stochastic Gradient Descent Tricks,” in *Neural Networks: Tricks of the Trade: Second Edition*, G. Montavon, G. B. Orr, and K.-R. Müller, Eds. Berlin, Heidelberg: Springer, 2012, pp. 421–436. doi: 10.1007/978-3-642-35289-8_25.

[182] D. P. Kingma and J. Ba, “Adam: A Method for Stochastic Optimization,” *ArXiv14126980 Cs*, Jan. 2017, Accessed: May 12, 2022. [Online]. Available: http://arxiv.org/abs/1412.6980

[183] P. Bühlmann, “Bagging, Boosting and Ensemble Methods,” in *Handbook of Computational Statistics: Concepts and Methods*, J. E. Gentle, W. K. Härdle, and Y. Mori, Eds. Berlin, Heidelberg: Springer, 2012, pp. 985–1022. doi: 10.1007/978-3-642-21551-3_33.

[184] R. J. Lewis and P. D, “An Introduction to Classification and Regression Tree (CART) Analysis," presented at Annual Meeting of the Society for Academic Emergency Medicine,” in *Annual Meeting of the Society of Academic Emergency Medicine in*, 2000.

[185] B. K. Nagaraja Rao, “The Role of Artificial Intelligence (AI) in Condition Monitoring and Diagnostic Engineering Management (COMADEM): A Literature Survey,” *Am. J. Artif. Intell.*, vol. 5, no. 1, p. 17, 2021, doi: 10.11648/j.ajai.20210501.12.

[186] M. Cerliani, “tsmoothie.” May 01, 2022. Accessed: May 05, 2022. [Online]. Available: https://github.com/cerlymarco/tsmoothie

[187] V. Sai Vineeth, H. Kusetogullari, and A. Boone, “Forecasting Sales of Truck Components: A Machine Learning Approach,” in *2020 IEEE 10th International Conference on Intelligent Systems (IS)*, 2020, pp. 510–516. doi: 10.1109/IS48319.2020.9200128.

[188] R. Nicolas, “The different driving cycles,” *Car Engineer*, Jan. 05, 2013. https://www.car-engineer.com/the-different-driving-cycles/ (accessed May 05, 2022).

[189] M. Mieloszyk and W. Ostachowicz, “An application of Structural Health Monitoring system based on FBG sensors to offshore wind turbine support structure model,” *Mar. Struct.*, vol. 51, pp. 65–86, Jan. 2017, doi: 10.1016/j.marstruc.2016.10.006.

[190] M. Benbouzid, T. Berghout, N. Sarma, S. Djurović, Y. Wu, and X. Ma, “Intelligent Condition Monitoring of Wind Power Systems: State of the Art Review,” *Energies*, vol. 14, no. 18, p. 5967, Sep. 2021, doi: 10.3390/en14185967.

Appendix

1. Matlab code for FBG sensor demodulation

```
% This program can achieve real-time control & interaction with the Keysight optic
insertion loss engine.

EngineMgr=actxserver('AgServerIL.EngineMgr'); % Connect to Engine Manager
EngineIDs=EngineMgr.EngineIDs; % List all Engines currently running
Engine=EngineMgr.OpenEngine(EngineIDs(1)); % Always connect to first engine
Engine.StartMeasurement; % Start measurement
 % Wait for measurement to be finished
 while Engine.Busy; pause(1);
 end
MeasurementResult = Engine.MeasurementResult; % Get result object
MeasurementResult.Write('c:\test.omr');  % Save as OMR file

% Data invoke from Keysight insertion loss engine to Matlab
 Graph = MeasurementResult.Graph('RXTXAvgIL');
 noChannels      = Graph.noChannels;
 dataPerCurve    = Graph.dataPerCurve;
 YData = reshape(Graph.YData,dataPerCurve,noChannels);
 xStart = Graph.xStart * 1000000000;
 xStep = Graph.xStep* 1000000000;
 xStop = Graph.xStop* 1000000000;
 XData =  xStart: xStep: xStop;
 plot(XData, YData);
hold on
% Peak tracking function
 [pks,locs] = findpeaks(YData,'minpeakheight',21);% 21 is the value of peak
                  judging threshold in this application. It is scenario-dependent.
 lambda_p = xStart + locs*xStep;
 temp_room = 22.33; % room temp in Celsius degree
 lambda_ref =[1529.84978,1532.929,1536.012,1538.82939];% set 4 ref central
wavelengths at room temp in nm, these values are scenario-dependent.
A = reshape(lambda_ref,4,1);% flip the ref wavelength data to matched matrix scale
B = lambda_p-A; % calculate the wavelength shift
temp_coe = 0.012; % FBG temperature coefficient for 12 pm/C = 0.012 nm/C
temp = temp_room + (B)/temp_coe;% current temp calculation

% Plot the figure for temperatures and FBG central wavelengths display
plot (lambda_p,temp,'o');
title('Temp reading & spectral of FBGs');
ylabel('TEMP/(?) & loss spectrum/(dB)') ;xlabel('wavelength/(nm)') ;
text (lambda_p,temp,num2str(temp));
hold on
```

2. Scikit-learn code for multi-position inner winding temperature prediction

```
### This program can be used to construct three types of ML models for inner
winding temperature prediction

# Related library import
import numpy as np
import matplotlib as mpl
import matplotlib.pyplot as plt
import pandas as pd
import sklearn
import sklearn.ensemble
import sklearn.preprocessing
import sklearn.metrics
import ast

from sklearn.metrics import mean_absolute_error
from sklearn.metrics import mean_squared_error
from sklearn.metrics import explained_variance_score
from sklearn.metrics import r2_score
from sklearn.svm import SVR
from sklearn.model_selection import train_test_split
from sklearn.model_selection import GridSearchCV
from sklearn.datasets import make_regression
from sklearn.model_selection import cross_val_score
from sklearn.model_selection import RepeatedKFold
from sklearn.multioutput import MultiOutputRegressor
from sklearn.ensemble import RandomForestRegressor
from sklearn.neural_network import MLPRegressor
from sklearn.preprocessing import StandardScaler
from sklearn.pipeline import make_pipeline
from sklearn.model_selection import learning_curve
from sklearn.model_selection import TimeSeriesSplit
from tsmoothie.utils_func import sim_randomwalk
from tsmoothie.smoother import LowessSmoother
from tsmoothie.smoother import ExponentialSmoother
from tsmoothie.smoother import *

# Prevent garbled code
mpl.rcParams['font.sans-serif']=[u'simHei']
mpl.rcParams['axes.unicode_minus']=False
def notEmpty(s):
    return s != ''

# Data preprocessing

# Raw data loading
fd = pd.read_csv("rawdata.csv", header = None, skiprows=[0,1])# load the raw
dataset recorded by our multi-sensor test-rig, skip row 0 which generally are
variable names.
```

```
features_raw = fd.get([ ])  # insert the column number of required input features,
including FBG wavelengths, electrical and mechanical variables
data = np.array(features_raw)

# Exponential smoothing function
smoother = ExponentialSmoother(window_len=1,alpha=0.3)
smoother.smooth(data)

# Export data after smoothing
if_s = smoother.smooth_data
np.savetxt("smoothdata.csv", if_s, delimiter=',')

# loading the previous recorded datasets
fd = pd.read_csv("smoothdata.csv", header = None, skiprows=[0,1])#  skip row 0
which generally are variable names
# Selection of input features & target outputs
outputs=fd.get([]) # column number of target inner winding temperatures
features = fd.get([# column number of mechanical features
                   # column number of FBG central wavelengths
                   # column number of electrical features
                   # column number of thermocouples measured temperatures
                   ])

#Time-series data split function
features = np.array(features)
outputs = np.array(outputs)
tscv = TimeSeriesSplit(gap=2, max_train_size=None, n_splits=5, test_size=None)
for train_index, test_index in tscv.split(features):

    x_train, x_test = features[train_index], features[test_index]
    y_train, y_test = outputs[train_index], outputs[test_index]
```

ML models training and optimization process

```
 #1.SVR modeL training and optimization
parameters = {
    'kernel': ['rbf','poly','sigmoid'...],
    'C': [],
    'gamma': [],
    'epsilon': []
    'd': []
    'b_0':[]}# SVR hyperparameters range setting for model optimization
model = GridSearchCV(SVR(), param_grid=parameters,
                     #verbose=3,
                     cv=5,
                     n_jobs=-1) # GridSearch hyperparameter optimization function,
svr_outs_mor = make_pipeline(StandardScaler(), # z-score Data standardization
function
                             MultiOutputRegressor(model))
svr_outs_mor.fit(x_train, y_train)
```

```
# 2.MLPR modeL training and optimization
param_list = {
    'hidden_layer_sizes': [ ],
    'activation': ["identity", "logistic", "tanh", "relu"],
    'solver': ["lbfgs", "sgd", "adam"],
    'alpha':[ ]
            }  # MLPR hyperparameters range setting for model optimization
model = GridSearchCV(MLPRegressor(), param_grid=param_list,
                     #verbose=3,
                     cv=5,
                     n_jobs=-1)
mlp = make_pipeline(StandardScaler(),
                                MultiOutputRegressor(model))
mlp.fit(x_train, y_train)

# 3.RFR modeL training and optimization
param_list = { 'n_estimators':[],
        'max_depth':[],
        'rfr__min_samples_leaf':[],
        'rfr__min_samples_split':[],
              } # RFR hyperparameters range setting for model optimization
model = GridSearchCV(RandomForestRegressor(), param_grid=param_list,
                     #verbose=3,
                     #oob_score=True,
                     cv=5,
                     n_jobs=-1)
rfr = make_pipeline(StandardScaler(),
                                MultiOutputRegressor(model))
rfr.fit(x_train, y_train)

# To be noticed, the above three types of ML algorithms (SVR, MLPR, RFR) cannot be
trained simultaneously. We listed them together to present the source code
efficiently.

# Validation data plot
ln_features = range(len(features))
y_predict_all = svr_outs_mor.predict(features)
ln_x_test = range(len(x_test))
plt.figure(figsize=(16,8), facecolor='w')
plt.plot(ln_features, outputs, 'r-', lw=2, label=u'T_exp', linestyle='-')
plt.plot(ln_features, y_predict_all, 'g-', lw =2, label=u'T_predict VS T_exp by
SVR/MLPR/RFR: Validation', linestyle='-.')

# Plot figure display for quick check
plt.legend(loc = 'upper left')
plt.grid(True)
plt.title(u" ")
plt.xlim(0, 3000)
plt.show()

# Regression performance evaluation indices for validation data
```

```
print("MAE is:", sklearn.metrics.mean_absolute_error(y_test, y_predict))
print("EVS is:", sklearn.metrics.explained_variance_score(y_test, y_predict))
print("MSE is:", sklearn.metrics.mean_squared_error(y_test, y_predict))
print("R-squared is:", sklearn.metrics.r2_score(y_test, y_predict))
print ("Training set accuracy:%.2f%%" % (svr_outs_mor.score(x_train, y_train) *
100))
print ("Validation set accuracy:%.2f%%" % (svr_outs_mor.score(x_test, y_test) *
100))

#Export predicted validation data
outputpath='c:ypred_valid.csv'
y_predict_valid= pd.DataFrame(y_predict_all)
y_predict_valid.to_csv(outputpath,sep=',',index=False, header=True)

# Trained ML models testing

# Loading the data from testing datasets
fd = pd.read_csv("newdataset.csv", header = None, skiprows=[0,1])#  skip row 0
variable names

outputs_2=fd.get([]) # column number of target inner winding temperatures
features_2 = fd.get([# column number of mechanical features
                     # column number of FBG central wavelengths
                     # column number of electrical features
                     # column number of thermocouples measured temperatures
                     ])
# Testing data plot
colors = ['g-', 'b-']
ln_features_2 = range(len(features_2))
y_predict_2 = svr_outs_mor.predict(features_2)
# The y_predict_2 here is the testing results of the trained SVR model. It can be
altered depending on the core ML algorithms, i.e. SVR, MLPR or RFR. Check the name
of other models above.

plt.figure(figsize=(20,10), facecolor='w')
plt.plot(ln_features_2, outputs_2, 'r-', lw=2, label=u'T_exp', linestyle='-')
plt.plot(ln_features_2, y_predict_2, 'g-', lw = 2, label=u'T_predict VS T_exp by
SVR/MLPR/RFR: Testing' , linestyle='-.')

# Plot figure display for quick check
plt.legend(loc = 'upper left')
plt.grid(True)
plt.title(u"")
plt.xlim(0, 3000)
plt.show()

# Regression performance analysis indices for testing data
print("MAE is:", sklearn.metrics.mean_absolute_error(outputs_2, y_predict_2))
print("EVS is:", sklearn.metrics.explained_variance_score(outputs_2, y_predict_2))
print("MSE is:", sklearn.metrics.mean_squared_error(outputs_2, y_predict_2))
print("R-squared is:", sklearn.metrics.r2_score(outputs_2, y_predict_2))
```

```
#Export predicted testing data
outputpath='c:ypred_testing.csv'
y_predict_test= pd.DataFrame(y_predict_2)
y_predict_test.to_csv(outputpath,sep=',',index=False, header=True)
```